Università degli Studi di Padova
Scuola di Dottorato di Ricerca in Fisica - XXV Ciclo
Dipartimento di Fisica ed Astronomia "Galileo Galilei"

Innovative techniques for Non Destructive Analysis

Direttore della Scuola: Ch.mo Prof. Andrea Vitturi
Supervisore: Ch.mo Prof. Giuseppe Viesti

Dottorando: Luca Stevanato

Contents

Executive Summary

English

This work describes the development of a radiometric mobile inspection system called SMANDRA (the Italian acronym stands for Sistema Mobile per Analisi Non Distruttive e RAdiometriche). SMANDRA is part of a large project called SLIMPORT, financed by the Italian Ministry for the Economic Development (MISE), dedicated to the development of an integrated toolbox forming a complete security system to monitor the flow of persons and merchandise in harbors. The system has been conceived as a flexible and transportable tool, to be used in conjunction with fixed installation such as radiation portal monitors, x-ray scanners and large detector arrays. In particular, the aims of SMANDRA are to detect and identify sources of ionizing radiation or identify dangerous and/or illegal materials inside volumes previously tagged as "suspect" by conventional X-ray scanners. The whole detector apparatus was designed minimizing volume and weight to be easily movable, mounted over forklifts or other light vehicles for inspections. In addition, it is possible to operate the entire system with batteries, making it completely independent from external power facilities. The system is made of two pieces having a volume less than 0.1 m^3 as follows:

- A passive unit including two gamma-ray detectors (5"x5" NaI(Tl) and 2"x2" $LaBr_3$(Ce)) and two neutron counters (5"x2" liquid scintillator NE-213 and ^{3}He proportional counter for fast and slow neutrons). The unit hosts batteries, power supplies, front-end electronics and CPU.

- An active unit including a portable sealed neutron generator based on the Tagged Neutron Inspection System (TNIS) technique.

The first unit can be used in standalone mode as a high efficiency spectroscopic radiometer for the detection of ionizing radiation such as gamma-rays, fast and thermal neutrons to search and identify radioactive material as well as Special Nuclear Material (SNM). It can also be used as detector package connected to the second unit for active interrogation of voxels inside a load by tagged neutron inelastic scattering imaging. All detector used in the SMANDRA system have been fully characterized. Initial tests were done with traditional analog NIM electronics followed by the new digital electronics based on fast digitizers. The detection and identification of standard radioactive sources (gamma ray and neutrons) has been tested successfully showing detection probability in order or even better with the requirements of this type of instrumentation. The detection of special nuclear material has been tested using SMANDRA as a high sensitivity passive spectroscopic system or as a complete active inspection system using tagged neutrons. The detection of plutonium samples seems to be possible with passive interrogation even in case of small samples (few

grams) due to the yield of gamma ray and neutrons. As it is well known, detection of uranium samples poses more problems because of the low neutron yield that characterizes this material. The gamma ray yield of highly enriched U samples could be easily shielded. In this case active interrogation is needed. Results show that it is possible to provide signature for the discrimination of uranium against heavy metals (as lead) by looking to the absolute gamma and neutron yield in coincidence with tagged neutrons or to correlations between detectors. It is worth mentioning that the SMANDRA system is a mobile multi-purpose spectrometric system not specifically designed to detect SNM. However the results reported might be implemented in future portable systems specifically designed to detect SNM in active mode.

Italiano

Questo lavoro descrive lo sviluppo di un sistema mobile per ispezioni radiometriche, chiamato SMANDRA (Sistema Mobile per Analisi Non Distruttive e Radiometriche). SMANDRA fa parte di un grande progetto chiamato SLIMPORT, finanziato dal Ministero Italiano dello sviluppo Economico (MISE), rivolto allo sviluppo di un sistema di sicurezza integrato per il monitoraggio del flusso di persone e merci nei porti. Il sistema è stato progettato come uno strumento mobile e flessibile, da usare in combinazione con postazioni fisse come portali, scanners x-ray e grandi array di rivelatori. Più in particolare, lo scopo di SMANDRA è quello di identificare sorgenti radioattive e materiali illegali e/o pericolosi nascosti dentro container e bagagli segnalati come "sospetti" dai sistemi di sicurezza tradizionali. L'intero apparato è stato disegnato per minimizzare il volume ed il peso in modo da essere facilmente trasportabile su un muletto o su altri veicoli leggeri per ispezioni mirate. In aggiunta il sistema può essere alimentato a batterie, rendendolo completamente indipendente dall'allacciamento elettrico. Il sistema è composto di due unità che hanno un volume totale minore di 0.1 m^3:

- Un'unità passiva composta da due rivelatori di raggi gamma (5"x5" NaI(Tl) e 2"x2" $LaBr_3$(Ce)) e due rivelatori di neutroni (scintillatore liquido NE-213 da 5"x2" e un contatore proporzionale ad ^{3}He). L'unità contiene le batterie, l'alimentazione, l'elettronica digitale e la CPU per l'acquisizione ed analisi dati.

- Un'unità passiva che include un generatore portatile di neutroni per l'identificazione dei materiali illeciti e/o pericolosi tramite la tecnica TNIS (Tagged Neutron Inspection System).

La prima unità può essere usata da sola come un radiometro spettroscopico ad alta efficienza per la rivelazione di radiazioni ionizzanti come raggi-gamma, neutroni veloci e neutroni termici e per identificare materiale radioattivo come ad esempio il Materiale Speciale Nucleare (SNM). Questa unità è poi usata insieme al generatore di neutroni per interrogazioni attive di specifiche porzioni di volume all'interno di container, grazie alla tecnica TNIS. Tutti i rivelatori di SMANDRA sono stati totalmente caratterizzati: i test iniziali sono stati fatti con elettronica analogica NIM seguiti da quelli effettuati con la nuova elettronica digitale basata su digitizer veloci. È stata dimostrata la possibilità di rivelare e identificare le sorgenti radioattive standard (raggi-gamma e neutroni) con un livello di confidenza migliore di quello richiesta dallo standard per questo tipo di strumentazione. La rivelazione di materiale speciale nucleare è stata testata sia in modalità passiva con la prima unità

sia in modalità attiva usando il generatore di neutroni. Il riconoscimento di un campione di plutonio è possibile con la sola interrogazione passiva anche in caso di campioni molto piccoli (qualche grammo) grazie all'alta emissione di raggi-gamma e neutroni. Come è noto, invece, la rivelazione di campioni di Uranio è più difficoltosa vista la bassa emissione di neutroni e la possibilità di schermare facilmente i pochi raggi-gamma; in questo caso è necessario intervenire con un'interrogazione attiva. I risultati dimostrano la possibilità di discriminare fra campioni di Uranio rispetto a metalli pesanti (come il piombo) guardando i conteggi assoluti di raggi-gamma e neutroni in coincidenza con l'emissione di un neutrone da parte del generatore o, in alternativa, guardando alla correlazione degli eventi fra due rivelatori (NaI(Tl) e NE-213). È importante sottolineare che SMANDRA è un sistema spettrometrico mobile multi-funzione, non disegnato specificamente per la rivelazione di materiale speciale nucleare. Tuttavia i risultati mostrano la possibilità in futuro di poter implementare sistemi portatili disegnati specificatamente per l'identificazione di Materiale Speciale Nucleare con l'ausilio di un generatore di neutroni.

Chapter 1

Introduction

Nowadays, the construction of a nuclear weapon does not pose strong technical problem, since the baisc know-how has been in the public domain for several decades [1]. The only barrier preventing a terrorist group from performing a nuclear attack is the difficulty to access to a sufficient amount of special nuclear material (SNM) as highly enriched weapon-graded uranium (WGU) or weapon-graded plutonium (WGP), as defined in the next section.

Stockpiles of SNM should be stored in high-security facilities, but the "nuclear club" of nations who possess nuclear technologies and materials has widened compared to Cold War years, and a black market of procurement networks is being formed [2]. In such situation, the second line of defense will be the ability to detect special nuclear material (SMN) while in transit through the civilian transportation infrastructure.

U.S. homeland security experts say that terrorist threats are most likely to enter our nation by way of the sea, in one of the nearly seven million cargo containers offloaded at U.S. ports every year. These tractor-trailer-sized, steel-walled boxes are typically sealed in foreign ports and not opened until delivered by trucks to points all across the country. Despite heightened security concerns following the September 11 terrorist attacks, less than two percent of these containers have been in past years inspected at U.S. seaports, according to the U.S. Customs and Border Protection agency.

Today's approach to nuclear detection relies primarily on fixed inspection portals placed at the national borders (the so-called port-of-entry) or in other transportation nodes; while their presence still represents an advancement in security procedures, doubts have been rised about the possibility that highly shielded or masked SNM might not be detected by those portals. A real improvement would be reaching the capability to detect nuclear materials with improved detection systems anywhere within the transportation infrastructure; that would deter nuclear terrorist attempting to pursue construction and deployment of a nuclear weapon. Hence, last years

have seen a large extension of research projects in the field of mobile instruments, to which this work belongs.

1.1 Definition of the problem

The following items are considered to be radiological/nuclear[1] threats:

1. operative nuclear weapons;
2. improvised Nuclear Devices (IND);
3. special Nuclear Material (SNM) that might be used to realize an IND;
4. radioactive material to be used inside Radiological Dispersal Devices (RDD).

Radioactive isotopes in each of the four classes emit gamma radiation. Neutron radiation may be emitted too, but not necessarily in substantial quantities. An RDD may contain radiological material emitting no neutron radiation at all, some uranium isotopes emit negligible amounts of neutron radiation. On the contrary most plutonium isotopes are known to be strong neutron sources.

Detectable signatures of RDD components

Generally speaking, RDD components (item 4 above) present no detection problems, even if shielded. Indeed, in order to have a significant contamination potential, the activity of a Radiological Dispersive Device is expected to be at the 1 MBq level.

Detectable signatures of SNM

SNM (items 1-3 above) may present non trivial detection problems. The most known Special Nuclear Material are the following:

- Weapons Grade Uranium (WGU), typically having a composition similar to the following:

  $$^{234}\text{U } 1\%,\ ^{235}\text{U } 93\%,\ ^{238}\text{U } 6\%$$

  The IAEA defines 25 kg of WGU as a "significant quantity"

- Weapons Grade Plutonium (WGPu), typically having a composition similar to the following:

  $$^{239}\text{Pu } 93\%,\ ^{240}\text{Pu } 6\%.$$

[1]The nomenclature "radiological" refers to any radioactive material usable for radiological terrorism including RDDs ("dirty bombs"). "Nuclear" refers specifically to neutron emitting materials, i.e. transuranic actinides such as uranium and plutonium isotopes.

The IAEA defines 8 kg of WGPu as a “significant quantity”.

Besides depending on the SNM composition and quantity, a nuclear device’s radiation emission also depends on further factors such as geometry and tamper material.

A schematic diagram of an implosion bomb is illustrated in Fig. 1.1, where the radioactive core is surrounded by a first shell of 2 cm Beryllium acting as reflector and a second shell of 3 cm Tungsten or depleted Uranium acting as tamper material. The tamper material has an influence on the emitted radiation rate, as can be seen in Table 1.1.

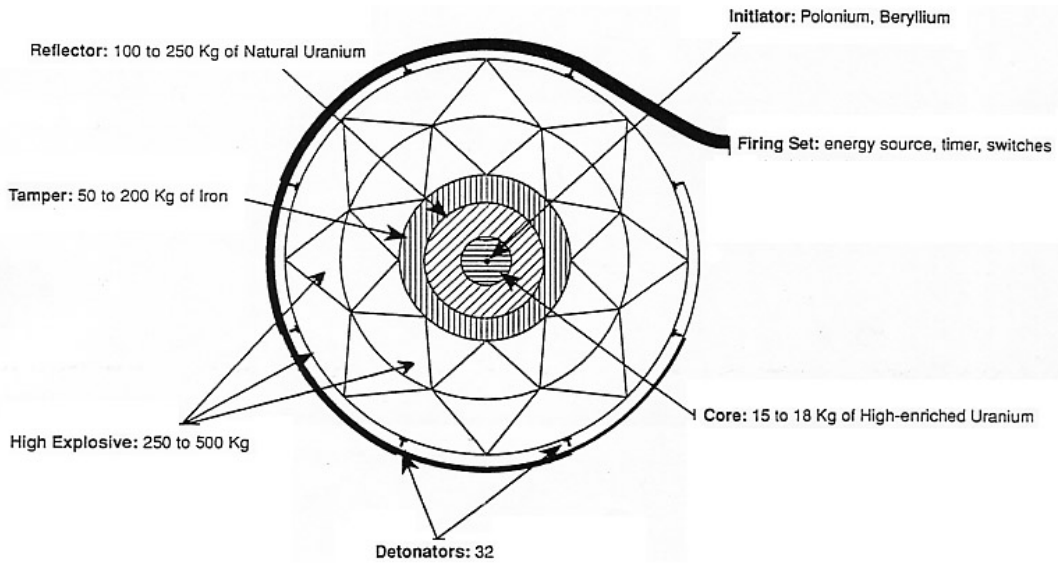

Figure 1.1: Weapon model used for signature estimation

	WGU		WGPu	
Tamper mat.	n rate (n/s)	γ rate (γ/s)	n rate (n/s)	γ rate (γ/s)
Tungsten	∼30	∼30	$\sim 4 \cdot 10^5$	$\sim 10^3$
Depleted U	∼1400	$\sim 10^5$	$\sim 4 \cdot 10^5$	$\sim 10^5$

Table 1.1: Tamper material influence on the emitted radiation rate

Unless a genuine spectrometric capability is implemented, the gamma ray spectrum from WGU and WGPu can easily be masked by radioactive substances of common use in industry and by Natural Occurring Radioactive Material (NORM).

Irrespective of the high gamma ray flux, the detection of WGU and WGPu is often driven by neutron detection, essentially because natural neutron backgrounds are typically 3 orders of magnitude lower than natural gamma background. Moreover,

the majority (>95%) of all neutrons emitted by SNM are so-called fast neutrons, with energies above the keV region. The possibility to distinguish fast from thermal neutrons offers the possibility to enhance the discrimination against natural background sources: this issue will be exploited in this work.

Neutron radiation signature

Neutron emission from the core material, including spontaneous fission and alpha particle induced neutron emission, is about 20 and $2 \cdot 10^5$ neutrons/second for the 12 kg and 4 kg of WGU and WGPu respectively. This is the characteristic neutron emission from bulk SNM. In case of an IND (see Fig. 1.1), the neutron yield also depends on the type of tamper material. If the device uses 12 kg of WGU and tungsten then the total emission at surface is about 30 neutrons/second. If the device uses Depleted Uranium then the emission is about 1400 neutron/second, due to neutron multiplication in these materials. Neutron emission remains very high in the case of WGPu devices for both tamper materials (about $4 \cdot 10^5$ neutron/second). Natural neutron backgrounds are typically three orders of magnitude lower than natural gamma backgrounds.

The majority (>95%) of all neutrons emitted by SNM are fast neutrons. Shielding generally has a thickness-dependent effect on the fast neutron component. Fig. 1.2 shows the shielding dependence of the fast neutron fraction within the total neutron signature.

Gamma radiation signature

Neutron emission is accompanied by an important yield of gamma rays. As shown in [3], most of the isotopes of interest emit on average 6.5 gamma rays of 1 MeV energy (per fission). The use of DU tamper entails an emission of 10^5 gamma/second for both WG material. This value decreases with tungsten tampers that act as a gamma-ray shield. In this case the emission reaches 30 gamma/second for WGU and 100 gamma/second for WGPu

Some characteristic gamma-rays are often used to identify relevant isotope. For example, ^{235}U is normally identified by looking at the 186 keV transition. However, it has been reported that such low-energy lines are easily shielded or even masked by other radioactive substances of common use in industry (such as ^{137}Cs), thus making the identification of ^{235}U by only its gamma-ray signature difficult.

Signature strengths relative to background

The detection of WGPu is generally based on neutron emission. More difficult is the detection of WGU, especially when tungsten rather than DU tampers are utilized.

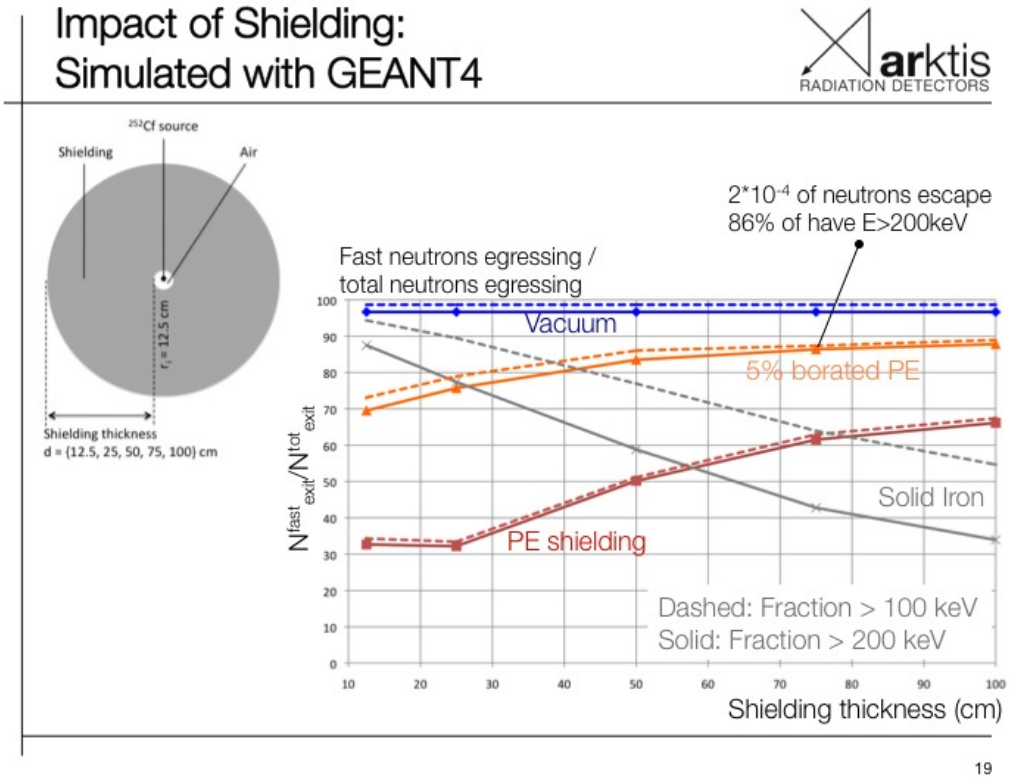

Figure 1.2: Plot showing the effect of shielding on the fraction of fast neutrons escaping an IND device described above based on simulations using GEANT4 [**?**]

When searching for neutrons as the signature of SNM, the background due to neutrons produced in the interaction of cosmic rays at sea level is about 10^{-2} neutrons/second/cm^2, increasing significantly with altitude. It is worth noting that natural background is four times lower than that induced by the test ^{252}Cf source in the IEC 62244 standard. Moreover, the neutron background seen by a fast neutron detector is two orders of magnitude higher than that seen by a thermal neutron detector.

In such background conditions and with a hypothetical neutron detector with 25% efficiency and 10 cm diameter, it is quite easy to detect the strong neutron yield from WGPu even at large stand-off distances (several meters), whereas the detection of WGU is more difficult, especially when the tungsten tamper is used. In the later case it is only possible do detect the neutron yield at very close distance (at contact).

1.2 International standards

IEC (International Electrotecnical Commission) defined a set of standard for detection systems dedicated to the monitor of ionizing radiations in various scenery. Two of them are of particular interest to this project:

a) IEC62244, Radiation protection instrumentation - Installed radiation monitors for the detectio nof radioactive and special nuclear materials at national borders

b) IEC 62327, Hand-held instruments for the detection and identification of radionuclides and additionally for the indication of ambient dose equivalent rate from photon radiation

The main difference between the two standards is that hand-held devices are required to detect not only the presence of a radiation source, but also to be able to identify it. Briefly, IEC IEC62327 rules require:

- in case of gamma rays, to launch an alarm within 3 seconds if radiation levels exceed threshold, and to identify the source in 1-2 minutes for a dose rate of 500 nSv/h on the detector
- as of the neutrons, to get an alarm in 10 seconds in presence of a ^{252}Cf source producing a neutronic dose of 3 microSv/h on the detector (corresponding to a source emitting $2 \cdot 10^4$ neutrons/s placed at a distance of 25 cm)

Another technical guidance is prepared by IAEA. The document is addressed to all instruments used by FLOs (Front Line Officers) and experts. We are interested in particular to RIDs (Radionuclide Identification devices), NSDs (neutron search devices) hand-held systems and Portable radiation scanners (PRSs). The common requirements for these systems are:

- False Alarm Rate (FAR) for either gamma rays or neutrons during operation shall not be more than one per hour.
- Probability of detection of 90% with a condifence level of 95%
- Detection of radioactive material that produces a dose rate of 0.05μSv/h in the point of closest approach to the instrument and moves with a speed of 0.5 m/s.
- Detection of γ-ray in the energy range from 50 keV to 1.33 MeV.

SMANDRA meets or overcomes all of these requirements; details on the tests are presented in Sec. 5.

1.3 SMANDRA - General description

The SLIMPORT project [4], financed by the Italian Ministry for the Economic Development (MISE), has been dedicated to the development of an integrated toolbox forming a complete security system to monitor the flow of persons and merchandise

in harbors. In this framework, a mobile inspection station (called SMANDRA, the Italian acronym stands for Sistema Mobile per Analisi Non Distruttive e RAdiometriche) has been developed. The system has been conceived as a flexible and transportable tool, usable in conjunction with fixed installation such as radiation portal monitors, x-ray scanners and large detector arrays. In particular, the aims of SMANDRA are to detect and identify sources of ionizing radiation or identify dangerous and/or illegal materials inside volumes previously tagged as suspect by conventional X-ray scanners. The whole detector apparatus was designed minimizing volume and weight to be easily movable, mounted over forklifts or other light vehicles for inspections. In addition, it is possible to operate the entire system with batteries, making it completely independent from external power facilities.

In figure 1.3 the complete system is shown during a laboratory test campaign. The system is made of two pieces having a volume less than 0.1 m^3 as follows:

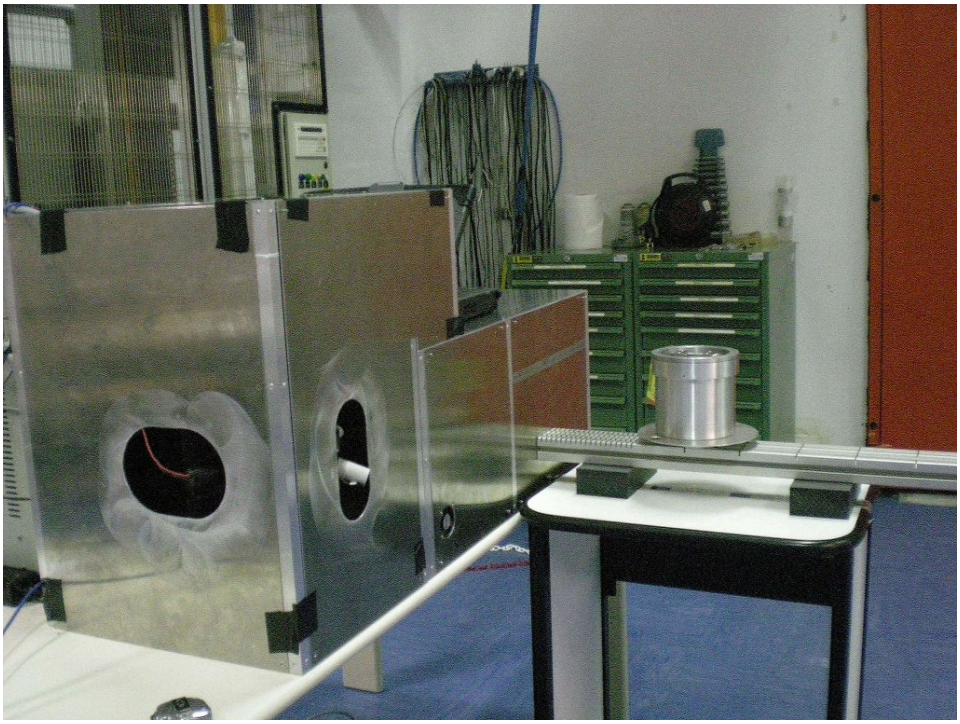

Figure 1.3: SMANDRA during laboratory test

- A passive unit including two gamma-ray detectors (5"x 5" NaI(Tl) and 2"x 2" $LaBr_3$(Ce)) and two neutron counters (5"x 2" liquid scintillator and ^{3}He proportional counter for fast and slow neutrons). The unit hosts batteries, power supplies, front-end electronics and CPU

- An active unit including a portable sealed neutron generator based on the Tagged Neutron Inspection System (TNIS) technique [5].

The first unit can be used in standalone mode as a high efficiency spectroscopic ra-

diometer for the detection of ionizing radiation such as gamma-rays, fast and thermal neutrons to search and identify radioactive material as well as Special Nuclear Material (SNM). It can also be used as detector package connected to the second unit for active interrogation of voxels inside a load by tagged neutron inelastic scattering imaging.

The double use of SMANDRA (active and passive interrogations) sets stringent requirements for the detector choice:

- low background and high efficiency detectors for the identification of weak radioactive sources
- capability of discriminating the two components of the radiation (neutrons and gamma rays) in the passive mode. This is an important feature for the identification of special nuclear material (SNM) sources
- high count rate capability to operate in coincidence with the associated particle counter hosted in the neutron generator.

1.3.1 Passive unit

The internal structure of the passive unit is shown in figure 1.4 and a summary of SMANDRA detectors is reported in table 1.2.

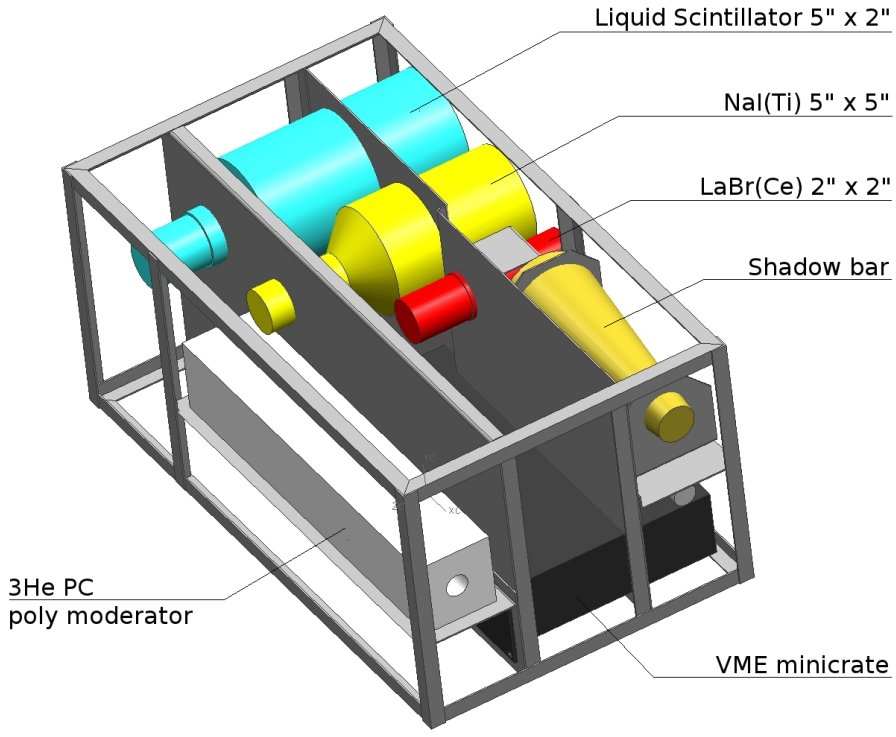

Figure 1.4: Internal structure of SMANDRA passive unit

Detector	**Particle**	**Usage**
NaI(Tl)	γ	Spectroscopy (low backgr. high eff.)
$LaBr_3$(Ce)	γ	Spectroscopy (high resolution)
NE-213	γ, n	n-γ discrimination
^{3}He	n	n threshold alarms

Table 1.2: Summary of SMANDRA detectors

Photon spectroscopy is performed using a high resolution 2"x 2" BrilLanCe^{TM} 380 $LaBr_3$(Ce) detector and a high efficiency large volume 5"x 5" NaI(Tl) scintillator. The $LaBr_3$(Ce) detector offers the ultimate energy resolution for scintillators [6] but it shows some weaknesses. It is presently available only with modest volumes compared to other scintillators, therefore this represents limitation for energetic gamma rays (up to 6 MeV) [7] from inelastic excitation in the active interrogations. Furthemore $LaBr_3$(Ce) suffers from internal activity [8] with some problem in the identification of weak γ sources.

A large NaI(Tl) scintillator has been selected to be used as detector for energetic gamma rays in active investigations as well as high efficiency device in the detection and identification of weak gamma sources with a simple decay scheme, when the energy resolution is not playing an important role.

In this application the scintillation detectors are more advisable respect to semiconductor (like HPGe or CzT) that exibits a much better energy resolution but limited efficiency. The important features of this prototype are flexiblility and trasportability and the use of semiconductors implies the presence of a reservoir of liquid nitrogen or a limitation in autonomy due to the power consumption of mechanical cryosystems.

Table 1.3 shows a short summary of detector performances.

Detector	NaI(Tl) 5"x 5"	$LaBr_3$(Ce) 2"x 2"
Full Energy Efficiency (@4.4 MeV)	0.24	0.25
Peak/Compton ratio	0.55	0.8
Factor of Merit (FM)*	31	5
Time resolution (typical)	2-3 ns	$<$ 1 ns
Space resolution (in AP systems)	10-15 cm	$<$ 5 cm
Energy resolution (@661 keV)	7-8%	$<$ 3.5%
Cost	5-6 kEuro	15 kEuro

**FM is the product of full energy efficiency times the surface of the detector*

Table 1.3: Performance comparison for SMANDRA gamma detectors

Neutron detection is perfomed with a typical organic liquid scintillator (5"x 2" type NE-213) and an ASPECT SN-01 ^{3}He proportional counter. The ability of

detecting fast neutrons becomes relevant in presence of unshielded SNM sources, for this reason a liquid scintillator coupled with a fast PMT tube is the best choice. In this case, the Pulse Shape Discrimination (PSD) [9] technique will be applied to discriminate neutrons from gamma rays. The interest in the detection of fast neutrons is motivated also by the energy dependence of the neutron background [10], as shown in figure 1.5, so that the signal-to-noise ratio is optimized.

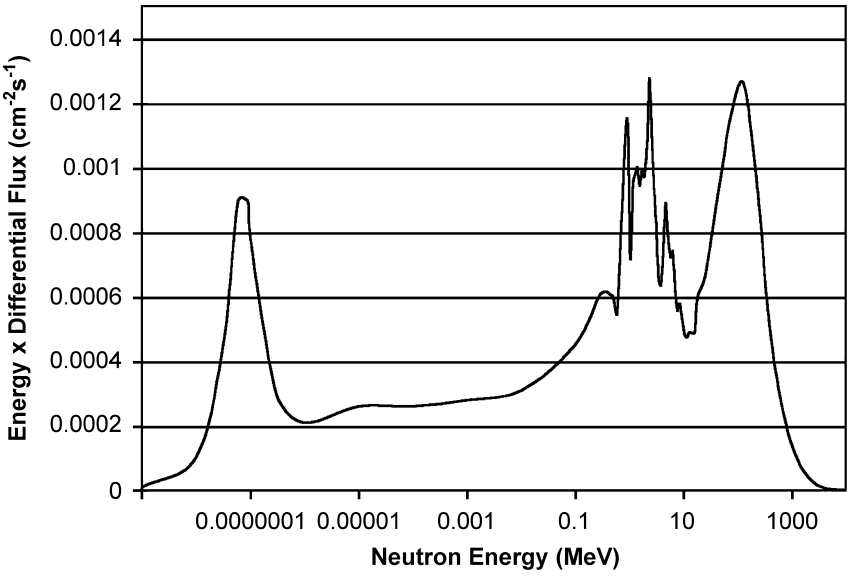

Figure 1.5: Plot of neutron background energy differential flux derived from [11].

The ^{3}He proportional counter with a polyethylene moderator is a typical choice as neutron counter for systems operated in passive mode [12]. This kind of detector is sensible only to thermal neutrons so the function of moderator is to make nearly costant the efficiency of the detector over the entire neutron energy range.

Finally, another important distinctive fact of SMANDRA is the simple electronic front-end based on fast digitizer. The passive unit hosts a prototype VME mini-crate (4 slots) with battery power supply for a complete autonomy of the system. The mini-crate can be configured with the V1718 USB Bridge module. In the minicrate there are also a programmable HV power supply V6533 (6 Ch, 4 kV, 3 mA, 9W) and a fast digitizer V1720 (8 Ch, 12 bit, 250 MS/s). Inside the V1720 4 FPGA (1 FPGA for a couple of channels) are used to implement the Digital Pulse Processing (DPP) algorithms, providing online for each event a reference time, a complete as well as a partial integration of the signal (for PSD analysis), and the possibility of downloading a selected part of digitized signals.

1.3.2 Active Unit

In order to achieve the capability to detect non-radioactive materials, SMANDRA has been extended with a second “active” module containing a neutron generator.

In this configuration the sample becomes a target for the neutron beam, and we register the secondary radiation induced by this bombardment.

The active box is shown together the passive one in Fig. 1.6.

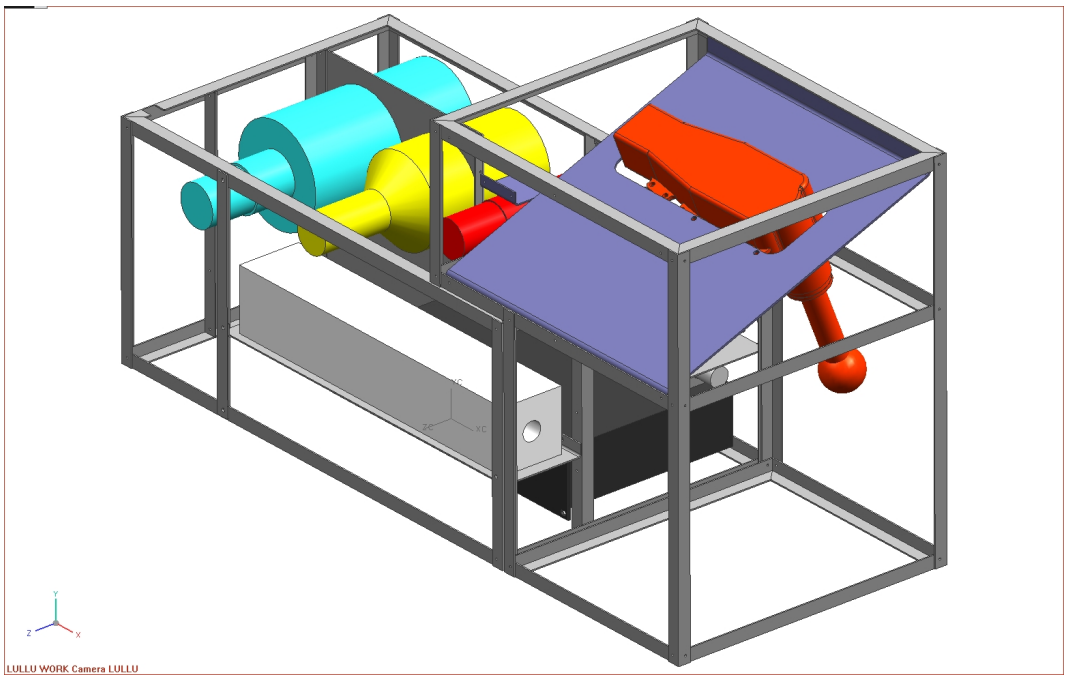

Figure 1.6: SMANDRA active unit with the neutron generator

SMANDRA makes use of a EADS SODERN TPA17 sealed neutron generator, remotely-controlled by a PC to reduce radiation hazard of the operator. Neutron generator emits 10^7 neutron per seconds over the entire 4π solid angle. In the passive unit a shadow bar, made of iron and lead, is added to protect detectors from direct radiation. Furthemore to tag the neutron beam towards the target the TPA17 embeds a YAP(Ce) scintillator for alpha particles that are associated with the neutron production in the T+D reaction inside the neutron generator. This technique called Tagged Neutron Inspection System (TNIS), ensures that only neutrons emitted in a given direction towards the sample will result in a valid event [5]. Figure 1.7 reports the geometry of active inspection. The tagged neutron beam, emitted by neutron generator (B), moves towards the target (C); inside the sample the emission of characteristic γ-ray that hits the detector (A) is induced by neutrons.

Several materials like Carbon, Nitrogen, Oxygen, Iron etc, have a charactheristic γ-ray signature resulting from inelasting excitation of the nuclei [13][14], then it is possibile to recostruct the elemental composition of the sample by analyzing the coincident γ-ray spectrum.

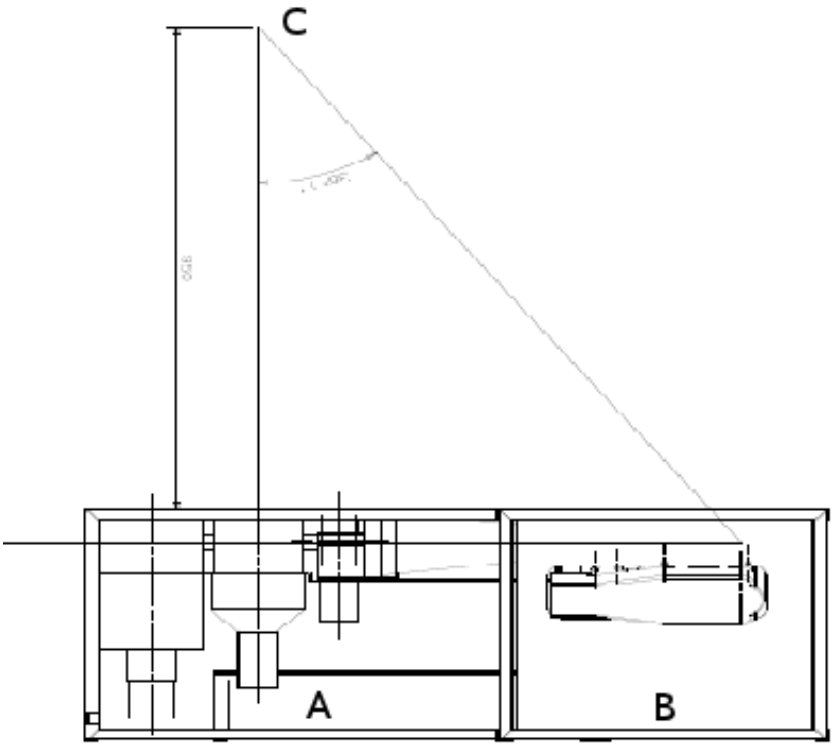

Figure 1.7: Relative position of the detectors (A), the generator (B) and the target (C)

Chapter 2

SMANDRA detectors

2.1 Physics of the detectors

2.1.1 Inorganic scintillator

The detection capability of an inorganic scintillator depends on the structure of the crystal lattice. In a pure inorganic crystal lattice such as NaI(Tl) or $LaBr_3$(Ce), electrons can occupy selected energy bands (see Figure 2.1).

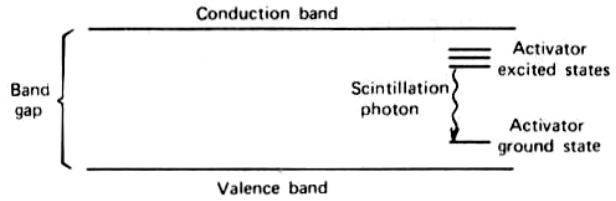

Figure 2.1: Energy band structure of an activated crystalline scintillator

The lower band, called Valence band, represents electrons that are essentially bound at lattice sites. The upper band, called Conduction band, represents electrons that have suffiecient energy to migrate freely throughout the crystal. The forbidden band or Band gap represents the range of energies (usually few electron volts) in which electrons can never be found. When incident radiation hits the crystal, electrons can be elevated to the conduction band leaving a hole in the valence band. The return of those electrons to the valence band causes the emission of scintillation photons. The band gap widths in some pure crystals are such that the wavelenght of resulting emitted photon is too high to lie in the visible region, for this reason small amounts of impurities are added to the crystal (e.g. Tallium is added to NaI in trace amounts) to lower the wavelenght of the emitted photons and maximize scintillation efficiency. The impurities are called *activators*. They create special sites in the lattice that modify the band gap structure. The result is an energy level within the forbidden gap, through this level the electron can deexcite back to the valence band. In this case the energy of the emitted photons is lower

compared to the pure crystal gap and this transition can now give rise to a visible photon, allowing of the detection process. There are three kinds of activator centers:

- *Luminescence centers* in which the de-excitation process give rise to a visible photon that is at the basis of the scintillation process.
- *Quenching centers* in which the transition between excited states and the ground state produces no visible photons. These processes represent loss mechanisms in the conversion of the particle energy to scintillation light.
- *Traps* in which the energy transition to the ground state is forbidden. In this metastable level, the electrons can stay for a long time before acquiring additional thermal energy to raise to a high-lying state from which deexcitation to the ground state is possible. When the high-lying state corresponds to a luminescence center, the delayed light emission is called phosphorescence.

The NaI(Tl) Crystal

NaI(Tl) detector shows an excellent light yield [15] and a large absorption efficiency also for high-energy gamma rays [16] due to the relatively high atomic number of Iodine (Z = 53) and to the crystal's density. It can be produced into a wide assortment of sizes and shapes. The energy response is close to be linear over a large energy range [17]. All these characteristics made NaI(Tl) the standard scintillation material for gamma-ray spectroscopy.

In the SMANDRA system a 5"x5" NaI(Tl) scintillator has been selected. The large size is mainly due to the detection of energetic gamma rays in active investigations and to the detection and identification of weak gamma sources.

Most relevant properties of the NaI(Tl) are shown in Table 2.1.

Density	3.67 g/cm^3
Emission Maximum	415 nm
Decay Constant	0.23 μs
Refractive Index @ maximum	1.85
Hygroscopic	yes

Table 2.1: Properties of NaI(Tl) detector

Figure 2.2 shows the absorption efficiency of NaI(Tl) detectors. The absorption efficiency depends generally on:

- the detector material,
- the linear attenuation coefficient,
- the volume of the crystal,

- its thickness in the direction of the incident radiation.

For a 5"x5" detector the absorption efficiency is always over 80% in the 0.1-10 MeV that is the revelant energy range for SMANDRA.

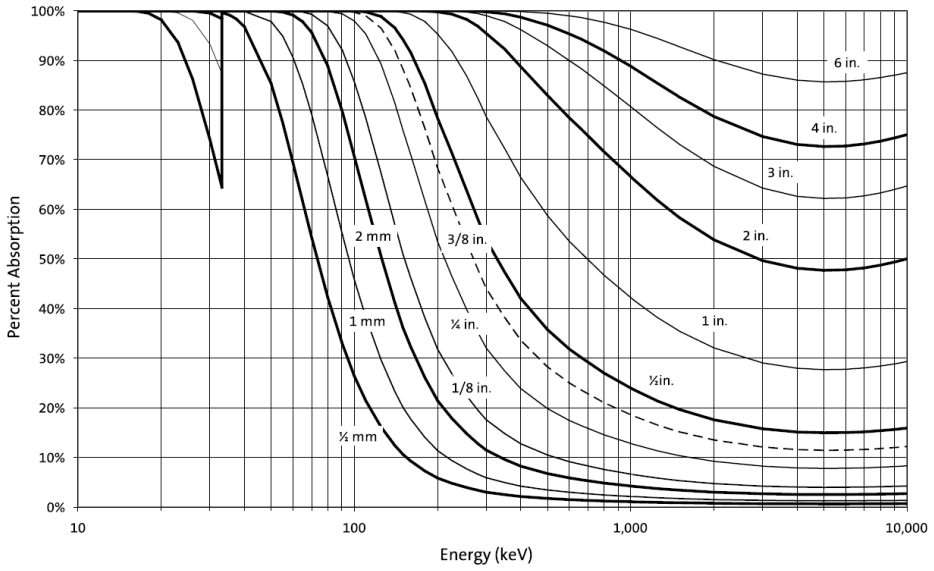

Figure 2.2: Absorption efficiency of NaI(Tl) detector.

Another interesting parameter is the photopeak efficiency. A typical γ-ray spectra includes several structure due to the different iteractions of the incident radiation, e.g. photoelectric, Compton edge, single and double escape, backscattering etc.. Counting the events in the full energy peak is the simplest way to identify radiation source in the natural background. Furthermore it is possible to eliminate some perturbing effects in the laboratory such as scattering from surrounding objects using only full energy peak events. The peak to total ratio for NaI(Tl) detectors of different size is shown in Figure 2.3. The photopeak efficiency is proportional to the atomic number of the detector. Indeed, a lower value of the atomic number and density of the material determines a poor photopeak efficiency. In Figure 2.4 is shown an example of curves for a 3"x3" NaI(Tl) scintillator and 3"x3" PVT plastic scintillator. The photopeak for the plastic scintillator is very weak and is not observed above 60 keV.

The $LaBr_3$(Ce) Crystal

The high-resolution detector of SMANDRA is a 2"x2" $LaBr_3$(Ce) scintillator of the Brilliance series, manufactured by Saint-Gobain, coupled to a standard Hamamatsu R6231 photomultiplier with AS20 voltage divider. Most relevant parameters of the detector are shown in table 2.2.

The $LaBr_3$(Ce) scintillators are generally interesting for γ-spectroscopy measure-

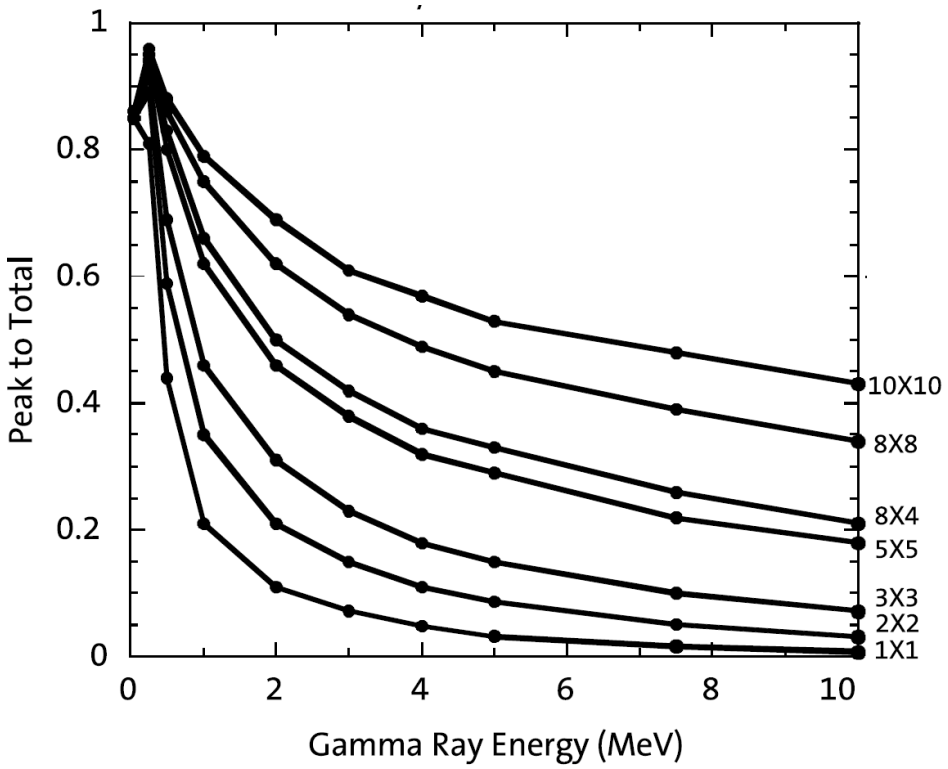

Figure 2.3: Peak to total ratio of NaI(Tl) detectors of different size. The numbers on each curve refer to the scintillatore size. As an example, 10x10 refers to a cylinder scintillator 10 inches in diameter by 10 inches long.[18]

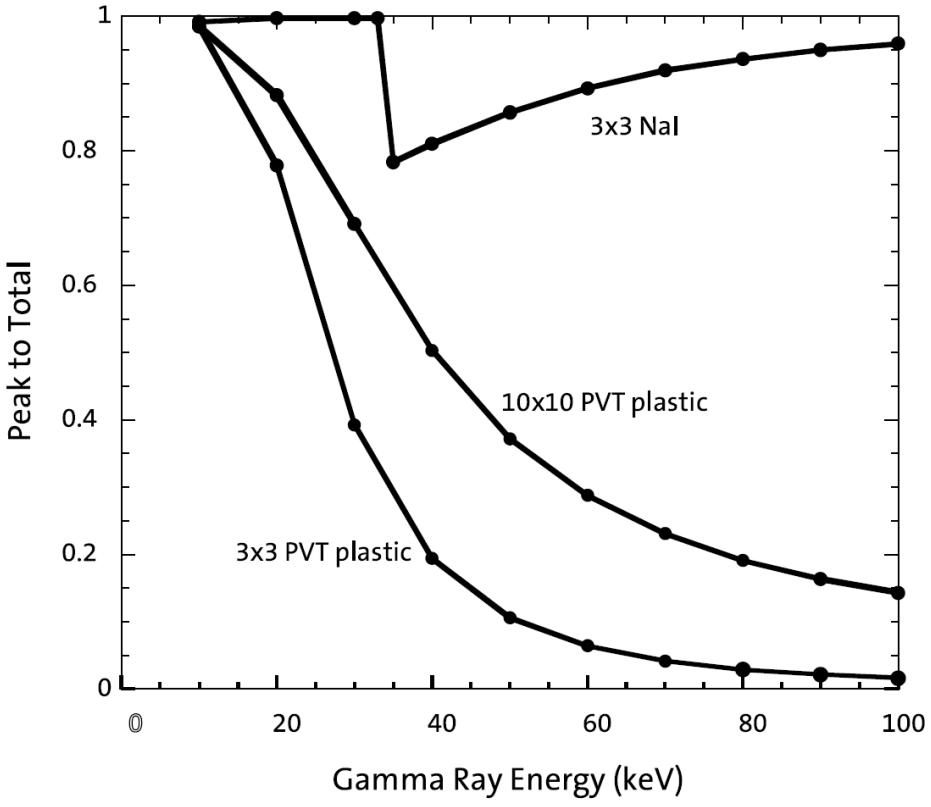

Figure 2.4: Comparison of the peak to total ratio for a 3"x3" NaI(Tl) detector and a PVT plastic scintillator of the same size. [18]

Internal activity peak	1436 keV
Density	5.08 g/cm^3
Melting point	1116 K
Thermal expansion coefficient along C-axis	$8 \cdot 10^{-6} \circ C^{-1}$
Hygroscopic	yes
Wavelength of emission max.	380 nm
Refractive index @ emission max	1.9
Primary decay time	0.016 μs
Light yield	63 photons/keVγ
Photoelectron yield (for γ-rays)	165% of NaI(Tl)

Table 2.2: Properties of $LaBr_3$(Ce) detector

ments due to their good time resolution (of the order of few hundreds picoseconds) and energy resolution (about 3% at 662 keV) [19][20][21]. These detectors, if made with large volumes, are usable for high-energy γ-rays (up to 20 MeV). This is due to the high Z of lanthanum and high density of the crystal. However the high cost has prevented the diffusion for this type of applications [22].

The energy resolution is defined as the width of the distribution at half of the maximum ordinate of the peak (FWHM) divided by the location of the peak centroid. There are a number of potential fluctuation sources that lead to a deterioration of the detector resolution:

- internal instability of the PMT tube,
- temperature dependence of the crystal light yield [23] [24],
- electronic noise within the detector and electronic system,
- statistical contribution arising from the discrete nature of the signal itself.

The latter one is the most relevant source of resolution degradation because in some sense it represents the minimum fluctuation that will always be present in the detector signal, with no correlation with the tecnical quality of the system. The statistical noise arises from the non continuity of the variable representing the charge Q generated within the detector by a quantum of radiation. For example in a scintillation counters, Q represents the number of photon collected by the PMT tube. If the total number of charge carriers is N the statistical fluctuations are characterized by the standard deviation $\sqrt{N}$, then the resolution improves (FWHM decrease) as N is increased. An ideal detector would have as many information carriers generated per event as possibile, so that the limiting resolution would be as small as possible. The dependence of resolution (R) from the energy of incident γ-ray (E) can be predicted simply by noting that:

1. the FWHM of the peak is proportional to the square root of the γ-ray photon energy,

2. the average pulse height produced is directly proportional to E.

$$R = \frac{FWHM}{CENTROID} = K\frac{\sqrt{E}}{E} = \frac{K}{\sqrt{E}} \tag{2.1}$$

This means that the energy resolution is inversely proportional to the square root of the γ-ray energy. Figure 2.5 [25] shows the function $R(E)$ for $LaBr_3(Ce)$ of different sizes and for NaI(Tl). The green line represents the expected curve, the best fit is obtained for $K = 76.3$.

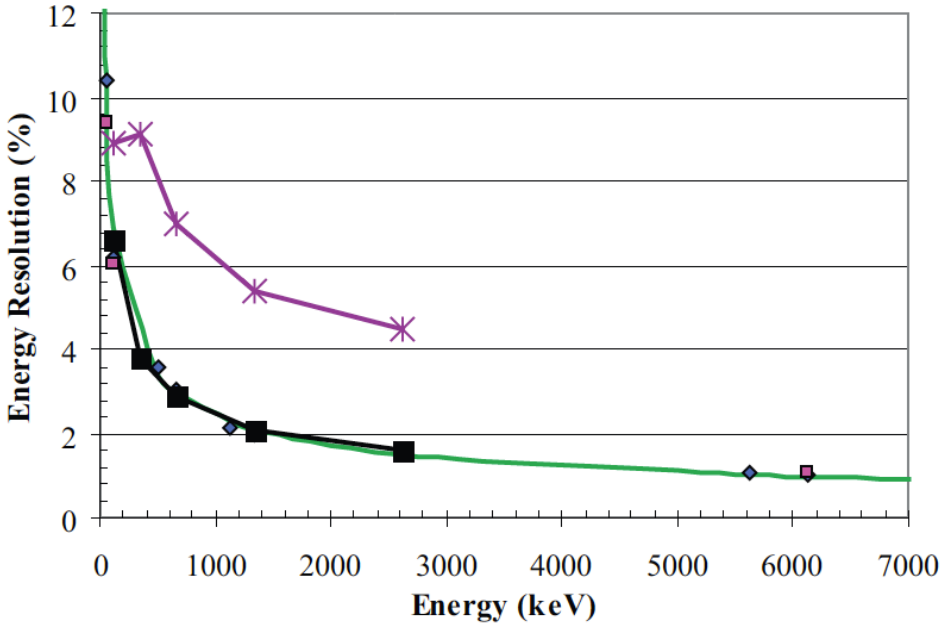

Figure 2.5: Dependency of energy resolution from γ-ray energy of the incident photon. Green line is the expected curve with $K = 76.3$. Black line is a 3"x3" $LaBr_3(Ce)$ detector. Blue diamond is a 2"x3" $LaBr_3(Ce)$ detector. Violet square is a 1"x1" $LaBr_3(Ce)$ detector and violet line is from 3"x3" NaI(Tl) detector.

In Figure 2.5 we can notice that the energy resolution of the NaI(Tl) is three times worse than the $LaBr_3(Ce)$ one [26]. This is due to the $LaBr_3(Ce)$ scintillator, that has 1.6 times the light output and is more than 10 times faster than NaI(Tl) [25]. This can also produce non-linear effects in the PMT that manifests itself in two ways: the FWHM of a peak is better than expected at that energy and the position of higher energy peaks is at lower pulse heigth than expected from a linear extrapolation [7] [27]. In order to minimize non-linear effects, one must select PMT with superior linearity properties, like 8-stage PMTs.

In conclusion, the best resolution achievable by the $LaBr_3(Ce)$ derives from the improved light production per unit of energy compared to NaI(Tl) and from a PMT

with high photocathode quantum efficiency like our R6231 PMTs [28]. It is worth mentioning that the R6231 PMTs have been often used with $LaBr_3(Ce)$ crystal in spectroscopic applications for their high photocathode quantum efficiency but it is a relatively slow device with a large transit time spread not properly suited for optimal fast timing applications.

The $LaBr_3(Ce)$ detector suffers from internal activity [8]. The detector crystal contains a small percentage of the radioactive isotope ^{138}La as well as ^{227}Ac, including several daughter nuclides. Fig. 2.6 ([29]) represents a pulse height distribution showing the internal contamination of the $LaBr_3(Ce)$ detector along with an explanation of the more relevant features in the pulse height distribution. The measurement referred in [29] was made in a low-activity environment.

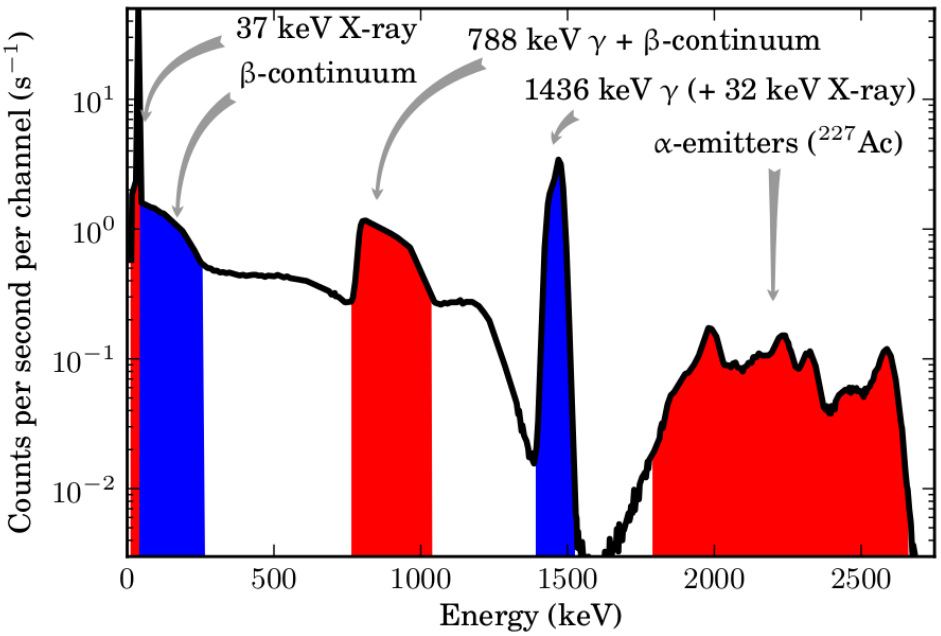

Figure 2.6: Spectrum from the internal contamination of the $LaBr_3(Ce)$ detector.

The main consequence of the internal activity is the presence of a multiplet at 1436 keV resulting from the decay of ^{138}La (half-life of $1.05 \cdot 10^{11}$) into ^{138}Ba by electron capture (66.4%). The multiplet is an effect of the combination of 1436 keV photons and 32 keV X-ray photons from ^{138}Ba. Another possibility is self-activity due to the ^{138}La decays through β-decay to ^{138}Ce (33.6%). This branch releases a 789 keV γ coincident with a β, which has an endpoint energy of 255 keV. In this case there is the possibility that the 789 keV γ-photon is completely absorbed in the crystal. The resulting effect is that the β-continuum is shifted to a higher energy creating the structure between 0.75 and 1 MeV [29][30]. Another contribution is given by α-particles emitted from ^{227}Ac with daughters. The energy of this particle is in the order of several MeV but the peaks in the pulse height distribution appears in the energy range of 1.5 to 3.0 MeV beacuse the light quenching for α-particles in

the $LaBr_3(Ce)$ is lower than for β-particles and γ-photons [31][32].

A good use of $LaBr_3(Ce)$ detectors requires an accurate determination of the self-activity, particularly when events are collected at low rates (few events per minute). In fact, spurious peaks due to internal activity might affect the identification and the measurement of the peaks of interest. On the other hand, if the internal activity rate is negligible compared to the true event rate and/or can be eliminated with the data-analysis (as in coincidence experiments), it can be used as an intrinsic calibration source useful to monitor gain drifts. This is an essential point in the measurement of continuum spectra.

Finally, in Figure 2.7 are shown the absorption efficiency (left) and peak to total ratio (right) for $LaBr_3(Ce)$.

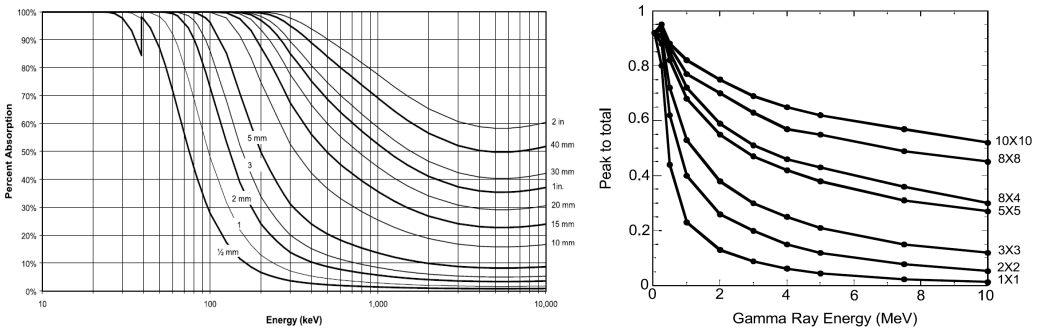

Figure 2.7: Absorption efficiency (left panel) and peak to total ratio (right panel) for $LaBr_3(Ce)$ detector.

Comparing figures 2.7 and 2.3, we can notice that for NaI(Tl) and $LaBr_3(Ce)$ crystal of the same size, $LaBr_3(Ce)$ is better both in terms of total efficiency and in the peak to total ratio.

2.1.2 Liquid scintillator

Liquid scintillators have many applications in neutron and gamma detection for their distinctive features. Thanks to different base materials, they offer the possibility of pulse shape discriminations, high flash point, performance at low or high temperatures and increased neutron or photon cross sections. Liquid scintillator is produced by dissolving an organic scintillator in an appropriate solvent. Sometimes a third costituent is added as wavelenght shifter to tailor the emission spectrum to better match the spectral response of common photomultiplier tubes. Most of these liquids suffer for the presence of oxygen in the solution. Oxygen operates as a strong quenching agent and can lead to the reduction of fluorescence efficiency. For this reason the treatment of scintillation liquid must be done with great care. Normally the solution is sold in appropiate selaed glass containers from which most of the oxygen have been purged.

The fluorescence process in liquid scintillators depends on the transitions in the energy level structure of a single molecule and therefore can be observed from a given molecular species independent on its physical state. This behaviour is in contrast with crystalline inorganic scintillators such NaI(Tl), which require a regular crystalline lattice as a basis for the scintillation process. For example anthracene, one of the most used material in organic scintillators, is observed to fluoresce as either a solid, vapor or as part of a multicomponent solution.

This organic molecules have a certain symmetry properties which give rise to what is known as a π-electron structure. In Figure 2.8 the π-electronic energy levels of this type of molecules is reported as an example.

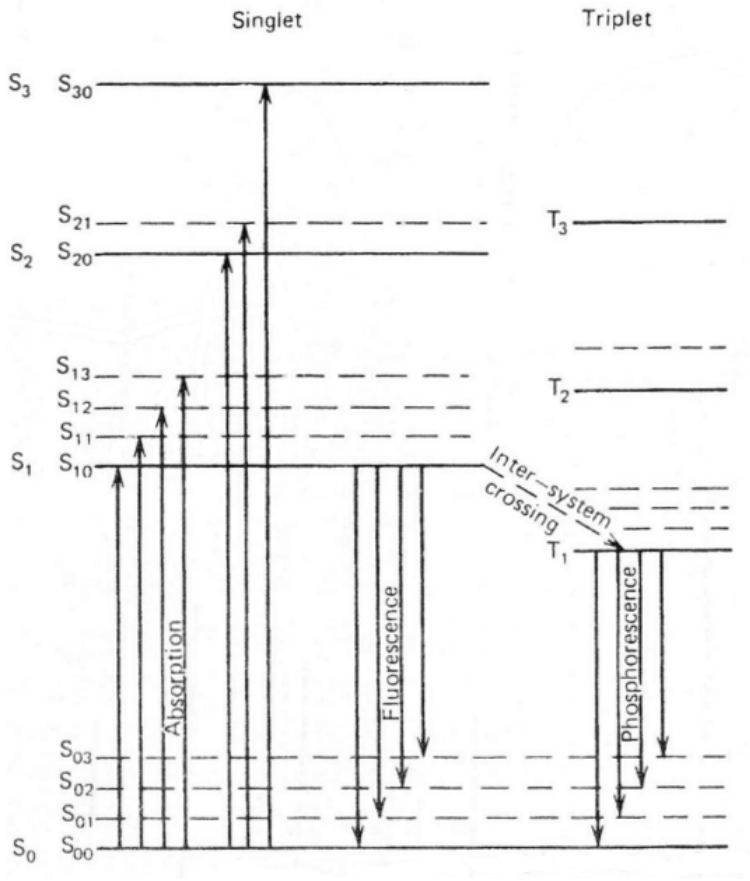

Figure 2.8: Energy levels of an organic molecule with π-electron structure

There are a series of singlet state (spin 0) labelled as $S_0, S_1, S_2, ...$ and a similar set of triplet state with spin 1, labelled as $T_1, T_2, T_3, ...$. Typical energy spacing bewteen the ground and first level of the singlet state ($S_0 \Rightarrow S_1$) is 3-4 eV. Each of these electronic configurations is further subdivided into a series of much finer spacing (typical 0.15 eV) which correspond to various vibrational states of the molecule.

When a charged particle passes close to the molecule, it transfers part of its kinetic energy that is absorbed. The higher states (S_2, S_3,...) are quickly deexcited

in few picosecond to the S_1 electron state through internal radiationless conversion as well as states with excess vibrational energy (such S_{11} or S_{12}) that are not in thermal equilibrium with its neighbors. Therefore the net effect of an excitation process is the population of the S_{10} state from which the prompt scintillation light is emitted with a transition to S_0 state. In most organic scintillators, prompt fluorescence is relatively fast in the order of few nanosecond.

Another process, called *intersystem crossing*, can convert some S_1 excited singlet state into triplet state. Triplet state T_1 has a lifetime much longer than the singlet S_1 state and deexcitation produces delayed light emission characterized as phosphorescence. Furthemore, some molecules may be excited back to the S_1 state and subsequently decay through normal fluorescence. This process represents the origin of the delayed fluorescence. Compared with the prompt decay time of a few nanoseconds, the slow component will typically have a characteristic decay time of several hundred of nanosecond. The importance of slow component derives from the dependence of this light with the nature of the exciting particle. One can make use of this correlation to discriminate between different particle like neutron, gamma, alpha etc. that have deposited the same energy in the detector. In fact, the slow component fraction depends primarly on the rate of energy loss dE/dx of the exciting particle. As shown in Figure 2.9 the tail of the signal is greater for heavy particle with large dE/dx. It is worth mentioning that neutrons do not release energy directly but the detection is based on elastic scattering of neutrons by light nuclei, in the same way γ-ray trasfer a portion of kinetic energy throught compton scattering.

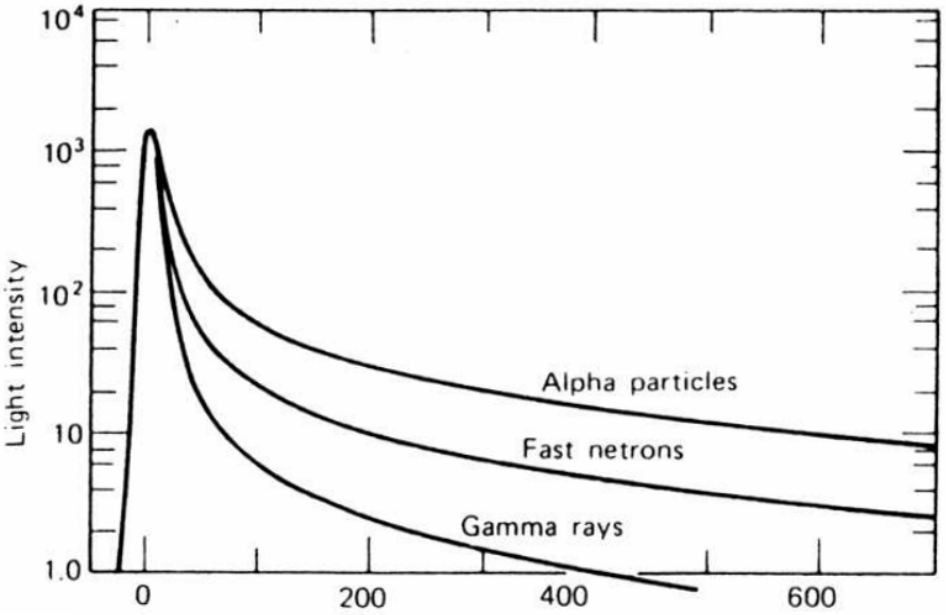

Figure 2.9: Pulse shapes in stilbene for different radiation's types [33].

This important features is called *Pulse Shape Discrimination* (PSD) and is widely

applied to eliminate γ-ray events when an organic scintillator is used as neutron detector [34][35][36].

NE-213

One of the historical scintillator for neutron spectroscopy was the liquid scintillator NE-213 [37][38][39], manufactured in the past by Nuclear Enterprises Limited and today by Bicron with the name of Saint-Gobain Scintillators or by Elyien Technologies. It consists of xylene, activators, the organic compound POPOP (as a wavelenght shifter) and naphthalene, which is added to improve light emission. The density of NE-213 is about 0.874 g/cm^3 and its composition is taken to be $CH_{1.21}$.

Its popularity is mainly due to its excellent pulse shape discrimination properties, comparable with that of Stilbene and Anthracene [40]. It is usually encapsulated in an aluminium or glass container, which allows the manufacturer to adapt its shape in order to meet different requirements.

Density	0.874 g/cm^3
Refractive index	1.508
Light output (% Anthracene)	78%
Decay time (fast)	3.7 ns
Wavelength of maximum emission	425 nm
Ratio of H to C atoms	1.213

Table 2.3: Properties of SMANDRA NE-213 detector

SMANDRA make use of an original 5"x 2"NE-213 detector, although in this work a number of test have performed with modern EJ-301 and EJ-309 scintillators.

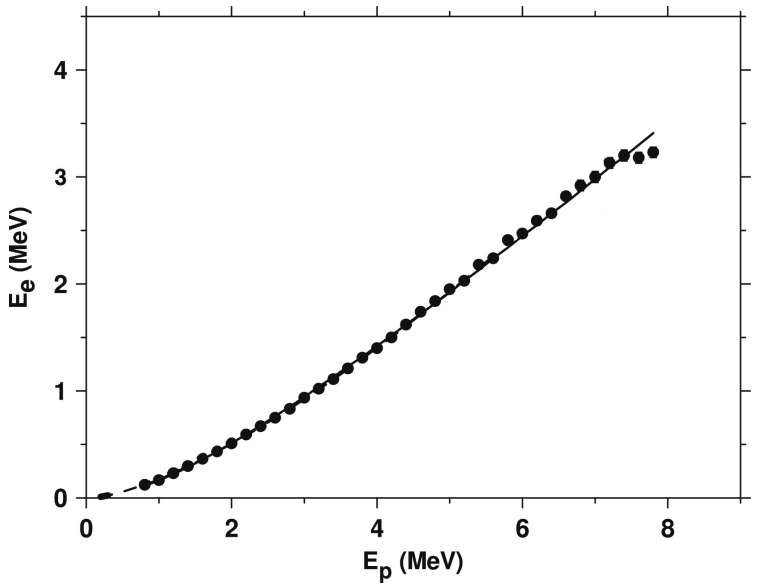

Figure 2.10: The light output for the LS-301 detector [41]. Points are the experimental data and the solid line is Eq. 2.2, equivalent to the NE-213 scintillator

As discussed in Sec. 2.1.2 neutrons incident on an organic scintillator produce light indirectly, mainly via the knock-on protons from elastic collisions with hydrogen. In order to interpret a measured neutron pulse height spectrum, the relationship between proton energy and light-output must be known. The light output function for protons is usually described by equation 2.2:

$$L(E_p) = L_0 \frac{E_e^2}{E_e + L_1} \tag{2.2}$$

where E_e is the electron energy and L_1,L_0 are fitting parameters. For NE-213 scintillator, thre reader can refer to [42][41][43][44]. We report in Figure 2.10 a recent work of Kornilov et al. [41] in which the relationship between the light output versus proton recoil energy for a LS-301[1] detector is shown.

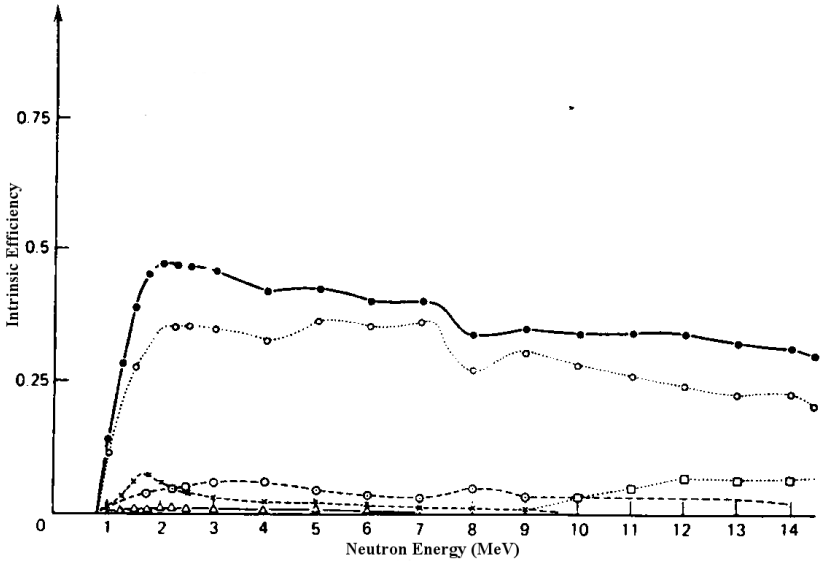

Figure 2.11: The calculate efficiency of a NE-213 liquid scintillator (cylinder:1.5"x4") for a discrimination level of 0.81MeV. Identification of the symbols is the following: • combined efficiency from all processes; ∘ single hydrogen scattering; × n-H, n-H double scattering; ⊙ n-C, n-H double scattering; △ n-C, n-H, n-H triple scattering; □ (n,α) and (n,n')3α reaction.

The detection efficiency of a device based on recoil nuclei is proportional to the scattering cross section of the nuclei and it depends on the shape and thickness of the detector and on the energy threshold. At low neutron energies the cross section of n-H reactions are predominant. Over 8-9 MeV other reactions must be considered, as n-C or n-H double or triple scattering. In Figure 2.11 is shown the calculated efficiency of a NE-213 detector [45].

[1]LS-301, produced by SCIONIX, is based on the EJ-301 scintillator, equivalent to the NE-213 neutron detectors

2.1.3 Proportional counter

Proportional counters are a type of gas-filled detectors, based on the phenomenon of *gas multiplication*. Tipically a proportional counter is a cylinder with a thin wire placed along the central axis. This wire serves as anode while the cylinder, often made of stainless steel, is used as cathode and conventionally grounded. In figure 2.12 a basic structure of a proportional counter is shown. A positive high voltage

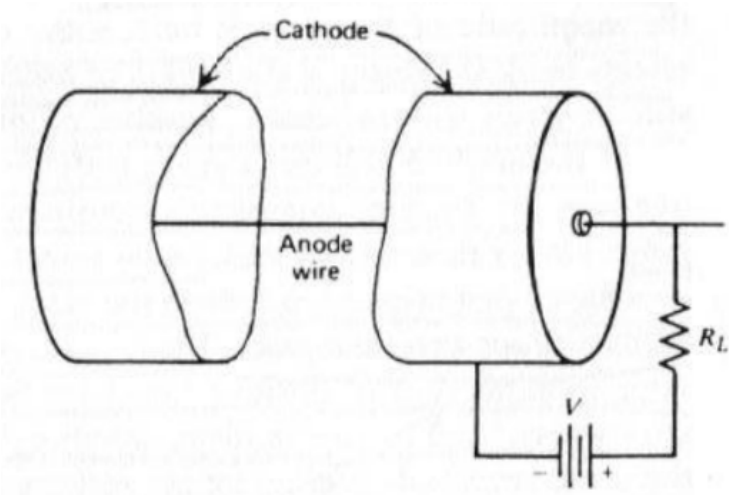

Figure 2.12: Basic elements of a proportional counter

must be applied to attract the electrons from the gas toward the central wire. The choice of the voltage is important because *gas multiplication* is a consequence of the electric field. When a pair ion-electron is created by incident radiation, they drift to their collecting electrodes acquiring kinetic energies beacuse of the applied voltage. If the kinetic energy is greater than the ionization energy of molecule it is possible to create, in another collision, an additional ion pair. This new electron released is accelerated by the electric field, contributing to the creation of new free electrons in a cascade process, called *Townsend avalanche*. There is a threshold value of the field above which this secondary ionization will occur, typical value at atmosferic pressure is of the order of 10^6 V/m. Under proper conditions, the number of secondary ionization events can be kept proportional to the number of primary ion pairs formed and the total number of ions can be multiplied by a factor of many thousand, reducing the need of external amplifiers.

Helium-3 detector

^{3}He proportional counters utilizes the ^{3}He(n,p)^{3}H reaction for the detection of neutrons:

$$^3\text{He} + \text{n (thermal)} \rightarrow \text{p} + {}^3\text{H}$$

In an ideal large detector, one would expect each thermal neutron reaction to deposit 764 keV in the form of kinetic energy of triton (191 keV) and proton (573 keV). The range of this reaction products is not always small compared with the dimension of the tube. As a consequence the wall effect [46] is important for conventional Helium-3 detector. In Figure 2.13 is shown an expected pulse height spectra for a typical Helium-3 detector. The two steps correspond to the maximun kinetic energy of proton and triton.

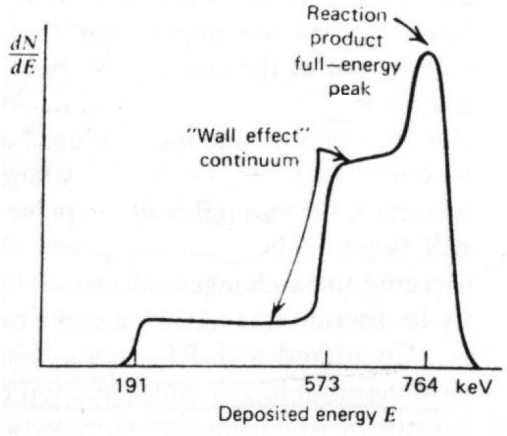

Figure 2.13: Typical pulse height spectrum for a ^{3}He with significant wall effect

Many methods have been used to reduce this effect. The first obvious step is to build the counter with a diameter as large as possible so that most iteractions occur far away from the wall. Another possibility is to increase the pressure of the gas and/or introduce a second heavier component, like krypton, to reduce the range of reaction products.

The energy dependence of cross section in case of ^{3}He follows the relation $1/v$ (v = neutron velocity) up to 0.2 MeV as shown in Figure 2.14, resulting in greater efficiency at lower energies. For thermal neutrons the value of cross section is 5330 barns.

In SMANDRA a shielding of polyethylene is added to slow down fast neutrons to a lower energy value where the detector efficiency is greater. As shown in Figure 2.15 ([47]) the efficiency of a unmoderated tube drops by over four orders of magnitude between few eV and 10 MeV.

2.2 Neutron Generator

Small neutron generators using the deuterium (^{2}H) - tritium (^{3}H) reaction are the most common accelerator based neutron sources. They offer a surprising technology, because they can supply a neutron beam of high flux from a small source. Thus, neutron generators based on those reactions can be used as a powerful tool in several

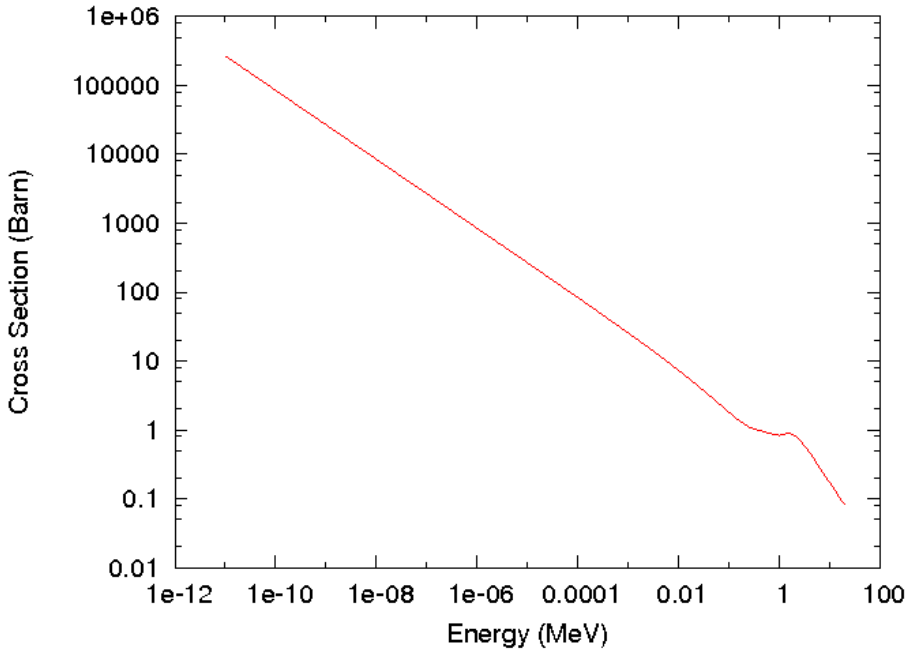

Figure 2.14: Total cross section for ^{3}He(n,p)^{3}H reaction

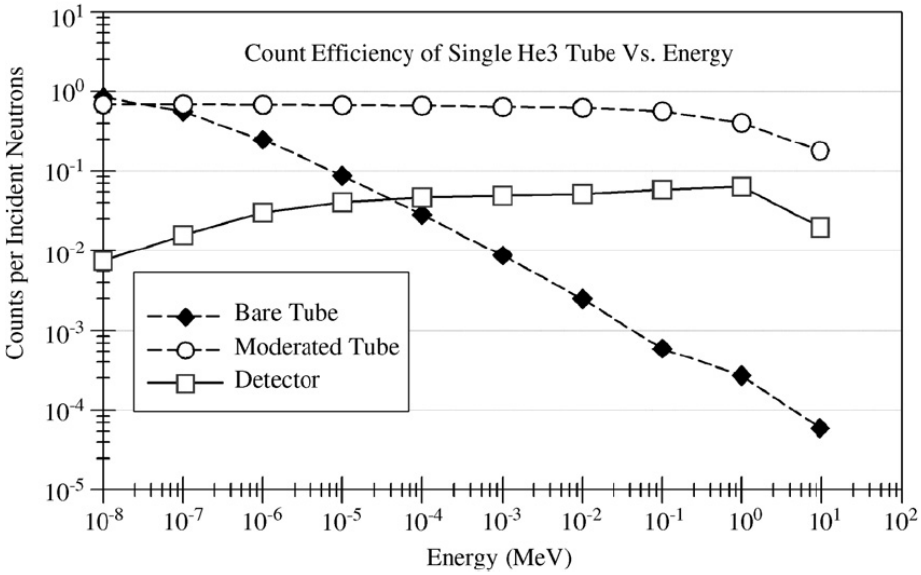

Figure 2.15: Black diamonds show the response of a single unmoderated ^{3}He neutron tube in counts per incident neutron as a function of incident neutron energy, open circles are the response of a moderated tube, and the open squares are the response of a moderated detector assembly.

fields in which there is demand of a beams of neutrons.

The operation's principle is simple, a high-voltage is applied to extract a $^2H^+/^3H^+$ beam from an ion source and to accelerate it towards the target where neutrons are produced in DT, DD, or TT collisions.

$$^2H + ^2H \rightarrow ^3He + n \quad Q = 3.27 \text{ MeV}$$
$$^2H + ^3H \rightarrow ^4He + n \quad Q = 17.59 \text{ MeV}$$

$^2H + ^3H$ reaction has the largest maximum cross-section of 5.0 Barn because the neutron in excess on the tritium nuclide increases the size of nucleus and therefore the cross section of fusion reaction. Maximum cross-section of this reaction for energies of incoming particle below 1 MeV is reached at the energy of 130 keV for deuterium ($^2H + ^3H$) and 195 keV ($^3H + ^2H$) for tritium. Table 2.4 reported fusion energy release (Q), maximum cross section (in Barns) for energies below 1 MeV (σ_{max}) and the neutron kinetic energy (in MeV).

Reaction	Q (MeV)	σ_{max} (barn)	E_n (MeV)
$^2H + ^2H \rightarrow ^3He + n$	3.27	0.09	2.5
$^2H + ^3H \rightarrow ^4He + n$	17.59	5.0	14.1

Table 2.4: Some important parameters of the fusion reactions

Neutrons produced from the $^2H + ^3H$ reaction are emitted isotropically from the target, instead neutron emission from the $^2H + ^2H$ reaction is slightly peaked in the forward (along the axis of the ion beam) direction. In both cases, the He nucleus is emitted in the exact opposite direction of the neutron.

The basic design of a modern compact accelerator neutron generator (an example is shown in Figure 2.16) does not vary from those of other particle accelerators. It consists of a source to generate positively charged ions; one or more structures to accelerate the ions (usually by using a voltage between 80-180 kV); a metal hydride target loaded with either deuterium, tritium, or a mixture of the two; and a gas-control reservoir, also made of a metal hydride material.

The most common ion source used in neutron generators is a cold-cathode also called Penning ions sources [48]. This simple ion source consists of a hollow cylindrical anode (usually biased 12 kV) with cathode plates at each end of the anode (usually at ground potential). An external magnet is arranged to generate a coaxial field of several hundred gauss within the ion source. When deuterium and/or tritium gas is introduced into the anode at a pressure of 1 Pa, the electric field between the anode and cathodes ionizes the gas. Electron confinement is established in this plasma by the orientation of the electric and magnetic fields, which forces the electrons to oscillate back and forth between the cathode plates in helical trajectories. Although some low-energy electrons are lost and strike the anode (which creates

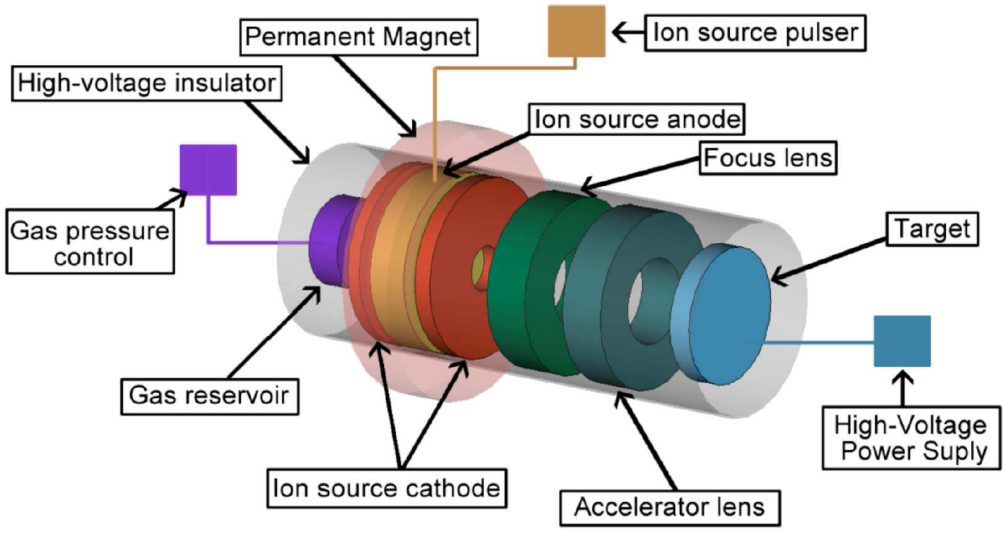

Figure 2.16: Illustration of a neutorn generator with a Penning ion source

more secondary electrons) most remain trapped and ionize more gas molecules to sustain the plasma. The ions are not similarly trapped, and when they strike the cathodes, they also release secondary electrons, which enter the plasma and help sustain it. Ions can escape the chamber into the acceleration section of the tube through a hole at the center of one of the cathodes, called exit cathode.

There are other types of ion sources that are used in industrial applications, for example hot-cathode sources, magnetrons, and radiofrequency ion sources. However, the simple design and durability of the Penning ion source have made it the most commonly used in industrial neutron generators [49].

TPA17 Neutron Generator

The compact Sodern GENIE APT 17 is the smallest portable neutron generator dedicate to elemental analysis using the associated particle imaging (API) technique. Elemental imaging using the API technique is based mainly on inelastic scattering reactions. The Deuterium - Tritium (DT) reaction in the tube produces a 14 MeV neutron and an associated alpha particle (with energy of 3.5 MeV) emitted at the same time and in the opposite directions. The detection of the alpha particle can be done with a segmented (multipixel) detector array [50] that gives the direction of the correlated neutron emitted in a narrow beam. Neutron generators with built-in particle detectors are becoming very popular for identification of the content of different objects with high sensitivity and position resolution [51] [52]. The neutron collides with a nucleus of the material under study and produces a γ-ray [13][14], whose time of arrival at the detector can be precisely measured. This is therefore a Time-of-Flight (TOF) method that allows to determinate the distance traveled by

the neutron (as both the speed of the neutron and of the gamma are known) [53]. As its direction is also known, three-dimensional spatial resolution of objects can be provided. A schematic diagram of API technique is shown in Fig. 2.17 and main features are reported in Table 2.5.

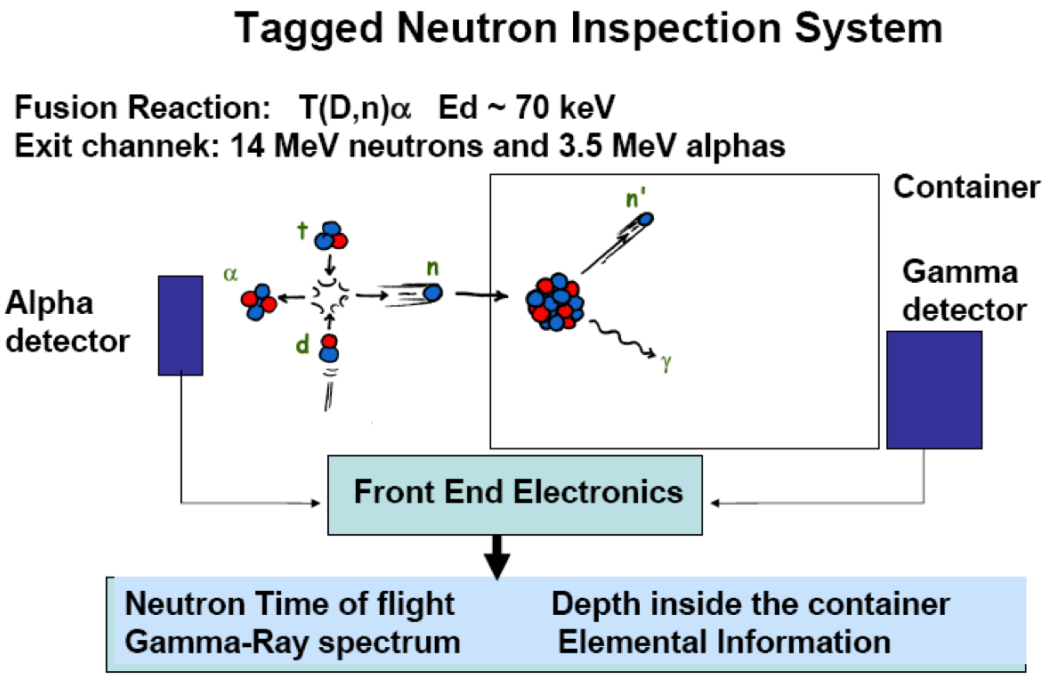

Figure 2.17: Schematic diagram of Tagged Neutron Inspection System technique for non-destructive inspections with neutrons.

Neutron Energy	14.1 MeV
Neutron emission 4π	10^8 n/s
Alpha detector	YAP(Ce)
Size	400x200x400 mm (LxWxH)
Weight	5.7 Kg
Accelerator Voltage	90 kV
Maximum Beam current	150 μA
Typical life time	5000 hours at 10^7 n/s

Table 2.5: Techical specification of Sodern GENIE TPA 17

YAP:Ce

In the TPA17 neutron generator a small inorganic crystal is used as α-particle detector: Yttrium Aluminium Perovskite activated by Cerium (formula $YAlO_3$:Ce, abbreviated YAP:Ce) [54][55]. Due to the low spatial resolution achievable with a single γ-detector and for the small dimension of the analyzed sample, it is not used a multipixel detector. The YAP(Ce) detector is coupled with an external HAMA-

MATSU R1450 photomultiplier, and the output signal is read by the same VME electronics of the SMANDRA system. Most relevant parameters of the detector are shown in Table 2.6.

Density	5.37 g/cm^3
Refractive index	1.93
Light output (% NaI)	40%
Decay time (fast)	25/30 ns
Wavelength of maximum emission	370 nm

Table 2.6: Properties of YAP:Ce detector

Chapter 3

Detector Characterization

This chapter describes the laboratory characterization of the detectors used in SMANDRA system. Initial tests were done with traditional NIM electronics followed by the new digital electronics based on fast digitizers. We will compare the two type of read-out.

3.1 NaI(Tl)

The SCIONIX NaI(Tl) 5"x5"scintillator is used in SMANDRA both in passive and active mode, as a high efficiency detector for searching and identifying radioactive sources or to detect nuclear photons emitted from light nuclei (C, N, O) when they are bombarded by neutrons in active configuration.

It is therefore necessary to individuate a "working point" that allows good energy resolution and linearity in a range of 0.1 - 2 MeV for passive measurements, together with a good time resolution and the possibility of sustain high counting rates in active mode when the energy range is extended up to 8 MeV.

3.1.1 Energy Resolution

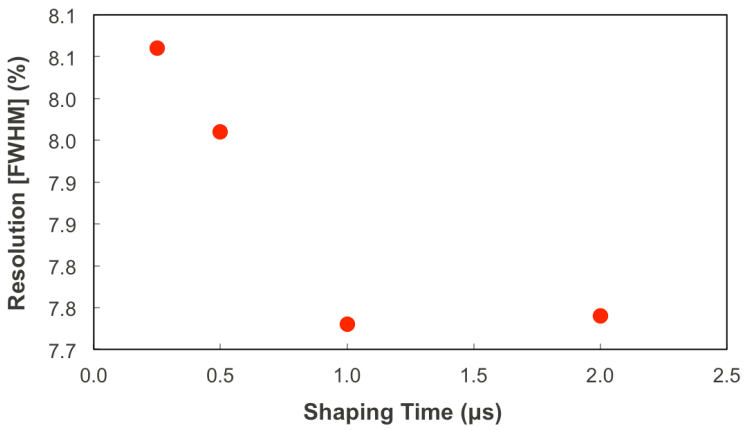

Figure 3.1: Relation between shaping time and resolution (FWHM) in NaI(Tl)

Initial tests have been carried out to determine working condition using standard NIM electronics (typically EGG ORTEC modules). First run selects the best shaping time (ST) of the spectroscopic amplifier with a ^{22}Na, with the detector operating at a voltage of 700V. The best energy resolution is obtained with a ST of 1 μs as shown in Figure 3.1. An energy resolution of 7.7% for the 511 keV full energy peak is comparable with values reported in literature, as in Figure 2.5 [25].

3.1.2 Resolution at high energies

Resolution tests at high energies were performed with a AmBe source. A typical resulting spectrum is shown in Fig. 3.2.

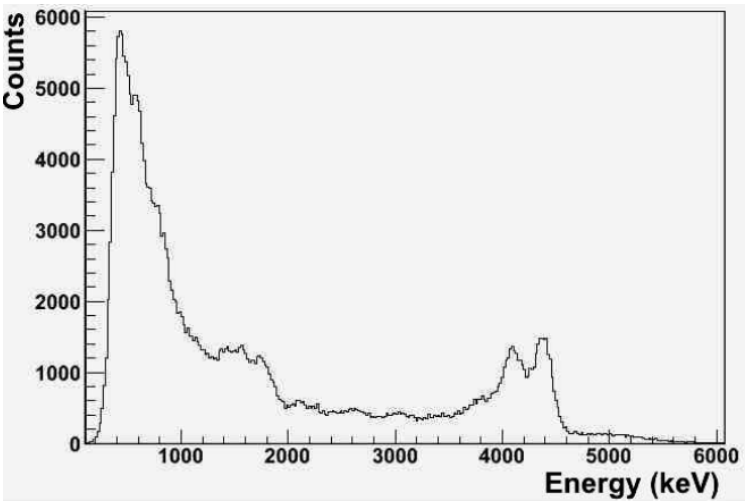

Figure 3.2: AmBe spectrum taken with NaI(Tl)

The spectrum, calibrated with the ^{22}Na source, presents a peak at an energy of 4.4 MeV, preceded by a structure around 4.0 MeV corresponding to first photon escape. The energy resolution of the peak at 4.4 MeV is about 5.5%, mainly caused by Doppler Broadening [56]. This is due to the fact that the 4.4 MeV gamma ray is produced by the recoiling nucleus in the reaction ^{9}Be(α,n).

3.1.3 Time resolution

The time resolution of the detector was studied by measuring gamma-gamma coincidences with a ^{22}Na soruce. An auxiliary detector, a fast plastic scintillator EJ-228 2"x 2"coupled to the PMT XP2020, was used. Intrinsic time resolution of EJ-228 is about 300-500 ps [FWHM] with a threshold between 0.2 and 1 MeV.

First set of measurements was dedicated to find the optimal value of the Constant Fraction Time Discriminator (CFTD) delay (Ortec Mod. 935). Results in Fig. 3.3 show that it is possibile to get resolutions of the order of 3.5 ns [FWHM] with minimum threshold on plastic scintillator and a threshold of 500 keV on the NaI(Tl) with a delay of 22 ns.

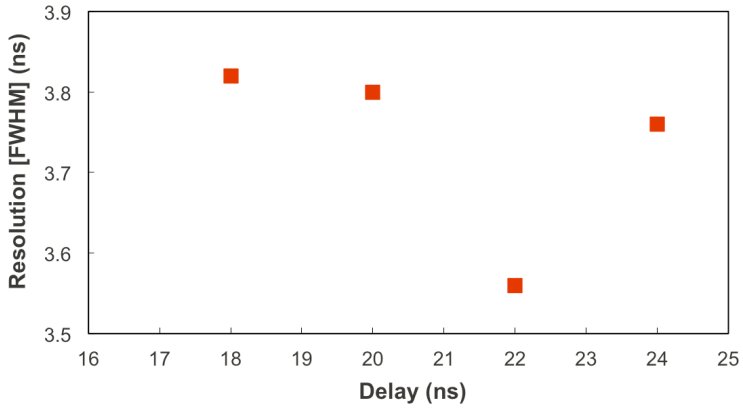

Figure 3.3: Relation between delay and time resolution in NaI(Tl)

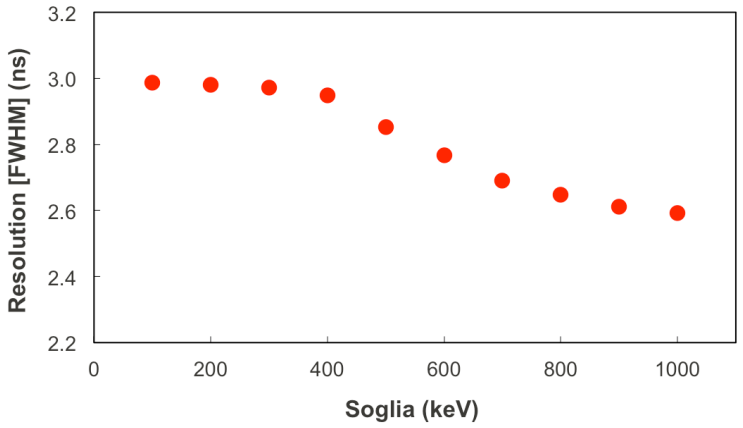

Figure 3.4: Relation between threshold and time resolution in NaI(Tl)

It is noticeable that for active inspections it is recommended a resolution of 2 ns, corresponding to about 10 cm of spatial uncertainty for 14 MeV Neutrons. Obviously, this resolution is related to photons with energy greater than 1 MeV. Analyzing gamma-gamma coincidences with the ^{60}Co in function of NaI(Tl) CFTD threshold (Fig. 3.4) we note that resolution decreases lower to 2.6 ns in case of signals in range 1-1.3 MeV. Consequently it is possible to expect better performances in active interrogations, near to the optimal value of 2 ns.

3.1.4 Count rate capability

The degradation of the NaI(Tl) performance with an increase of the count rate was studied. Gamma-gamma coincidences have been measured with the ^{22}Na source and the fast plastic scintillator. The NaI(Tl) detector was loaded with a second source (^{137}Cs) not seen by the plastic scintillator. In this way, we sent always the same signal to the DAQ, the coincidences between NaI(Tl) and plastic, corresponding to different count rates in the NaI(Tl).

We registered energy resolution and relative shift (with respect to the lowest rate measurements) as a function of the count rate. We repeated the measurements with two different NIM amplifiers (Figures 3.5 and 3.6).

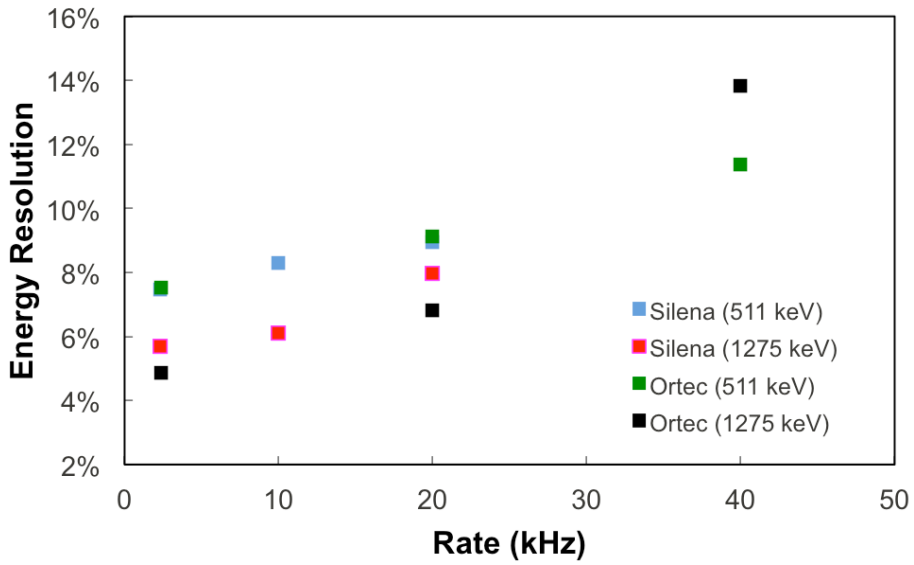

Figure 3.5: Relation between resolution and rate in NaI(Tl) for the two peaks of ^{22}Na source.

It is noticeable a clear shift in amplification of about 10% at 40 kHz, with a clearly correlated worsening of the energy resolution.

As a conclusion, the preliminary tests with NIM electronics for the NaI(Tl) detectors are:

- operating voltage 700 Volt,

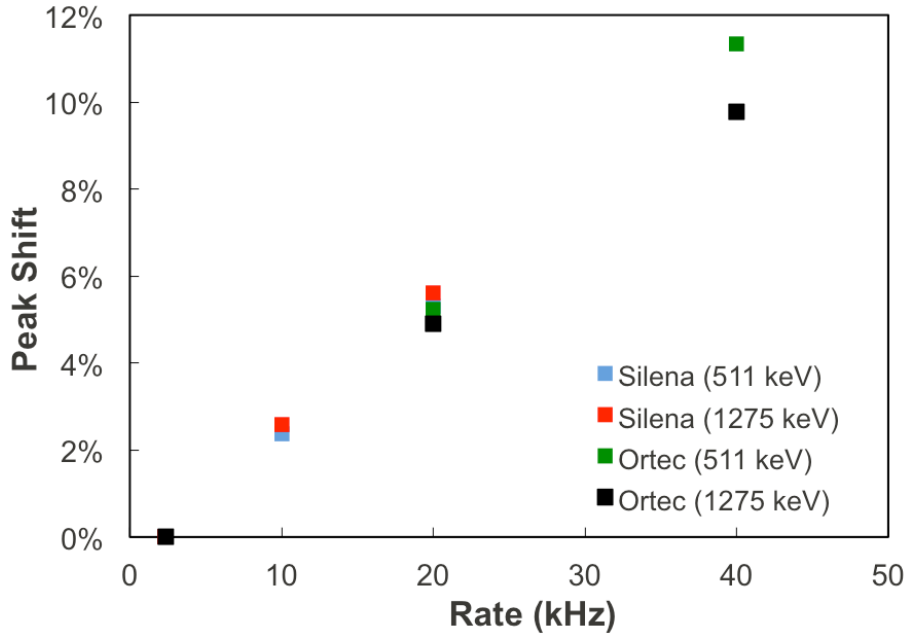

Figure 3.6: Relation between peak shift and rate in NaI(Tl) for the two peaks of ^{22}Na source.

- best resolution with a Shaping time of 1 μs,
- good linearity in the required energy domain,
- gain drift and loss of resolution at high rate ($\sim$ 40 kHz),
- best CFTD external delay of 22 ns,
- time resolution about 2.6 ns with 1 MeV threshold.

3.2 $LaBr_3(Ce)$

St. Gobain's 2"x 2" $LaBr_3(Ce)$ detector will be used in SMANDRA both in passive and active mode. Therefore we looked for good resolution and linearity in a range of 0.1 - 2 MeV for passive measurements, together with a good time resolution and the possibility of sustain high counting rates for active interrogations.

3.2.1 Energy resolution

First measures determined the optimal value of the signal shaping time to be used in the NIM amplifier, operating the detector at HV = 750 Volt with ^{22}Na source. Results, reported in Fig. 3.7, show that ST values from 0.25 to 1 μs provide an equivalent energy resolutions.

Once fixed ST to 1 μs, we studied the dependance of the energy resolution on the high voltage (Fig. 3.8), we noticed that the value of HV = 700 V corresponds clearly to the best performances.

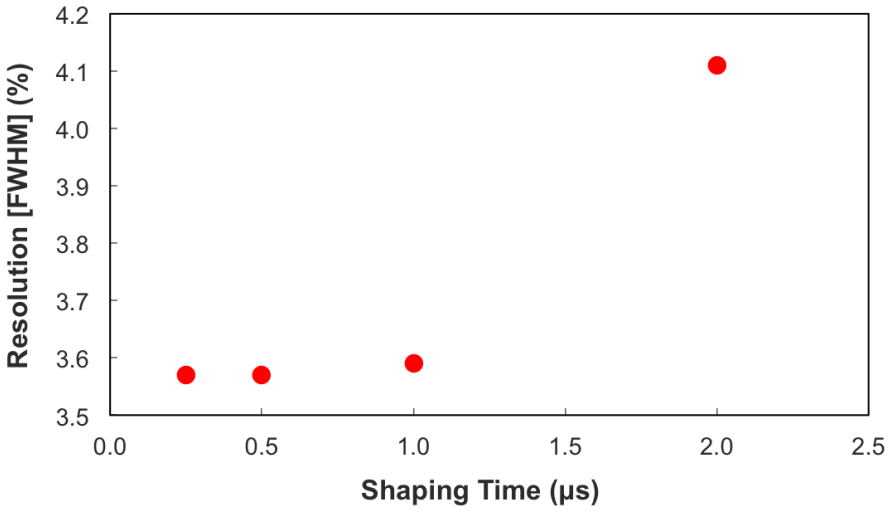

Figure 3.7: Relation between shaping time and resolution in $LaBr_3(Ce)$.

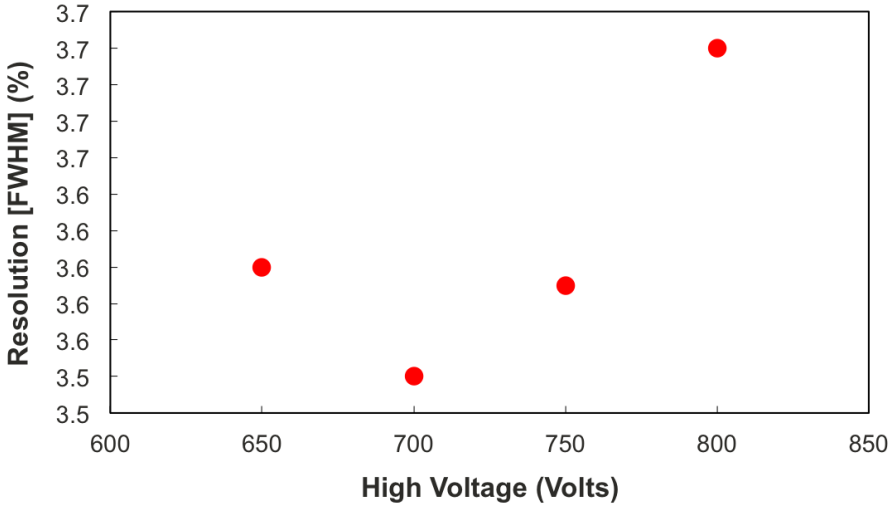

Figure 3.8: Relation between power supply and resolution in $LaBr_3(Ce)$.

3.2.2 Resolution at high energies

High energy tests were performed with a AmBe source, whose spectrum is shown in Fig. 3.9.

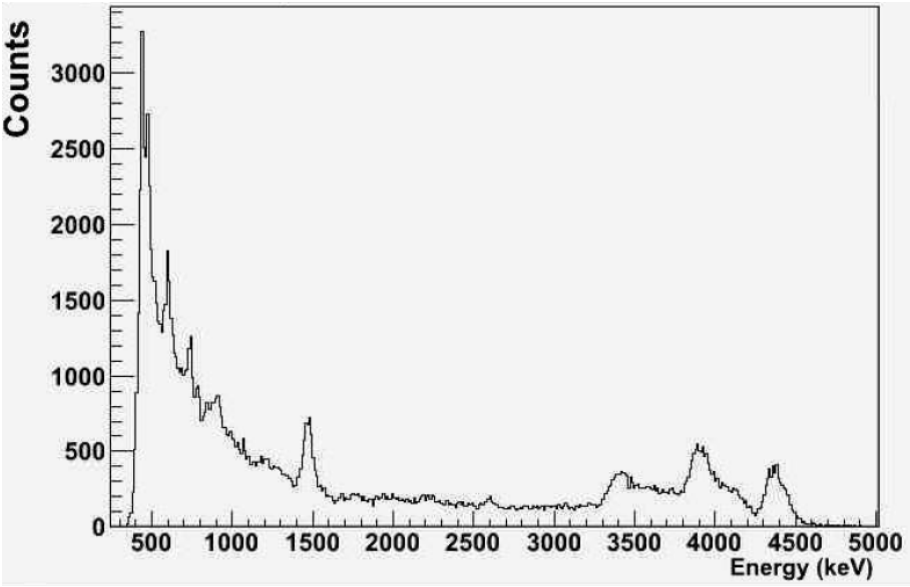

Figure 3.9: AmBe spectrum taken with $LaBr_3(Ce)$

It was not possible to obtain the correct energy for the 4.4 MeV peak through standard linear calibration based on ^{22}Na or ^{60}Co sources. Consequently we performed a non-linear calibration using a second degree polynomial function. Calibrated spectrum shows the sequency of 4.4, 3.9, 3.4 MeV due to first and second escape. It is worth mentioning that Monte Carlo simulations [57] predict a ratio of 5:4:3 between Full Energy, Single Escape and Double Escape, in accordance with our data.

The measured energy resolution at 4.4 MeV is about 3.7%, mainly due to the Doppler Broadening [56].

3.2.3 Time resolution

As in the previous case, we started in searching the best value for the delay of the CFTD. Results are displayed in Fig. 3.10. The time resolution resolution sets around 0.65 ns [FWHM] with minimum thresholds and a 16 ns delay.

Count rate capability

With the same procedure used for NaI(Tl) we analyzed resolution and relative shift (with respect to the lowest measured rate of the two peaks, 511 and 1275 keV of the ^{22}Na source) as a function of the count rate.

There is a quite large shift of about 7.5% at the count rate of 20 kHz, but this

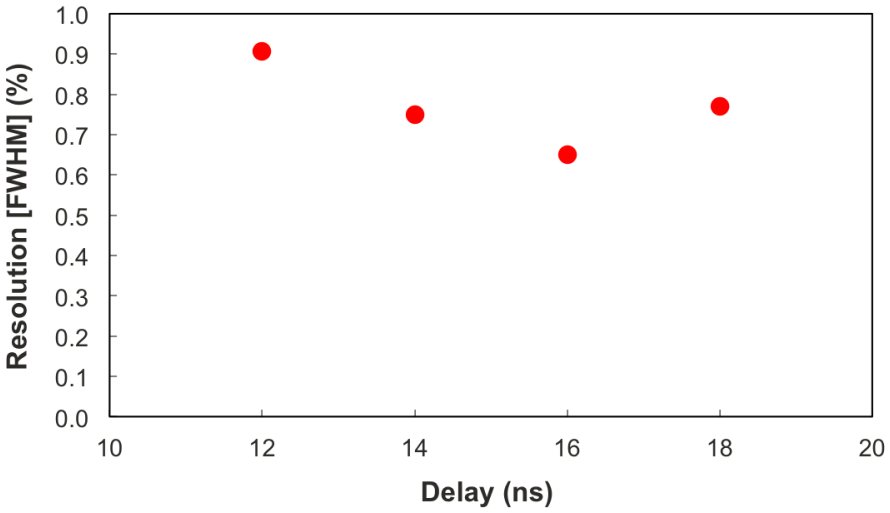

Figure 3.10: Relation between delay and time resolution in $LaBr_3(Ce)$

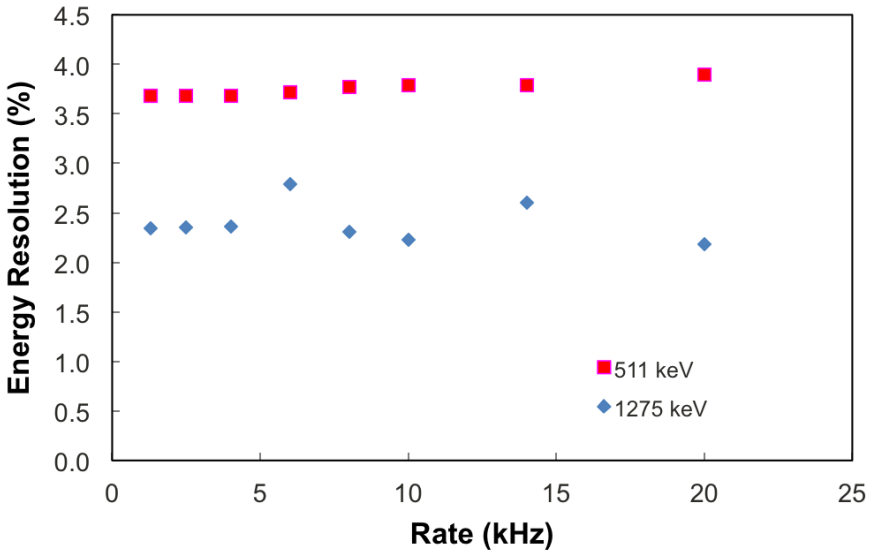

Figure 3.11: Relation between resolution and rate in $LaBr_3(Ce)$

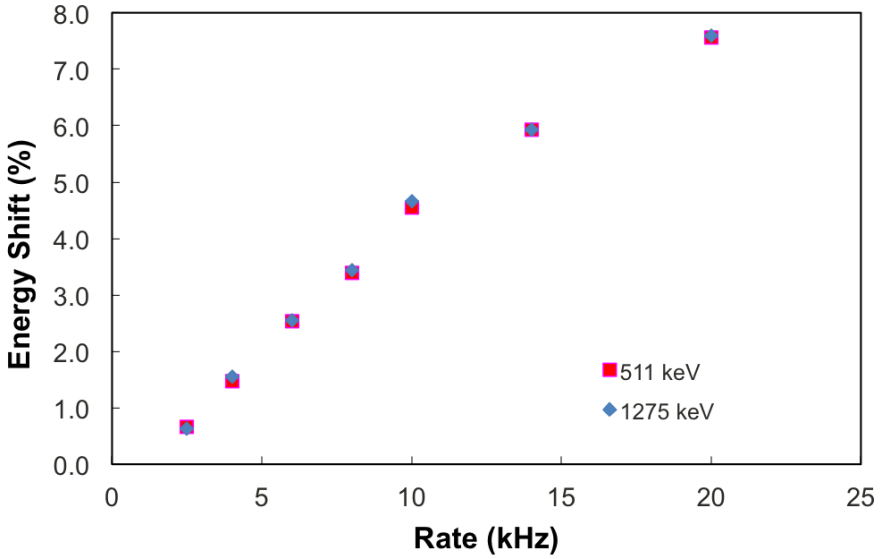

Figure 3.12: Relation between peak shift and rate in $LaBr_3$(Ce)

seems not to affect the energy resolution that is in order with the specification of the detector. This shift is probably due to strong afterglow in the $LaBr_3$(Ce) [58] and will be discussed in details in the next chapter with the new digital electronics.

As a conclusion, the preliminary tests of the $LaBr_3$(Ce) detectors are:

- operating voltage 750 Volt,
- best resolution with ST = 1 μs (or less) integration of anode signal,
- linearity loss at high energies,
- gain is not stable at high counting rates,
- time resolution much lower than 1 ns with a delay of 16 ns for CFTD.

Internal background

In addition we have also studied the self-activity background in the $LaBr_3$(Ce) detector. As already discussed in Section 2.1.1 the background is due to the presence of ^{138}La (1 part over 104) and the contamination with ^{227}Ac, chemically homologous of lanthanium. Natural radioactivity inside the crystals is due to beta, gamma and alpha emissions reported in Fig. 2.6 (see [29] [6] and Tables 3.1, 3.2).

The total self activity is reported to be 0.85 counts/(s/cm^3) that in case of a 2"x 2" crystal corresponds to about 80 Hz. In our 3"x 3"crystal, we measured a background of about 220 Hz with very low threshold.

Background spectra measured in this work is reported in Fig. 3.13. It is evident the contribution of ^{138}La and ^{227}Ac.

Isotope	Decay	$E_{\beta-}$ (keV)	I_e (%)	E_γ (keV)	I_γ (%)
^{138}La	β^-	252 ± 12	34	789	34
	EC		66	1436	66
^{211}Pb	β^-	1378 ± 8	100		
^{207}Tl	β^-	1423 ± 5	100		

Table 3.1: Self-activity in $LaBr_3$(Ce) crystals due to β decay

Isotope	Q (keV)	E_α (keV)	E_γ (keV)	Absolute branch (%)	Relative branch (%)	Measured branch (%)
^{207}Th	6146	5756	256	7.0±0.4	54±3	66±9
	6146	5756	236	12.3±0.9	98±7	118±12
^{223}Ra	5979	5716	144	3.2±0.1	25±1	24±11
			154	5.6±0.1	43±1	37±9
		5607	269	13.7±0.3	106±2	106±10
		5540	324	3.9±0.1	30±1	26±8
			338	2.8±0.1	22±1	27±8
^{219}Rn	6946	6553	271	10.8±0.3	84±2	89±9
	6946	6425	402	6.4±0.2	50±2	47±8
^{211}Bi	6751	6278	351	12.9±0.1	100±1	100

Table 3.2: The comparison between the measured relative branch of α decay with that expected assuming secular equilibrium

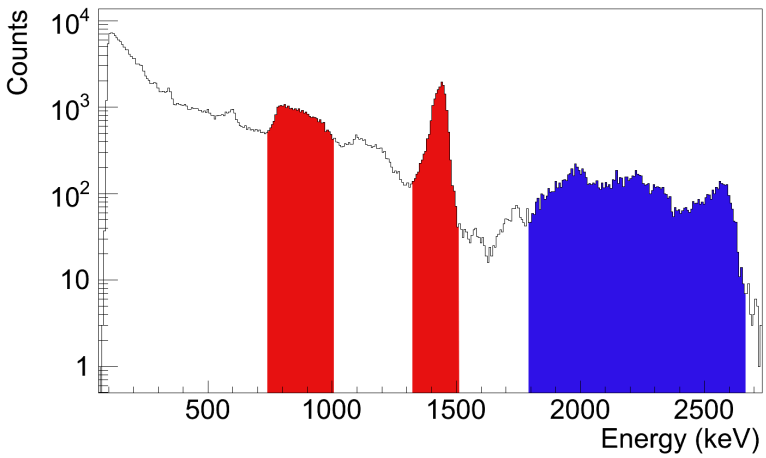

Figure 3.13: Background acquisition with $LaBr_3$(Ce). Red regions are the contribution from ^{138}La, blue region is the contribution of ^{227}Ac.

Response to neutrons

Finally, the $LaBr_3(Ce)$ crystal has been also irradiated with neutrons from a source of ^{252}Cf. Neutron induced events were selected by time-of-flight measures against a fast plastic. The spectrum of the neutron induced events is shown in Fig. 3.14.

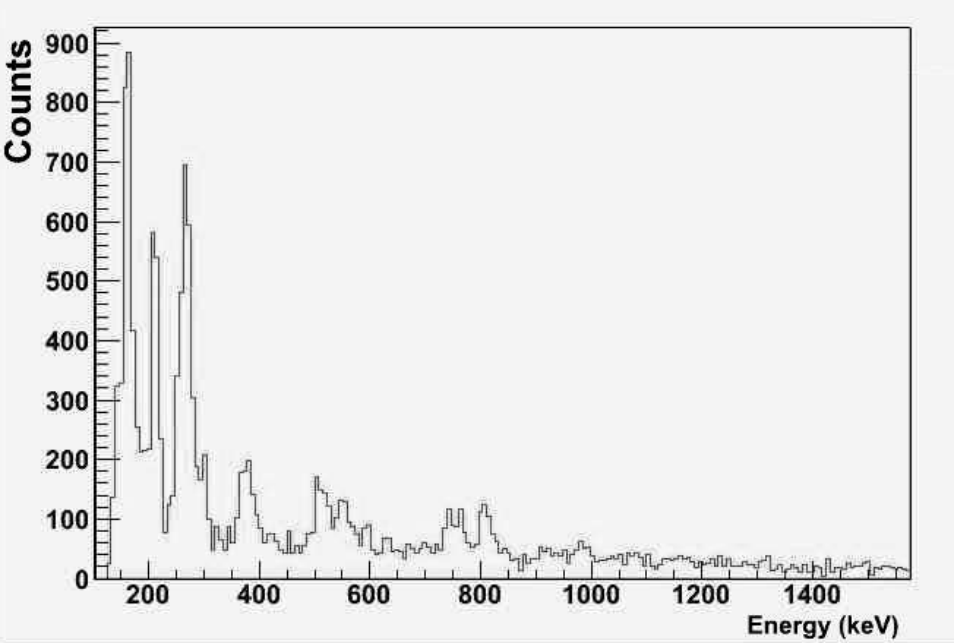

Figure 3.14: Spectrum of neutron induced events in $LaBr_3(Ce)$

Peaks visible in Fig. 3.14 correspond to gamma transitions in the ^{139}La and $^{79,81}Br$ nuclei, induced by inelastic scattering of neutrons. Table 3.3 [59] contains a more detailed explanation of the structure:

Experimental		NNDC database
E_γ (keV)	Nucleus	E_γ (keV)
160	^{139}La	166
210	^{79}Br	207
270	^{81}Br	260
	^{81}Br	275
380		
513		
550	^{81}Br	538
	^{81}Br	566
750		
810	^{81}Br	836

Table 3.3: Neutron induced gamma transitions in $LaBr_3(Ce)$

The results are in good agreement with the data from NNDC database.

3.3 NE-213

The neutron detector NE-213, has a diameter of 5"and 2"thickness, and is characterized by using γ-ray and neutron source to find out best working conditions to discriminate fast neutrons from γ-rays and optimize the energy resolution of the detector.

3.3.1 Calibration with ^{22}Na source

The energy calibration of a liquid or plastic scintillator has been matter of several studies in the past due to the special characteristics of this type of detector ([60]; [61]). In fact the low average atomic number of the plastic material implies that photons emitted by typical radioactive sources interact only by Compton scattering. In this case the nominal energy of the Compton Edge is well known. However, the finite pulse resolution of the scintillation detector implies that the position of the maximum in the Compton events distribution is shifted to lower energies, with the shift depending on the detector pulse resolution. In order to solve this problem, some empirical prescriptions have been developed in the past and simulations by Monte Carlo methods are commonly used to determine the shift value by fitting the experimental distribution. In this work we use a simplified method [62].

Calibration procedure

We construct the expected distribution of the Compton events using the Klein-Nishina formula [63]:

$$\frac{d\sigma}{dT} = \frac{\pi r_e^2}{m_e c^2 \alpha^2} \cdot \left(2 + \frac{s^2}{\alpha^2 (1-s)^2} + \frac{s}{(1-s)}\left(s - \frac{2}{\alpha}\right)\right)$$

where T is the kinetic energy of the scattered electron, r_e is the classical electron radius, $\alpha = h\nu/m_e c^2$, $s = T/h\nu$ and $h\nu$ is the initial photon energy. The overall pulse height resolution of the detector is reproduced by a Gaussian smearing of the predicted distribution [64] [65]. As an example, we compare the effect of the Gaussian smearing corresponding to width values of σ = 5, 10, 15 and 25 keV with the theoretical distribution (see Fig. 3.15). It appears, as expected, that the maximum in the Compton distribution moves to a lower energy value by decreasing the pulse height resolution.

The energy calibration of liquid scintillators is performed by the following steps:

1. measuring a high statistics pulse height distribution using a ^{22}Na gamma ray source,

2. producing a set of theoretical Compton distributions for the 511 keV and 1275 keV gamma rays with Gaussian smearing for different values of the width

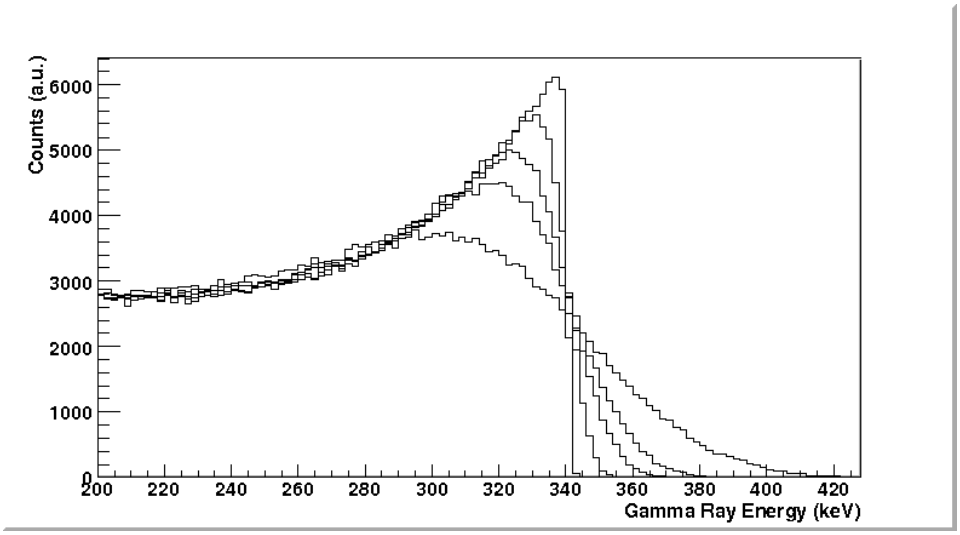

Figure 3.15: The effect of different gaussian smearings over a theoretical Compton Edge

(usually from 10 to 200 keV),

3. determining, by a χ^2 analysis, the width that better reproduces the experimental distribution. The best-fit width value determines directly the energy shift of the nominal Compton Edge, used to calibrate the spectra and the energy resolution of the detector. Furthermore, the variance of the χ_2 distribution provides information about the sensitivity of this method.

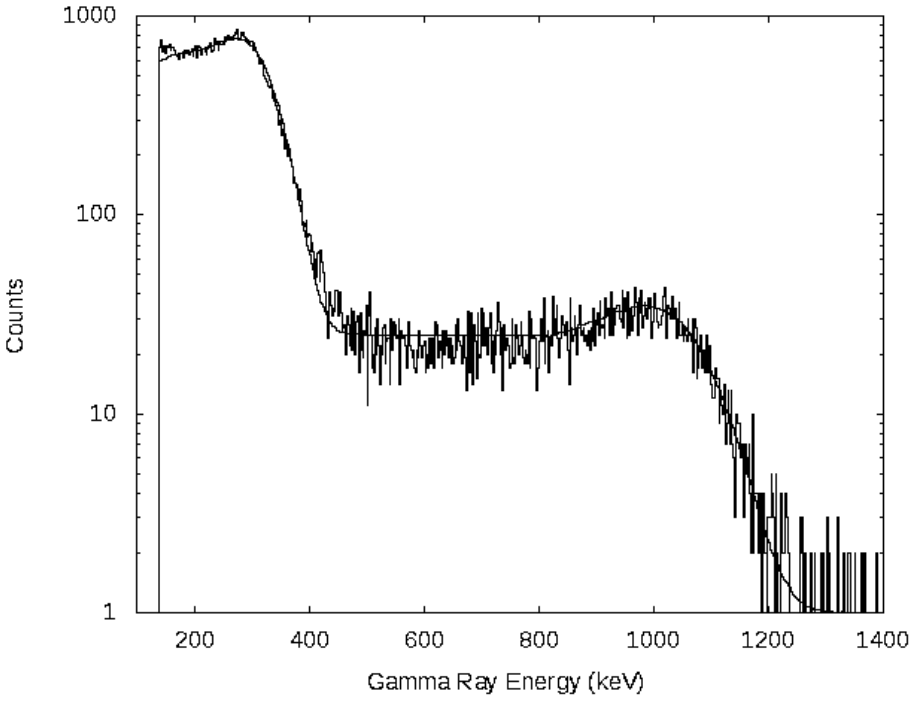

Figure 3.16: Fitting experimental Compton Edge spectrum for liquid scintillator

An example of the above procedure is reported in Fig. 3.16 for the ^{22}Na spec-

trum measured by one of our EJ301 liquid scintillators. The result of the spectrum analysis is also shown. It is found that the best fit values for the width of the Gaussian smearing are $\sigma = 32$ keV ($\sigma = 52$ keV) for the 511 keV (1275 keV) photon, respectively. This resolution values imply shifts of 53 keV and 84 keV for the two maxima in the spectrum respect to the nominal Compton Edge energies. The sensitivity of this method is typically 10% of the σ value. It is worth mentioning that this method was first tested by using high resolution HPGe spectra where the energy calibration was obtained either by using directly the full-energy peaks or by the method previously presented. It is found that, in this case, the two calibrations are very close within the experimental uncertainties. In the same way it was also verified that our results are very close to those of [66]; here the method makes use of a linear fitting of the falling region of the spectrum at energies higher than the Compton Maximum to get an estimate of the detector resolution.

In Fig. 3.17 we show a typical calibrated spectra for the NE-213 SMANDRA detectors. The energy resolution (σ) is, in this case, 40 keV for the the 511 keV photon and 68 keV for the 1275 keV one.

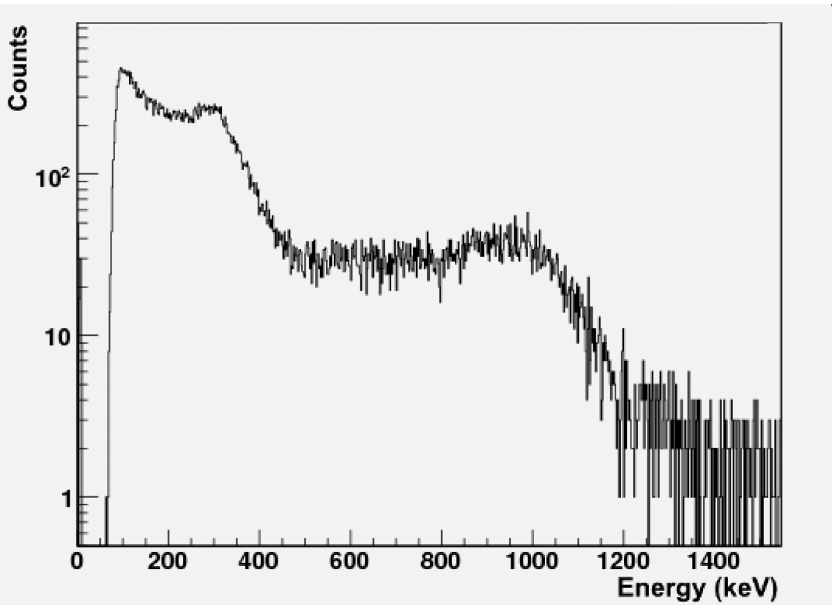

Figure 3.17: Calibration spectrum of NE-213

This type of calibration is used in all the following paragraphs. Such calibration values are espressed in units of keVee (keV electron equivalent) defined as the energy of a photon that produces a given impulse in the scintillator. Note that recoil protons generated by neutrons through elastic scattering on Hydrogen nuclei inside the scintillator produce less light compared to electrons of the same kinetic energy.

3.3.2 Pulse Shape discrimination

It is know that the scintillation light is composed of two components, one faster than the other (see section 2.1.2). The fast component is due to prompt fluorescence and is characterized by a decay time of the order of few ns. The slow component corresponds to the delayed fluorescence and has a typical decay time of the order of 50-100 ns. The ratio between fast and slow components depends on the kind of particle which causes the ionization as show in Fig. 2.9. Taking into account that neutron produces protons when interacting with scintillator while a γ produces electrons, the produced light shows a different distribution as demonstrated in Fig. 3.18 where is clear the different amplitute of the tail of the signal. The analysis of the signal provide the possibility to discriminate between neutrons and γ-ray.

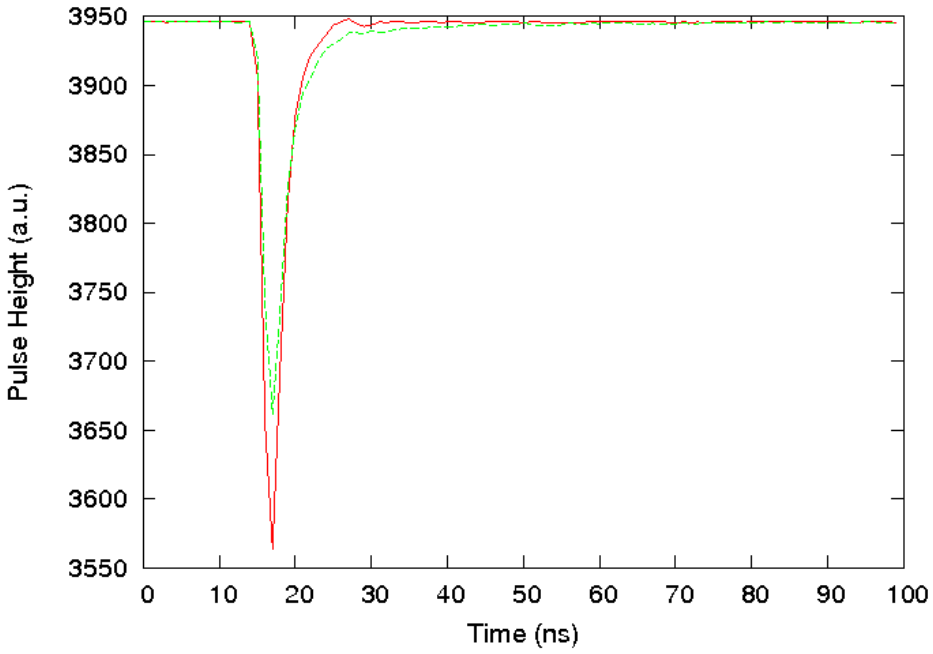

Figure 3.18: Signal for neutron (green) and γ-ray (red) of the same energy. The tail of the signal allows us to discriminate them.

We used the classical method of integrating the total signal and the delayed component by using standard NIM modules. Signal corresponding to delayed component was obtained with a 150 ns gate, delayed by 15 ns from the beginning of the impulse.

In Fig. 3.19 we report a bidimensional graph of the total integral (PH_TOT) versus the delayed component (PH_D). It is noticeable that neutron/gamma discrimination works well for pulse height larger than 200 keVee, corresponding to neutron energies of 0.7 MeV or greater (note that average energy of fission neutrons is about 2 MeV).

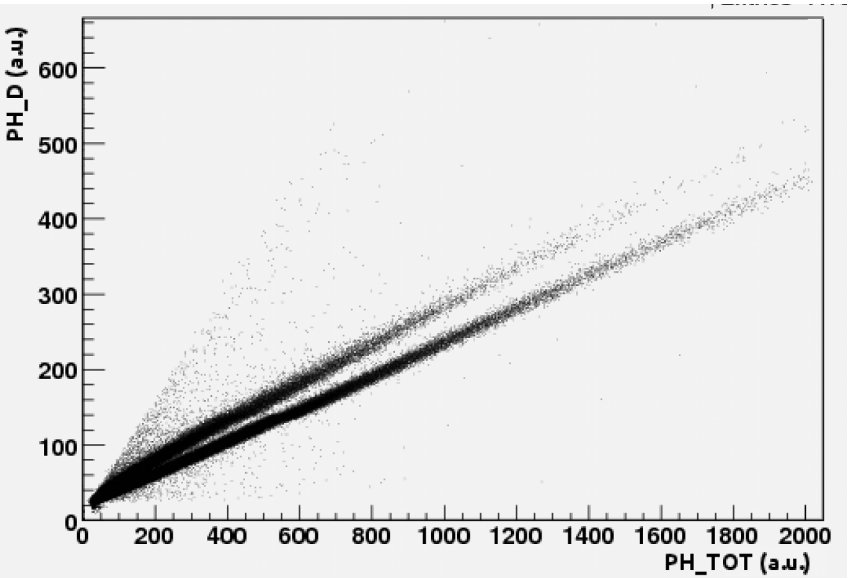

Figure 3.19: Neutron/gamma ray discrimination plot

Chapter 4

Improvement with Digital Electronics

4.1 VME technology

VMEbus is a computer architecture. The term 'VME' stands for VERSA Module Eurocard and was first defined in 1980 by a group of manufacturers. This group was composed of researchers from Motorola, Mostek and Signetics corporations. The suffix "bus" is a generic term describing a computer data path, hence VMEbus represents a standardized extension of VERSA mechanically compatible with the Eurocard board standard that is now an IEC standard as ANSI/IEEE 1014-1987, widely used in various physical and engineering applications. Since its introduction, VMEbus generated thousands of products and attracted hundreds of manufacturers of boards, mechanical hardware, software and bus interface chips. It continues to grow and support different applications such as industrial controls, military systems, telecommunications, office automation and instrumentation systems.

Unlike NIM standard, the use of VME bus allows direct communication between different boards hosted in the same crate: each board is identified by a logical 32 bit address ("base address") defined by a switch on the board itself. The first board of the crate acts as controller of data flow. In each board, a set of readable memory registers contains the data. Another set of writeable registers is available for committing istructions or writing down configuration parameters. The possibility to operate all the boards from the controller is of great advantage because results in various levels of automation of an experiment. In our configuration, the controller board is connected to a PC and driven by a dedicated software interface developed for this project.

4.2 VME prototype crate

We use prototype battery-operated VME mini-crate (4 slots), based on commercial model CAEN VME8004 (see Fig. 4.1). The table 4.1 describes its main features.

Mechanics	19"VME case, 4 slots 6U, 160mm VME boards
Dimensions	19"width, 2U height
Backplane	VME64 J1/J2, 4 slot Automatic daisy chain
Mains Input	Auto range: 90÷264 Vac, 47÷63 Hz
Output power	250 W @ 110÷264 Vac
Maximum Current	25 A @ +5 V 16 A @ +12 V 1 A @ -12 V
Isolation	CE acc. to EN 61010
Noise and ripple	< 60 mVpp @ +5 V < 160 mVpp @ +12 V < 250 mVpp @ -12 V
Operation	0÷50 °C without derating
Cooling Airflow	66 m^3/h

Table 4.1: Properties of CAEN VME8004 minicrate

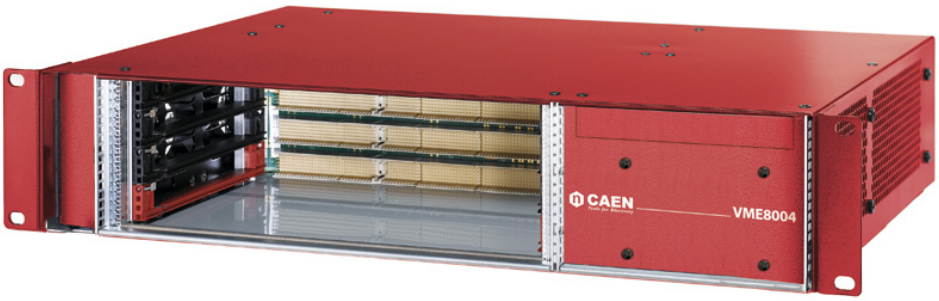

Figure 4.1: CAEN VME8004 minicrate

The controller slot is the lower one. The internal mechanical layout of SMANDRA has been designed specifically to accomodate this crate, providing adequate air-flow for cooling requirements.

4.3 USB bridge

A USB bridge model CAEN V1718 (shown in Fig. 4.2) provides standard connection with the computer, with a maximum transfer rate of 30 MB/s (see Table 4.2 for further details).

This module, placed in the first position on VME-crate, provides electrical interface between computers and the VME and takes care of the conversion from software commands to VMEbus hardware language. Every board corresponds to a library containing its own specific set of high-level instructions (e.g. for rising a voltage or reading a register). The use of V1718 and its standard library allows to avoid

building from scratch a direct interface to the VME bus using a raw programmable board.

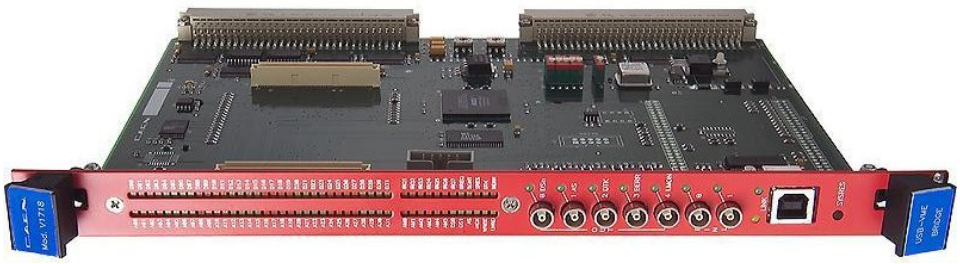

Figure 4.2: CAEN V1718 USB bridge

Packaging	1-unit wide and 6U high VME module
PC Interface	USB 2.0 compliant
Transfer rate	30 Mbyte/s
Panel outputs	5 NIM/TTL, programmable
Panel inputs	2 NIM/TTL, programmable

Table 4.2: Properties of CAEN V1718 USB bridge

4.4 HV power supply

High-Voltage power supply is provided through the programmable board V6533 HV Power Supply for all the detectors (Fig. 4.3). It is housing 6 high voltage power supply channels 4kV, 3mA (9W max), three of them positive and the others negative. The channels share a common floating return, which allows on-detector grounding reducing the noise level. Other relevant properties are summarized in Table 4.3.

VMAX hardware	0÷4 kV common to all board channels
Polarity	Positive or Negative; common floating return
Max. Output Current	3 mA (9W max)
Voltage Set/Monitor Resolution	100 mV
Current Set/Monitor Resolution	50 nA
Output Voltage	0÷4 kV (connector output)
VMAX hardware accuracy	2% of FSR
VMAX software	0÷4 kV selectable for each channel
VMAX software resolution	100 mV
Voltage Ripple	1kV/500A: 3mV Typical / 5mV Maximum
	2kV/1mA: 3mV Typical / 5mV Maximum
	4kV/2mA: 12mV Typical / 20mV Maximum
	3kV/3mA: 10mV Typical / 20mV Maximum
Ramp Up/Down	1÷500 V/s, 1 V/s step

Table 4.3: Properties of CAEN V6533 power supply

It is possibile to power different detectors, or study the response to power of a single detector, simply changing a value in the software configuration file.

Figure 4.3: CAEN V6533 high voltage supply board

The V6533 also integrates a temperature sensor for each channel, providing a simple way to continuously monitor the temperature inside the crate.

4.5 Digitizer

The most important board of SMANDRA electronics is the V1720 digitizer board, together with its advanced programmable FPGA.

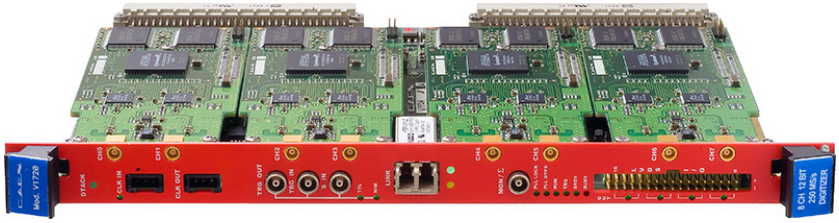

Figure 4.4: CAEN V1720 digitizer

The board is a simple 8-channel, 12bit, 250 MS/s digitizer (main features in Table 4.4), but the built-in programmable FPGA makes the difference with the other types of digitizer. Inside the FPGA can be implemented different firmwares dedicated to specific advanced functions. In SMANDRA we implemented Digital Pulse Processing (DPP) algorithms, providing the following online services for each event:

- time stamp - a reference time of the event from the beginnig of the acquisition,
- both complete and partial integration of the signal - used for Pulse Shape Discrimination (PSD) in the liquid scintillator
- the possibility of storing a selected part of the digitized signal for off-line analysis - e.g. to performing digital CFTD for coincidences recostruction.

The sampling of the signal with V1720 is customizable in many ways, from the trigger mode (by threshold or by peak identification) to the number of samples to save in the records, and each channel has an independent configuration registry.

Analog Input	8 channels, single-ended (SE) or differential. Input range: 2 Vpp; Bandwidth: 125 MHz.
Digital Conversion	Resolution: 12 bit. Sampling rate: 31,25 to 250 MS/s simultaneously on each channel
Memory Buffer	1.25 M sample/ch or 10 M sample/ch; Multi Event Buffer with independent read and write access. Divisible into 1 ÷ 1024 buffers.
Trigger	Individual channel autotrigger
Trigger Time Stamp	32bit - 8ns (34s range). Sync input for Time Stamp alignment
VME interface	VME64X compliant; Multi Cast Cycles Transfer rate: 60MB/s (MBLT64), 100MB/s (2eVME), 160MB/s (2eSST). Sequential and random access to the data.
Input connectors	Single ended: MCX Differential: Tyco MODU II

Table 4.4: Properties of CAEN V1720 digitizer

4.5.1 Principle of operation

The basic operating mode of a digitizer is essentially the same as a digital oscilloscope: the analog signal, after an input stage of signal conditioning mainly used to adapt the dynamic range, is sampled by a flash ADC and stored in a circular memory buffer of a programmable size. At the arrival of the trigger, the buffer is frozen and made available for the readout while the acquisition continues in a new buffer. There are few important differences with digital oscilloscope and classical analog eletronic. The digitizers allow for deadtimeless acquisition. They have the ability to accept two consecutive triggers very close to each other thanks to the multi-buffer memory management: there is no dead time between an acquisition window and the next one. This characteristic is a very important distinctive feature respect to the dead time of analog electronic chains. Furthemore all the channels are allowed to generate triggers independently. The individual trigger can be used locally by the channel that generated it or can be use to generate a global trigger for all the channels in the board. It is possible to synchronize several boards with a common clock reference to make an acquisition system with a theoretically unlimited number of channels aligned in time to have, for example, events with correlated time stamps. Another distinctive fact is the high bandwidth readout that starts from 30MB/s with the USB connection to reach 160MB/s with optical link technology. Finally with the FPGA (Field Programmable Gate Array) it is possible to perform on line data processing. FPGAs are programmable devices with the ability to manage the ADC sample stream and implement online digital algorithms for signal processing. This feature is very important for the implementation of systems that are not simply based on the acquisition, storage and readout of waveforms (raw data) but rather on the calculation of certain quantities of interest (e.g. the charge associated with a

pulse, the pulse height, the leading edge, the baseline, the arrival time and other parameters) and the storage and transfer of just the final results, with clear advantages in terms of readout bandwidth. In Fig. 4.5 is shown an example of the possibile implementation of the FPGA. It represents a diagram of the operation during a charge integration of the signal.

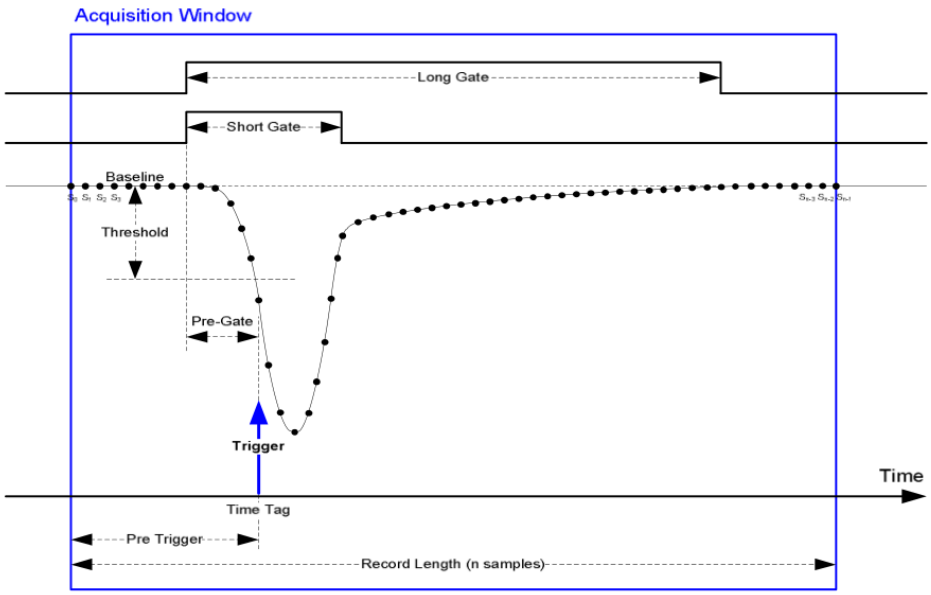

Figure 4.5: Signal sampling with explanation of different acquisition parameters.

As discussed before, the board digitizes input signals in a continous way and the samples are stored in a buffer. When the trigger condition is satisfied, the analysis algorithm goes back along the sample array, according to the PRE-TRIGGER setting and opens the acquisition windows. PRE-GATE parameters define the starting point of the integration that ends according to the LONG and SHORT GATE value. The resulting values are stored in the DATA buffer, together with the desired number of raw samples and a time tag of the event. This operation is done independently for each enabled channel, with a common clock every 4 ns. To optimize the FPGA performances several of this parameters need to be tuned. This optimization was performed empirically, by scanning for each parameter a range of possible values and measuring for each setting the energy resolution of the detector. For $LaBr_3$(Ce) and NaI(Tl) detector we used full energy peak from ^{22}Na to calculate the detector resolution. For the liquid scintillator we used the procedure described in Section 3.3.1 was used.

4.6 Optimization of FPGA parameters

The 12bit FlashADC uses 4096 channels for digitizing signals, and the default baseline is set at half of the range, that corresponds to 2100 channel. Considering that we use only negative pulses, we set the DC offset value to -36 units for all channels; in this way the baseline raises to channel 4000 and the available dynamical range of the FADC is doubled.

After that, we carried out a specific study on each detector to define the best operating values for all the other parameters with particular attention to LONG-GATE, PRE-GATE and BSLTHRESHOLD. The SHORT-GATE parameter is relevant only in the case of liquid scintillator NE-213 for neutron/gamma ray discrimination. The optimization is done recursively, every optimized parameter is used to optimize the next parameter. When the processing is done, we restart from the first parameter until the best value doesn't change. The data reported in the next section regard the last optimization process.

4.6.1 NaI(Tl) gamma detector

The signal of NaI(Tl) detector takes of about 750 ns long, with a raising time of about 100 ns. The 250 M/s FADC has an internal clock of 4 ns, that is the time width of each bin, so the integration gate must be greater than 200 intervals (800 ns).

We performed an initial "coarse" optimization of the LONG-GATE, locating the minimum resolution in a working range between 200 and 250 units. Then we did a fine search, varying the LONG-GATE value from 170 to 260 with steps of 10 units.

Results reported in Fig. 4.6 show the measured energy resolution for the two peaks of a ^{22}Na source as a function of LongGate duration (in 4 ns units). We can

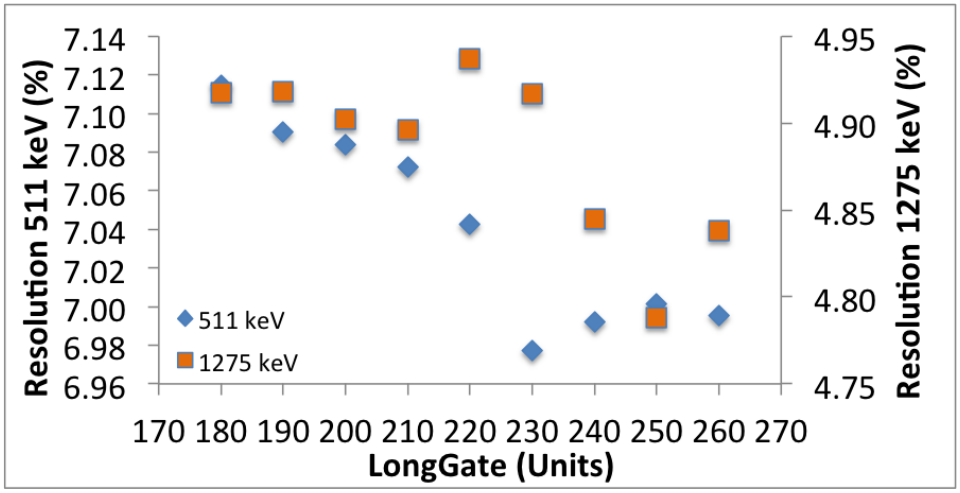

Figure 4.6: NaI(Tl) scintillator: LongGate optimization

notice that the value of 260 (corresponding to 1040 ns) gives best resolution at both energies.

Then, we search for the best value of the PRE-GATE parameter using the same procedure; PRE-GATE starts from the time where signal overcomes threshold, and has been set from a value of 15 to 50 (between 60 and 200 ns). The results are shown in Fig. 4.7.

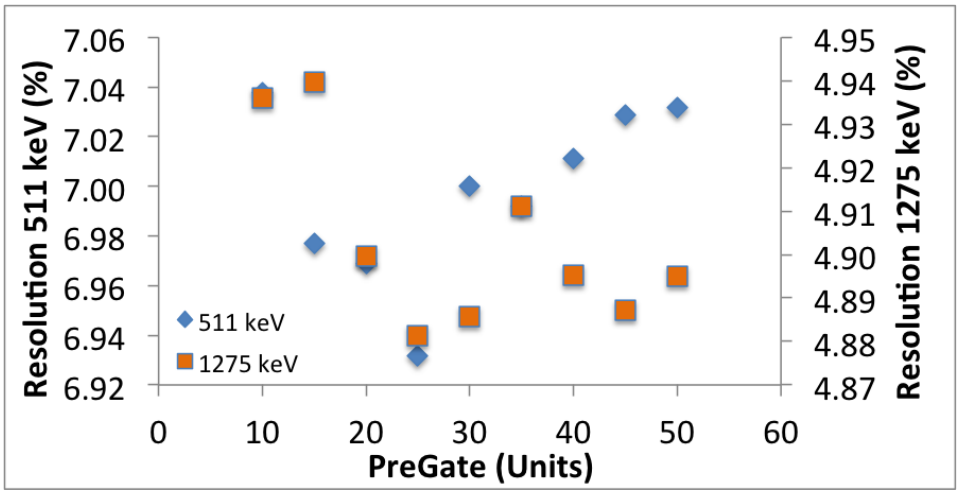

Figure 4.7: NaI(Tl) scintillator: PreGate optimization

Even the data present show some fluctuation, we fix the best value for PRE-GATE to 25 units, equivalent to 100 ns.

Last parameter to be analyzed is BSLThreshold that specify the threshold value under which the FPGA can sample the baseline value of the signal. Best value is found to be 3.

Energy resolution values measured after the optimization are summarized in Table 4.5 and compared to previous measurements carried on the same detector but with NIM amplifier and ADC.

NaI(Tl)	Standard NIM	FADC V1720
Energy Resolution @ 511 keV	7.51%	7,01%
Energy Resolution @ 1275 keV	4.87%	4.62%

Table 4.5: Resolution for NaI(Tl) scintillator

A significant improvement of the measured energy resolution using FADC V1720 is obtained at the lower energy.

4.6.2 $LaBr_3$(Ce) gamma detector

The signal of $LaBr_3$(Ce) detector is about 100 ns long with a raising time of 20 ns.

LongGate parameter has been varied from 25 to 60 units (corresponding to 100

to 240 ns) with a step of 5 units; results with the same ^{22}Na source are shown in Fig. 4.8.

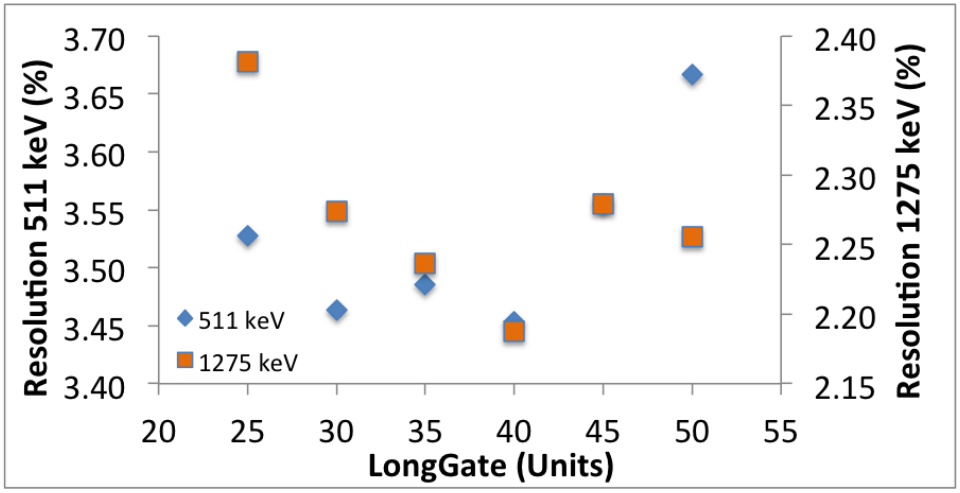

Figure 4.8: $LaBr_3$(Ce) scintillator: LongGate optimization

The best value for LONG-GATE in case of $LaBr_3$(Ce) detector is 40 units (160 ns).

PRE-GATE has been optimized in the range from 15 to 50 units (60 to 200 ns); results are shown in Fig. 4.9.

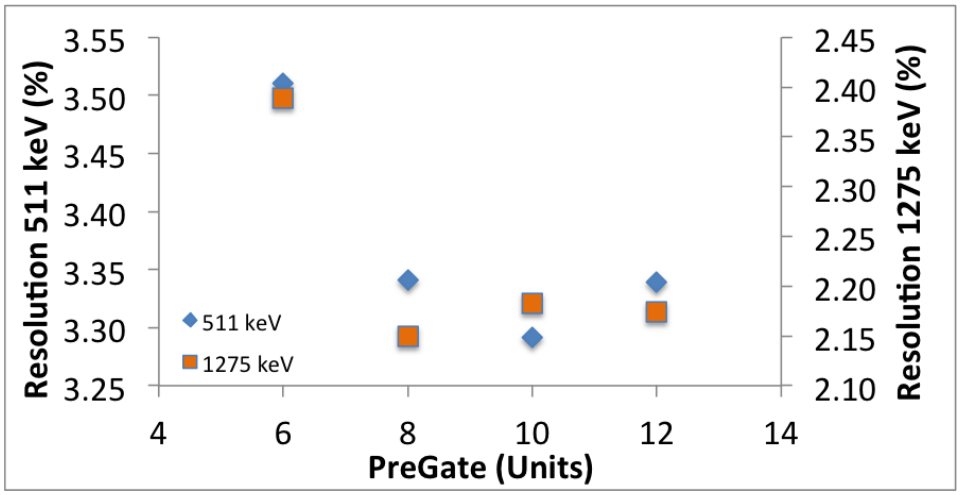

Figure 4.9: $LaBr_3$(Ce) scintillator: PRE-GATE optimization

In Fig. 4.10 we report the resolutions for three values of BLSThreshold. Best performances are obtained with the value 5.

As in case of the NaI(Tl) detector, the measured energy resolutions of $LaBr_3$(Ce) scintillator with FADC V1720 are compared with the NIM measured values (see Table 4.6).

With FADC V1720 the energy resolution values improve significantly. At the energy of 511 keV the performances of VME digitizer improve of about 10% respect

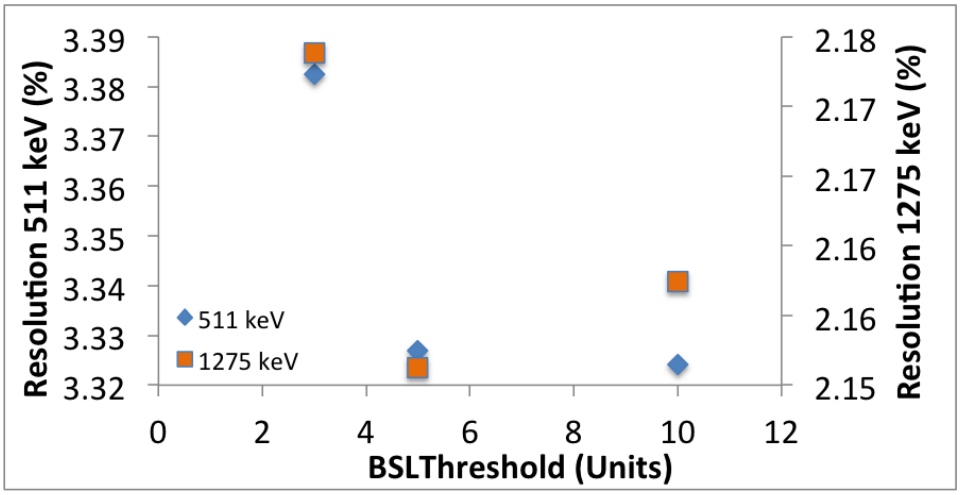

Figure 4.10: $LaBr_3$(Ce) scintillator: BSLThreshold optimization

$LaBr_3$(Ce)	Standard NIM	FADC V1720
Energy Resolution @ 511 keV	3.70%	3.32%
Energy Resolution @ 1275 keV	2.25%	2.16%

Table 4.6: Resolution for $LaBr_3$(Ce) scintillator

to the values obtained with NIM electronics. For this detector Saint-Gobain guarantees resolution better than 3.5% on ^{137}Cs peak at 662 keV. With the same source we measured a resolution of 3.12%, 11% better than nominal value.

4.6.3 NE-213 fast neutron detector

This detector is used as neutron detector. Consequently, the neutron/gamma ray discrimination is crucial. As a consequence, FPGA parameters have been optimized to maximize the discrimination capability.

To evaluate the "quality" of the discrimination it is necessary to define some parameters. First of all, we filled a 2-D scatter plot where events are defined by total charge Q_{Long} and by the charge in the signal tail ($Q_{long} - Q_{short}$) normalized to Q_{long}. The tail-to-full ratio $(Q_{long} - Q_{short})/Q_{long}$ is typicall used for neutron/gamma discrimination.

Results shown in Fig. 4.12 were obtained with a ^{252}Cf source. We then defined a threshold on total charge of 400 keVee (keV electron equivalent: as it was produced by gamma radiation) corresponding to a 1.7 MeV neutron cut. Threshold channel in Fig. 4.11 is at channel 2000.

The 1-dimensional plot shown in Fig. 4.12 is obtained projecting the 2-D scatter plot, from channels 2000 (1.7 MeV) to 16000 (7.4 MeV), on the Y axis. Here the peak due to gamma signals, to the left, for which $(Q_{long} - Q_{short})/Q_{long} < 0.1$, is clearly separated from that of the neutrons, $(Q_{long} - Q_{short})/Q_{long} > 0.1$. At this

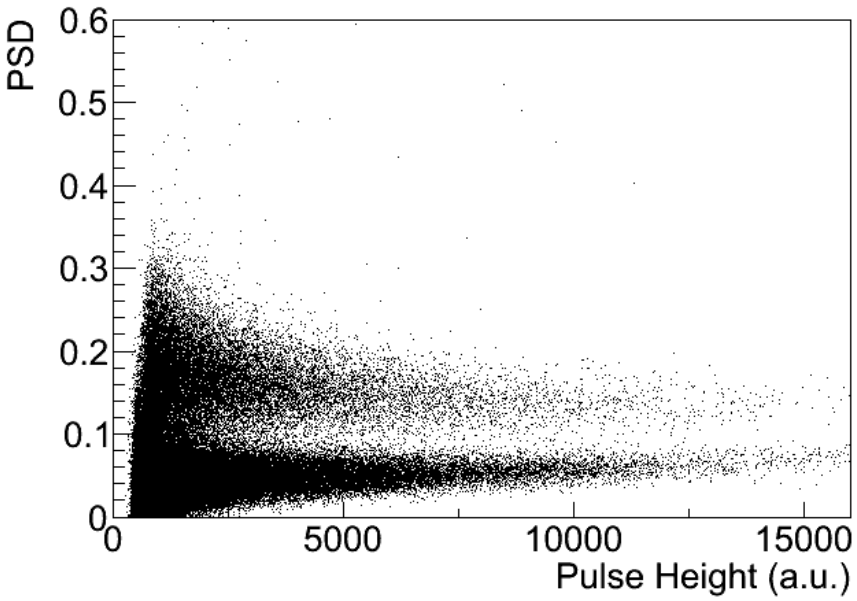

Figure 4.11: NE-213 scintillator: optimization of the neutron/gamma discrimination

point we can define the Figure Of Merit (FOM) as follow:

$$FOM = \frac{FWHM_N + FWHM_G}{PEAK_N - PEAK_G}$$

where PEAK_N e PEAK_G are the centroids of the peaks and FWHM_N, FWHM_G have the usual meaning, N and G indexes being related to neutrons and gammas, respectively.

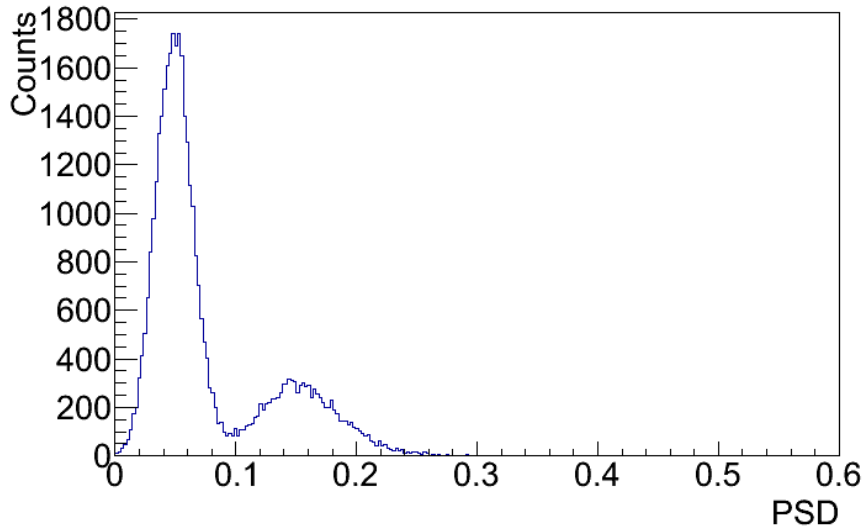

Figure 4.12: Figure of Merit (FOM)

Obviously, a better separation between the two peaks corresponds to a better

neutron/gamma discrimination and a higher FOM.

In the case of the liquid scintillator we have two gates to optimize: the LONG-GATE and the SHORT-GATE. After some quick tests we set the SHORT-GATE at the temporary value of 15, and optimize the LONG-GATE monitoring the FOM. Data are reported in Fig. 4.13.

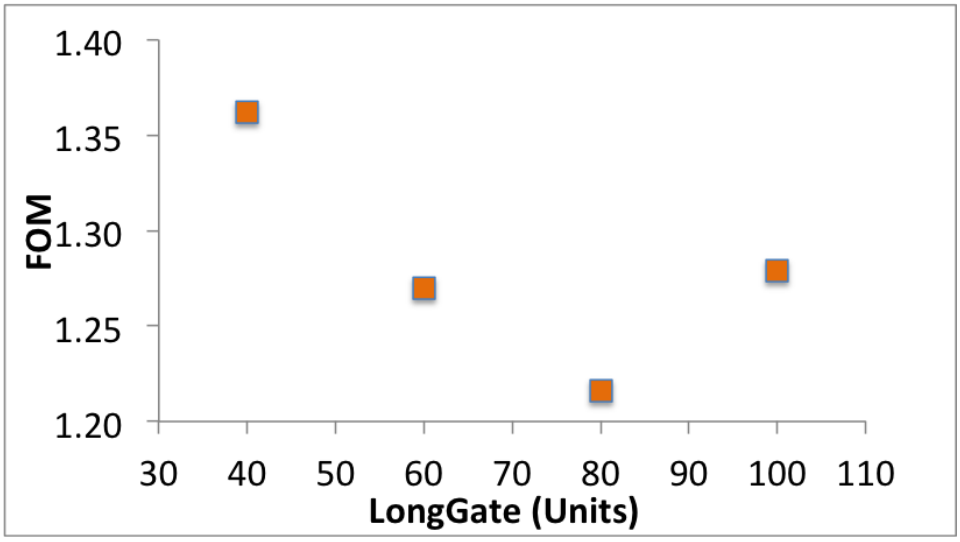

Figure 4.13: NE-213 scintillator: LongGate optimization. FOM is defined in the text.

Better discrimination performances correspond to the LONG-GATE value of 80 units (320 ns). Fixed the LONG-GATE the optimization procedure is applied to SHORT-GATE. The results are lined out in Fig. 4.14. Best separation is related to a value of 12 units (48 ns).

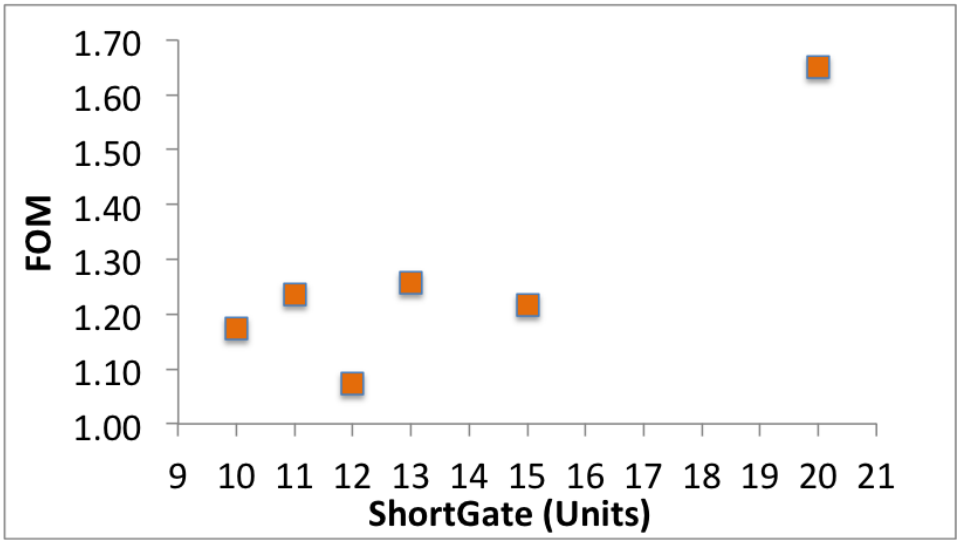

Figure 4.14: NE-213 scintillator: ShortGate optimization. FOM is defined in the text.

Also in case of the NE-213 detector we can compare the on-line FPGA data with off-line results performed analyzing raw events recorded from the FADC or directly

processing the signals with NIM hardware. Table 4.7 compares the values for an energy window of 400 - 1400 keVee.

NE-213	On-line FADC analysis	Off-line analysis of FADC data	Hardware analysis with NIM electronics
FOM	1.08	1.05	0.9

Table 4.7: NE-213 scintillator: FOM obtained with a window of 400-1400 keV

On-line discrimination with the FPGA has nearly the same performances of an off-line analysis of digitized pulses, but allows higher acquisition rates. NIM performances are slightly worse. It is worth mentioning that a much better FOM is obtained by using modern scintillator assembly respect to the results reported in this section.

4.7 Performance at high counting rates

4.7.1 $LaBr_3$(Ce)

The energy resolution of the $LaBr_3$(Ce) scintillator was first tested as a function of the counting rate up to about 20 kHz by using standard NIM electronics (ORTEC Amplifier mod.570) and a ^{22}Na source. The measured energy resolution (δE/E), computed as FWHM/E is rather constant with the rate by using Shaping Time value ST= 0.5μs or ST= 1.0μs. Typical values are δE/E= 3.7% at 551 keV and δE/E= 2.25% at 1275 keV, in agreement with the producer specification (in our case energy resolution lower than 3.5% at 662 keV). Our measured energy resolutions are comparable with those reported in [7, 27] for 2"x 2" and 3"x 3" crystals with standard NIM electronics read-out. Other measurements were performed using the V1720 digitizer with the optimized DPP parameters. The counting rate varied up to several kHz by changing the source position and, for rate over 50 kHz, by stacking on the front face of the scintillator a combination of several different sources. A sample of the obtained spectra is reported in Fig. 4.15.

In Fig. 4.16 we present a summary of the energy resolution measured as a function of counting rate. The energy resolution is generally better than that measured using standard NIM electronics and is generally lower than the value declared by Saint-Gobain up to very high rates (i.e. 340 kHz).

To understand the worsening of the energy resolution above 100 kHz, a specific test of the V1720 card was performed by using a BNC Pulse Generator mod. PB-4 and a Timing Filter Amplifier ORTEC. This was made to obtain a pulse with a shape similar to the $LaBr_3$(Ce) one. Results from the pulser test, reported in Fig. 4.17, demonstrate that the electronics contribution to the energy resolution belongs

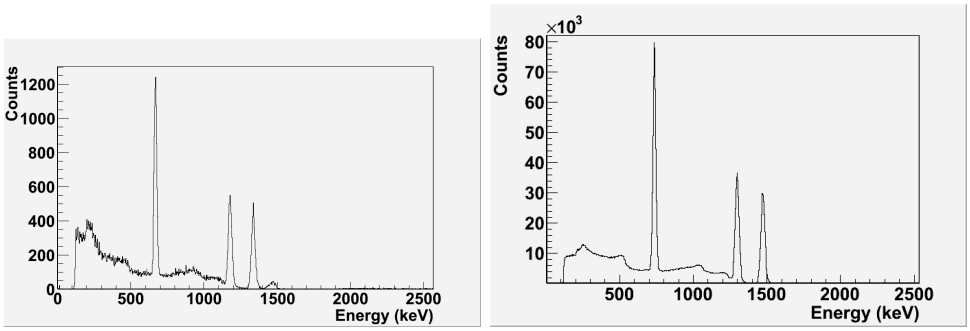

Figure 4.15: Gamma ray spectra measured with the $LaBr_3(Ce)$ scintillator with a ^{137}Cs and a ^{60}Co source at total rate of 1.5 kHz (left panel) and 145 kHz (right panel). The energy calibration was established at the lower rate.

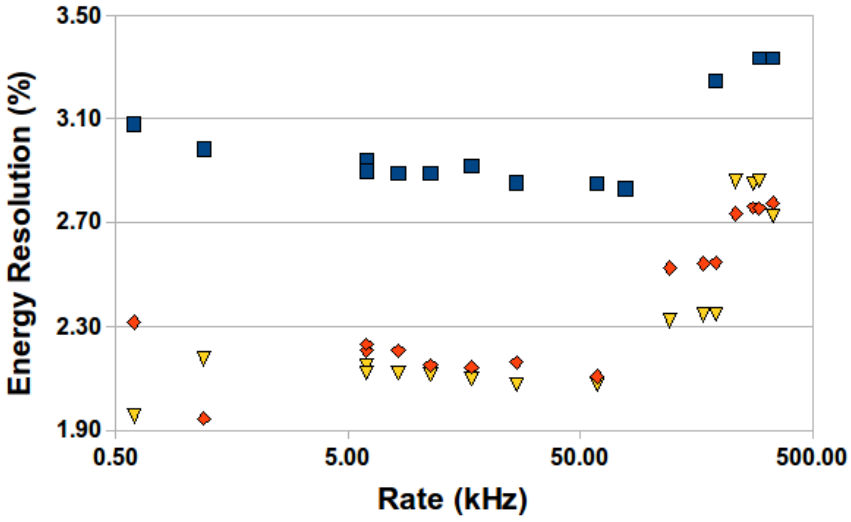

Figure 4.16: Energy resolution of the $LaBr_3(Ce)$ scintillator with the V1720 read-out as a function of the count rate. Squares are relative to the ^{137}Cs gamma line (0.662 MeV) whereas triangles and diamonds are related to the ^{60}Co lines (1.33 and 1.17 MeV)

to the range δE/E= $0.50 \pm 0.05\%$ up to about 180 kHz and then increases up to about 0.6% at 220 kHz. Such contribution to the overall energy resolution reported in Fig. 4.16 is certainly negligible and its variation with the rate does not explain the registered worsening of the energy resolution.

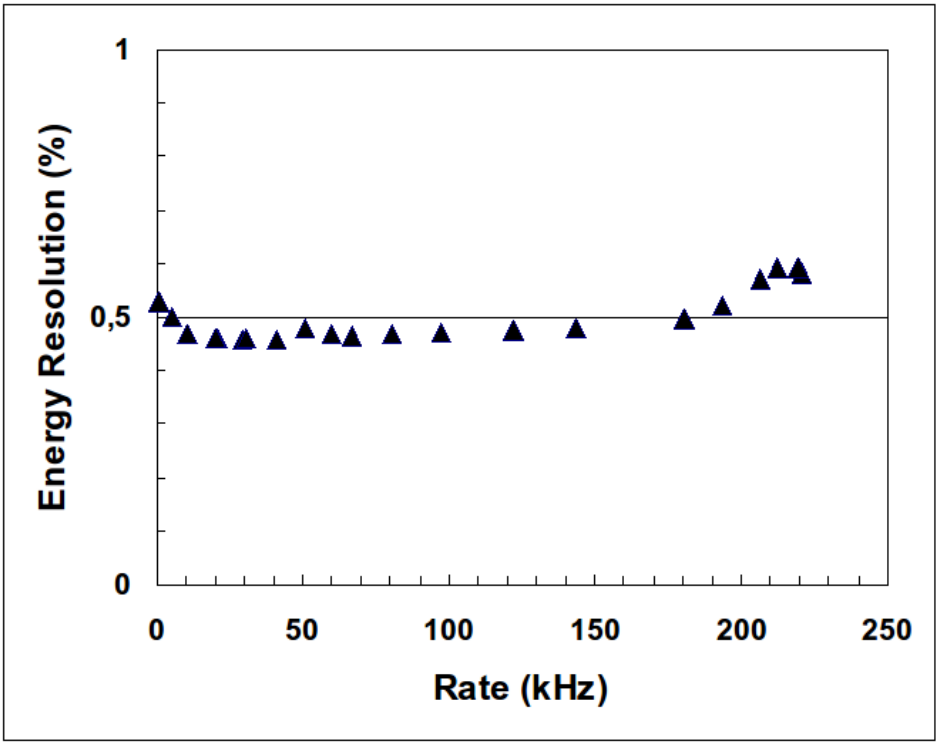

Figure 4.17: Energy resolution of the V1720 card as a function of the rate measured during the pulser tests.

It is worth mentioning that very high count rate applications of $LaBr_3$(Ce) scintillators have been recently reported in the fields of safeguards [67] and plasma diagnostics [68], although a direct comparison of our measured energy resolution rate at high rate it is not possible. It is interesting to note that in [68] the reported energy resolution is lower than 2.4% at 662 keV for a 1.5"x 1.5" crystal up to 40 kHz.

Looking in more detail at Fig. 4.15, it appears that the peaks are apparently shifted at higher energy when the detector load is increased. This effect appears as well in measurements with standard NIM electronics (7% shift at 20 kHz with respect to the peak position measured at 1 kHz.) and does not depend on the gamma ray energy. The shift is magnified at higher rates in the measurements performed with the V1720 digitizer as illustrated in Fig. 4.18, with a measured shift value of about 16% at 250 kHz.

This effect was studied in detail performing the following operations:

- changing the HV power supply and the current limits in biasing the detector,

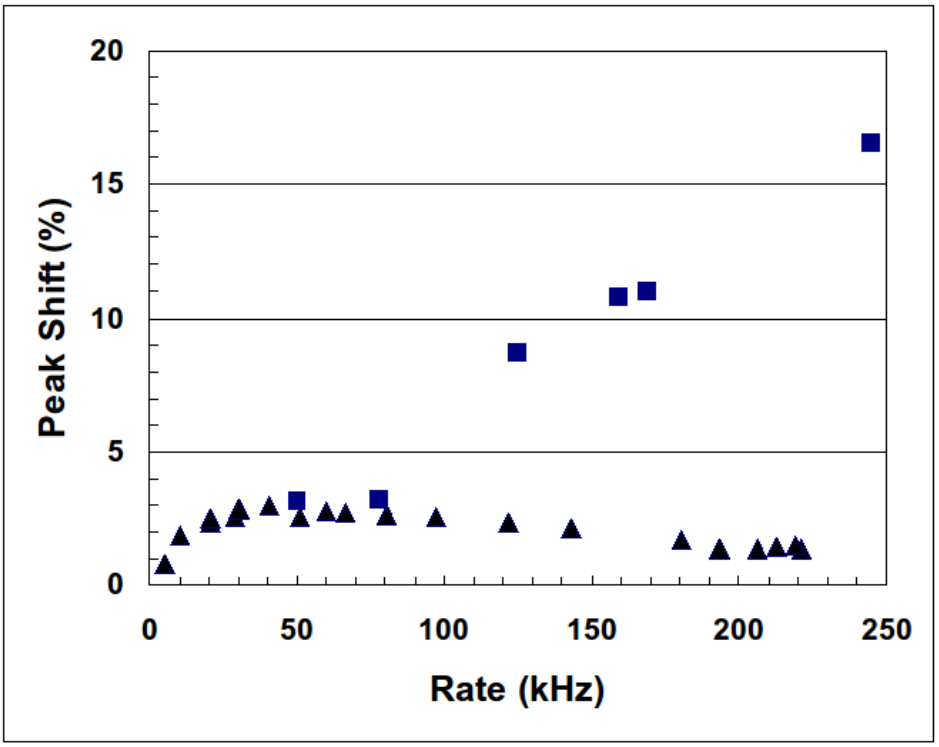

Figure 4.18: Measured shift in the peak position as a function of the detector rate as measured with the V1720 digitizer. Squares are relative to the ^{137}Cs gamma ray (0.662 MeV) whereas triangles are related to the shift measured with pulser.

- replacing the PMT voltage divider with other components available in our Lab (e.g. home made voltage divider, ORTEC or SILENA devices),
- pulser test.

We varied the high voltage of several hundred of volts with a consequent variation of the detector gain, but the relative shift of the peaks remains the same. Also the variation of current limits do not leads to an explanation of the effect. With some voltage divider (as the SILENA), the rate increase causes a shift down of the peak position with a loss of energy resolution. In all the other cases the shift is confimed. Also in this case one can learn something from the pulser run: the variation of the pulser peak position up to 220 kHz is generally lower than 3% compared to the 1 kHz value. In Fig. 4.18 we can notice that the shift measured with the pulser is very close to the gamma source values up to 80 kHz and remains constant up to over 200 kHz, whereas the shift of the gamma ray peak position increases remarkably for rates higher than about 80 kHz.

It is quite interesting to notice that the shift in the peak position for rates higher than 80 kHz is clearly associated with the degradation of the energy resolution from about δE/E = 2.9% [FWHM] at 80 kHz to δE/E = 3.2% [FWHM] at 220 kHz for the 662 keV ^{137}Cs gamma ray. It is know that the $LaBr_3$(Ce) crystal exhibits

a significant afterglow component that might affect the signal-to-noise ratio [69]. Recently, Moszyski [70] reported indeed an interesting correlation of the intrinsic energy resolution of scintillation crystals with their afterglow. Thus the shift effect evidenced in fig.4.18 can be qualitatively explained by the afterglow emission in the crystal.

The measured gamma ray spectrum at the detector load of 340 kHz is presented in Fig. 4.19. Because of the rate-dependent shift, the energy calibration was obtained by using the ^{241}Am (59 keV), ^{22}Na (511 and 1275 keV), ^{137}Cs (662 keV) and ^{60}Co (1.17 and 1.33 MeV) transitions. It appears that the sum peak of the ^{60}Co source (2.5 MeV) and the 4.4 MeV line from AmBe show up at lower energies than expected, revealing a non-linearity of the system for the higher pulse heights. Such effect has been evidenced in [7][27] and were explained as conseguence of the saturations of the PMT. In particular, hardware solutions to this problem have been tested in [27]. As for our detector, the non-linearity has been compensated by using an additional quadratic term into the energy calibration. This procedure is necessary in active interrogations when photons in the range 2-7 MeV are of primary interest.

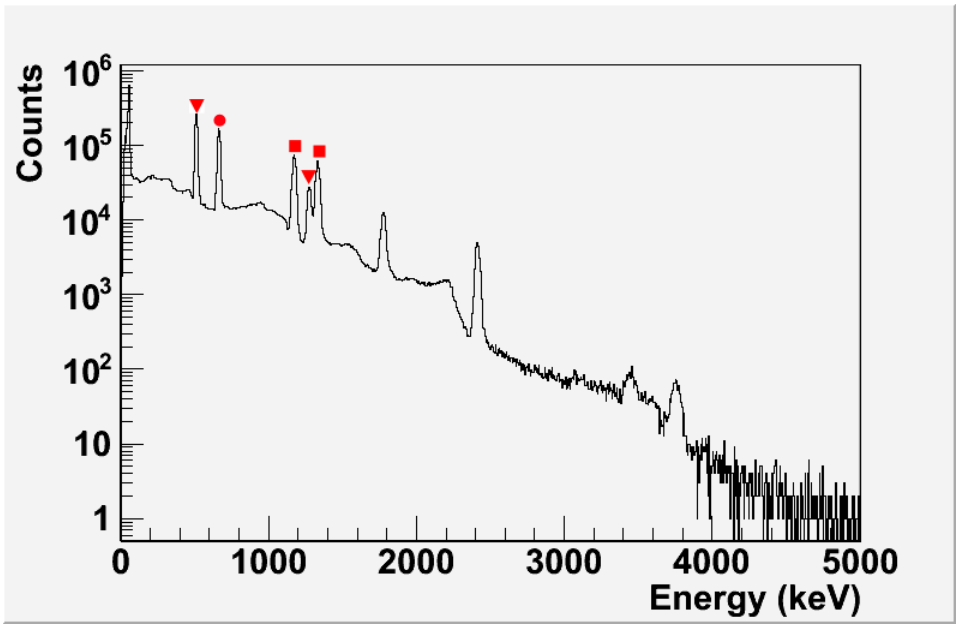

Figure 4.19: Gamma ray spectrum taken with a cocktail source at the total rate of 340 kHz. Triangles mark the ^{22}Na (511 and 1275 keV) transitions, the full dot marks the ^{137}Cs transition (662 keV) and the squares mark the ^{60}Co (1.17 and 1.33 MeV) transitions.

4.7.2 NE-213 liquid scintillator

We performed some test at high counting rate with a AmBe source placed at different distances from the liquid scintillator detector. For each run, the FOM value has been calculated for a window from channel 2000 (1.7 MeV) and channel 16000 (7.4 MeV). Fig. 4.20 shows a typical 2D scatter plot and FOM plot with AmBe source placed

at 11 centimiters with an acquisition rate of 5.3 kHz.

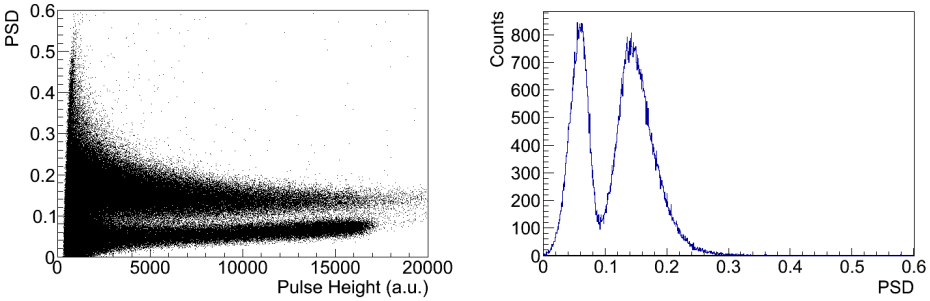

Figure 4.20: On the left panel, NE-213 scatter plot from an AmBe. On the right panel a unidimensional projection of the PSD value with a pulse gate from channel 2000 (1.7 MeV) and channel 16000 (7.4 MeV)

Using an AmBe source we get a better FOM respect to the on obtained with ^{252}Cf; this is due to different energies involved in the decays, as well as a better neutron-to-gamma emission ratio.

The FOM values as a function of the rate are reported in Fig. 4.21.

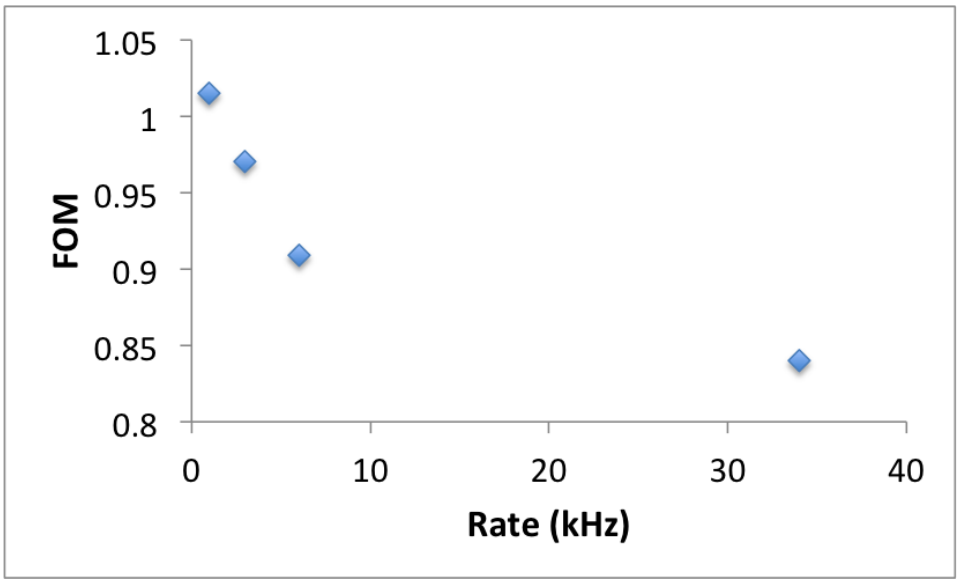

Figure 4.21: NE-213 detector, FOM as a function of rate (AmBe source)

It is evident a worsening of the FOM at high rate of about 20%. There are several sources of instability that contribute to this degradation. First of all there is the possibility of fake neutron events caused by physical effects in the detector as signal pileup or caused by statistical problem as the tail of the gamma-ray peak printing towards the neutron region. With an appropriate pileup filter the first problem can be eliminated, while the second one must be kept in consideration when we set the discrimination threshold for neutrons. During some specific analysis another important contribution of instabilities from the electronics front-end was found, from the test it is evidenced that there are some failure in the FPGA integration procedure

during high rate acquisition. This problem was solved with an appropriate filter that will be discussed in next Chapter.

4.8 Timing properties

Timing properties of the detectors are important in our application when the system is used in active interrogation with tagged neutron beams. In this case the associated alpha particle related to the final state of the neutron emitting reaction D+T is detected inside the neutron generator providing the emission time of the neutron and its flight direction, as defined by kinematics. The acceptance of the alpha particle detector determines the neutron beam spot at a given distance. The detection time of the neutron induces gamma rays inside the material and allows to determinate essentially the travel time of the neutron. Under this light the time resolution of the system defines the depth of the voxel investigated by the neutron beam [5] that, linked to the geometry of the beam spot, provides the definition of the inspected volume.

The typical associated particle detector is a YAP scintillator, which presents very good count rate capability and fast timing properties. The time resolution of SMANDRA detector was studied by measuring gamma-gamma coincidences with a ^{22}Na source between a YAP crystal and the other 3 detector: NaI(Tl), $LaBr_3$(Ce) and liquid scintillator. Moreover, to compare the timing data with values reported in literature and with the results obtained from NIM electronics further studies were performed with a EJ-228 plastic scintillator instead of YAP detector. Intrinsic time resolution of a EJ-228 plastic reaches 300-500 ps with a threshold between 0.2 and 1 MeV [71].

In this work, the data analysis will be performed off-line, and it is necessary to identify the best method to reconstruct time coincidences using the data from the V1720 flash ADC.

4.8.1 Digital CFTD optimization

The easiest way to produce coincidence is comparing FlashADC timestamp values. V1720 acquires data at a 250 MHz rate, with an integration bin of 4 ns. In case of fast detectors with good time resolution (lower than 1 ns) the 4 ns bin width is the best time resolution we can get using the timestamp information. This coincidence will be affected from jitter due to different amplitudes of signals: timestamp is recorded at the beginning of the PreTrigger, generated on a threshold basis and thus not independent from signal amplitude. Instead, in common Constant Fraction Discriminators (CFTD) this issue is solved by using the Amplitude and Risetime Compensated technique (ARC).

The jitter effect is evident in case of NaI(Tl) scintillator that has a rise time of more than 100 ns. Time resolution, that we expected to be about 5 ns (according to previous tests with NIM CFTD), reaches the value of 30 ns [FWHM] as reported in Fig. 4.22. Here, data of gamma-gamma coincidences with ^{22}Na between NaI(Tl) and a YAP scintillator are reported when is used the timestamp information.

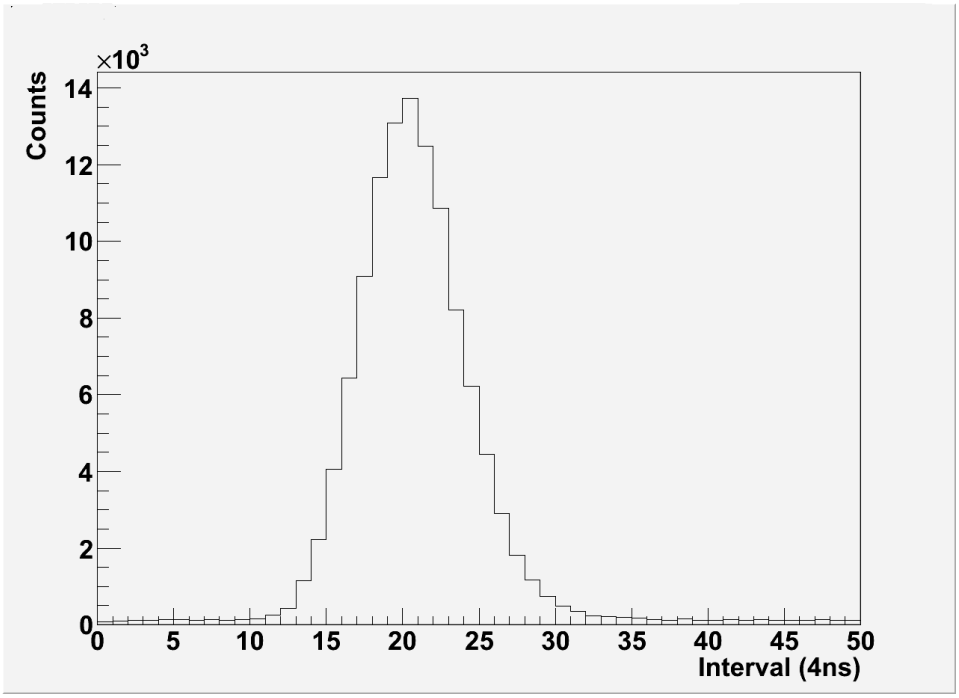

Figure 4.22: Gamma-gamma coincidence peak between NaI(Tl) and YAP using timestamps

Fast detectors (like $LaBr_3$(Ce)) have shorter rise times, and the spread induced by threshold is smaller. Comparing timestamps of $LaBr_3$(Ce) and YAP detector we obtained a time resolution of 6 ns [FWHM]. The correlation is reported in Fig. 4.23.

In order to improve time reconstruction performance we abandoned the timestamps and analyzed directly the digitized signal, looking for a fixed reference point indipendent from the amplitude. The rise time is independent from signal amplitude and from the particular interaction point inside the scintillator volume both in organic and inorganic scintillators. Hence, to realize a simple software CFTD it is enough to calculate the reference time from a threshold that is a constant fraction of the maximum signal. After that, we are able to evaluate the actual time resolution of our detectors.

In Fig. 4.24 are reported gamma-gamma coincidence peaks obtained with the ^{22}Na source, with $LaBr_3$(Ce) and NaI(Tl) detectors in coincidence with the YAP fast scintillator. The width of the peak related to NaI(Tl) narrowed compared to Fig. 4.22; time resolution is now 7.5 ns [FWHM], while $LaBr_3$(Ce) presents a value similar to previous measurements. Further improvements in time resolution need

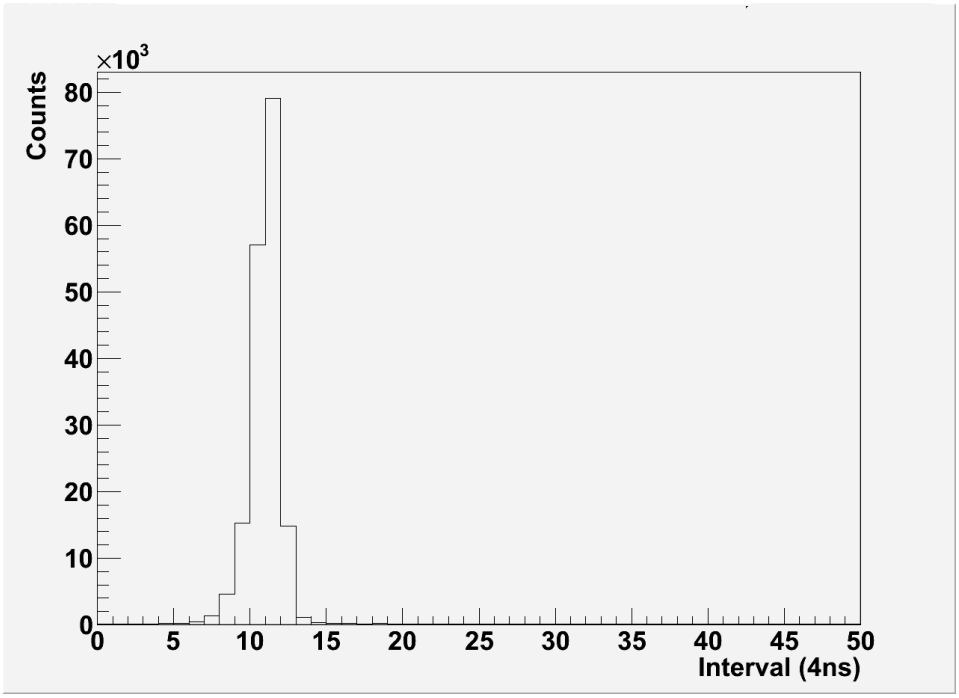

Figure 4.23: Gamma-gamma coincidence peak between $LaBr_3$(Ce) and YAP using timestamps

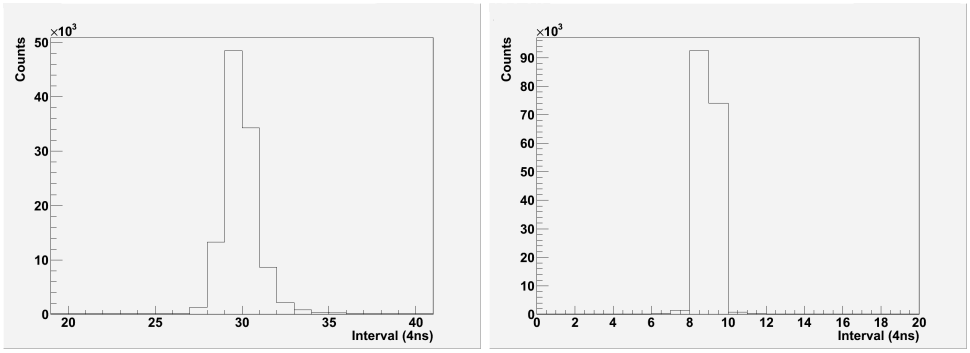

Figure 4.24: Gamma-gamma coincidences with variable threshold adjustment. On the left side result for NaI(Tl) detector, on the right side $LaBr_3$(Ce).

the signal to be interpolated to lower the uncertainty interval under the limit (the bin width) of 4 ns. We compared three different methods for calculating thresholds at a constant fraction of maximum:

- linear fit of the rising part,
- polynomial fit of rising edge,
- analytical calculations.

Another possibility is the implementation of a virtual Constant Fraction Timing Discriminator as described in [72]. For each of these methods the result were evalueted in term of timing resolution but also in the associated computional time, fundamental for a possible online analysis.

The shape of the digitized signal for the 511 keV full energy peak in the $LaBr_3(Ce)$ spectrum measured with the V1720 digitizer is shown in Fig. 4.25 compared to the signal measured with a Tektronix Digital Oscilloscope (TDS2014B 100 MHz, 1. GS/s). The Digital Oscilloscope signal is obtained as the average of 128 pulses above the trigger level. A typical waveform for the fast plastic EJ-228 is also reported derived as an average pulse close to the Compton Edge of the 511 keV transition.

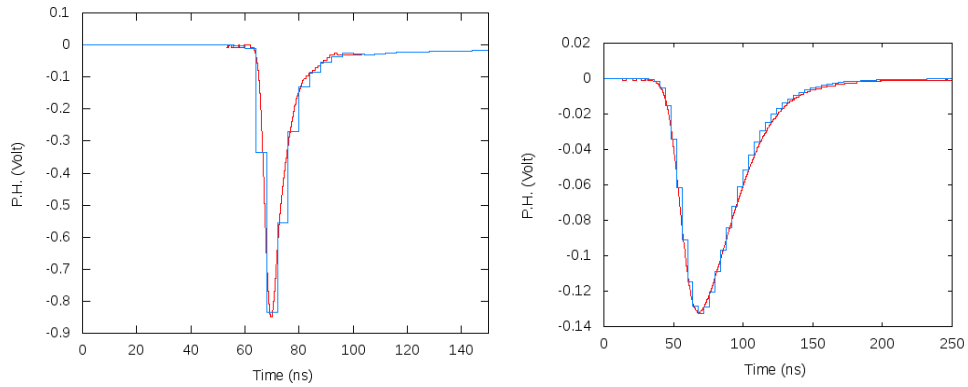

Figure 4.25: Histogram of the pulse height versus time of the $LaBr_3(Ce)$ detector (right panel) and EJ-228 plastic scintillator (left panel) measured with the V1720 digitizer. The continuous line is the result of a measure with a Tektronix Digital Oscilloscope

Linear fit of the rising part

The first method consists of a linear fit of the central portion of the signal rising part, taking as a time reference a threshold corresponding to 50% of the signal amplitude.

This simple method works fairly well if the rising times are long enough (as in the case of NaI(Tl)) so that several points are avaible for the fit. On the contrary, it not works well with fast signals, like liquid scintillators or the YAP. With these detectors, the rising part of the signals is concentrated over 3 or 4 bins, dramatically reducing the statistic and making the fit procedure very unstable. Fig. 4.26 reports

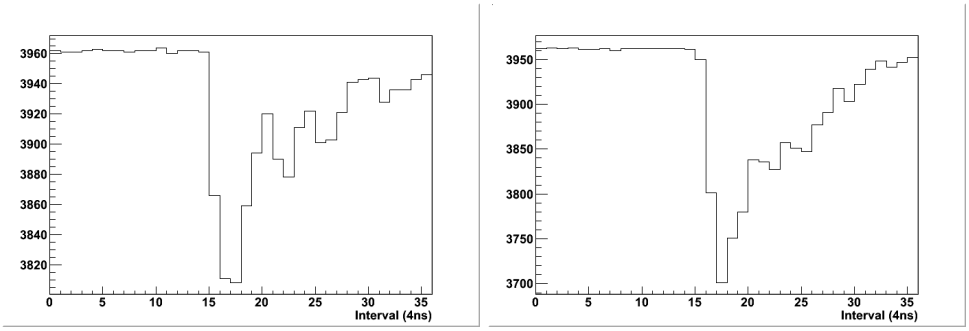

Figure 4.26: Fast signals with very short rising time

two example of fast signals that will produce unstable timing. We can see that the two signals are very similar, but a slight difference in trigger results in a very different profile of the 4 bins of rising ramp due to digitalization resolution, and so a linear fit will produce two different results starting from near the same pulse.

Time resolution achievable with this method is about 8 ns [FWHM] (NaI(Tl) vs. YAP) and 2 ns [FWHM] ($LaBr_3$(Ce) vs. YAP).

Polynomial fit of the rising edge

In a second time, we analyzed the possibility to interpolate with a polynomial function the whole rising edge of the signal, together with some descending point after the maximum. After having determined the function, it is simple to deduce a time reference from a given threshold simply using the inverse function, or trying several time values inside an iterative process. This procedure is the most accurate, but is also very time-consuming from a computational point of view.

The application of this algorithm to download data from the digitizer results in the resolutions of 1.54 ns and 6.50 ns [FWHM] respectively for coincidences of $LaBr_3$(Ce) versus YAP and NaI(Tl) versus YAP.

Fitting the 3 upper points of the pulse peak with a parabolic function improves final resolution, reducing it up to 20 ps in case of $LaBr_3$(Ce) and 50 for NaI(Tl), anyway, computational time would increase by a further 15%.

Analytical calculations

The third method looks at a solution without any fit procedures that increase considerably the computional time. For a given signal (see Fig. 4.25), we calculate the lowest value of the signal corresponding to the maximum in amplitude, and divide this value by two (thus setting a threshold of 50%). Then we search for the two closest bins to this value, interpolate the straight line passing by these two points, reverse it, and finally calculate the time corresponding to the 50% given threshold. The time resolution obtained with this third method correspond to 1.58 e 6.54 ns

[FWHM] respectively for $LaBr_3$(Ce) andNaI(Tl) detectors. There is a little worsening in resolution (about 2% with respect to method 2) totally negligible in our application.

Virtual CFTD

As in common CFTD circuitry, each signal is split in two parts: one signal is delayed by a quantity D and the other is inverted and attenuated using the fraction F. Finally the two signals are summed, originating a bipolar signal that provides the timing information at the zero crossing point.

$$CF[k] = F \cdot samples[k] - samples[k - D]$$

In our process the zero crossing value is determined by linear interpolation between the two data points close to the zero baseline. Fig. 4.27 shows an example of a virtual CFD signal (continuous line) compared to the input one (dotted line).

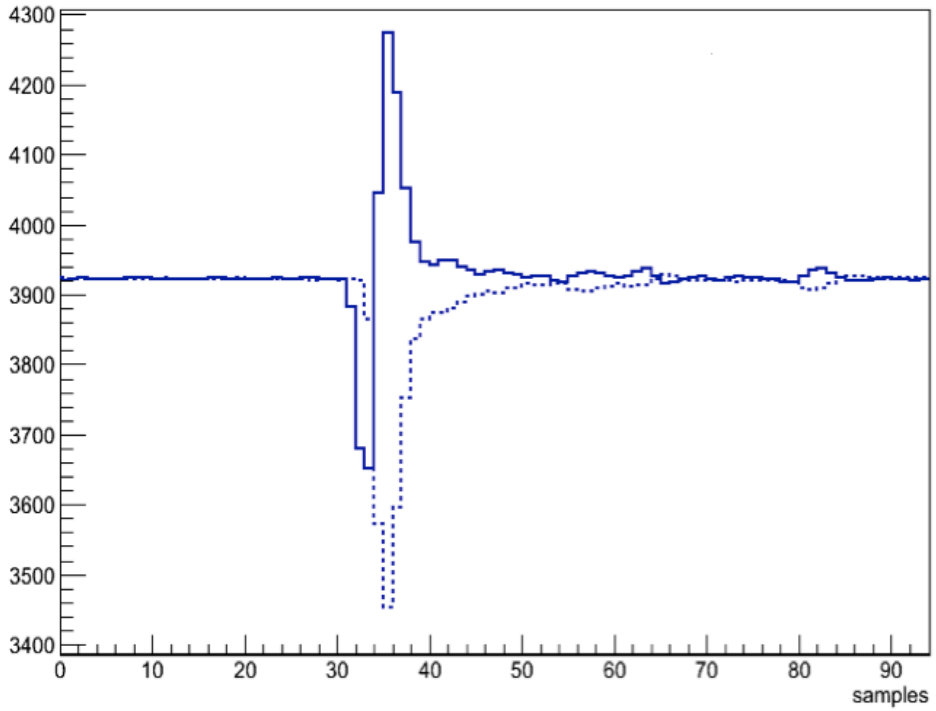

Figure 4.27: Super imposition of the input signal from the detector (dotted line) and the virtual CFD trace (continuous line).

For each detector the parameter F and D is optimized by scanning a range of possible values. Typically, the delay has a value slightly larger than the signal rise time. The fraction is inversely proportional to the height of the signal. The optimized values are reported in Table 4.8 As an example, in Fig. 4.28 is shown the optimization of delay (D) and fraction (F) parameters for $LaBr_3$(Ce).

Detector	D	F
YAP	2	0.7
EJ-228	2	0.7
$LaBr_3(Ce)$	8	0.4
NaI(Tl)	30	0.1

Table 4.8: Optimized parameters for Virtual CFTD. D are reported in bin units.

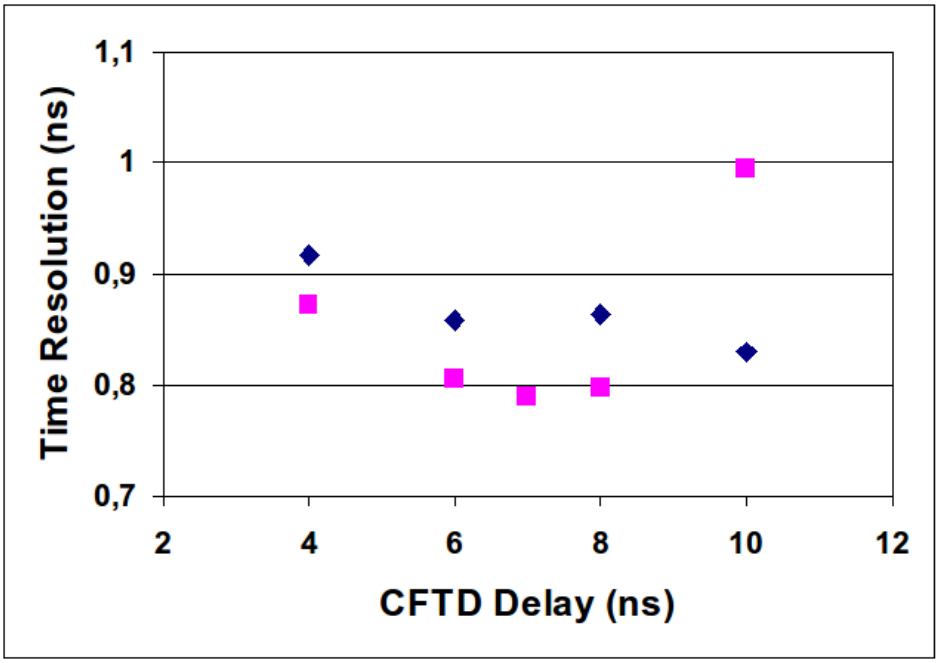

Figure 4.28: Measured time resolution [FWHM] by varying the $LaBr_3(Ce)$ delay D in the virtual CFT: diamonds fraction F=0.2, squares fraction F=0.4

The time resolution are 1.06 e 5.1 ns [FWHM] respectively for $LaBr_3$(Ce) and-NaI(Tl). This method provides the best time resolution obtainable for a digital CFTD.

Computational time

The needed computational time is fundamental for online implementation of the virtual CFTD. We search for the best compromize from time resolution and computational time. As an example we list the computing time of the analysis with the four reported methods on a file containing 600000 events by using a laptop (CPU intel core i3, 4GB RAM):

- linear fit of the rising edge: 45 seconds,
- polynomial fit of the rising edge: 640 seconds,
- analytical calculation: 10 seconds,
- virtual CFD: 15 seconds.

The fourth method provides a very good timing resolution with a computational time slightly worse than method 3 (but better than method 1).

4.8.2 Coincidences with SMANDRA detectors

With the same configuration described above (fast detector YAP), we determined the time resolution of SMANDRA detectors. In Fig. 4.29 we reported the measured time spectra for all detector and the energy histograms with optimized parameters.

Table 4.9 summarizes the measured of time resolution for the three detectors with no threshold and with threshold set to 500 keV for both the YAP and SMANDRA detectors compared with result obtained in previous measurements by using analogical electronics (CFTD Ortec 935).

	V1720 no threshold	V1720 500 keV threshold	CFTD ORTEC
NaI(Tl)	5.96 ns	5.39 ns	4.2-3.5 ns
$LaBr_3$(Ce)	1.40 ns	1.15 ns	0.90-0.650 ns
NE-213	1.78 ns	1.51 ns	

Table 4.9: Resolution comparison between SMANDRA detectors with different electronics

The time resolution obtained with the V1720 card and the simple virtual CFTD seems to be slightly worse compared to the values achieved by using NIM CFTD. This is certainly due to the relatively small number of time bins used in digitizing the signals and, consequently, in managing our virtual CFTD. In our opinion better

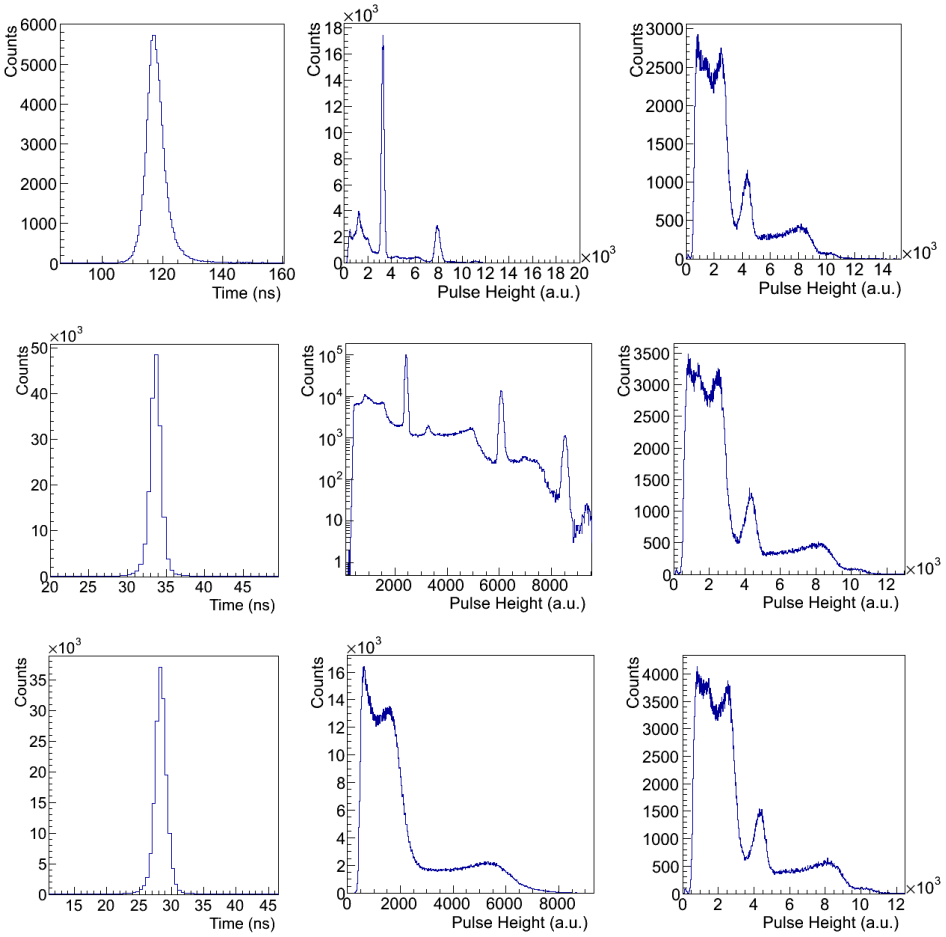

Figure 4.29: Typical timing and energy spectra for SMANDRA detectors. On the upper panel results from NaI(Tl)-YAP coincidences: left side timing spectra, center NaI(Tl) energy histogram and right side YAP energy spectra. Center panel $LaBr_3(Ce)$ detector and bottom panel result from NE-213 liquid scintillator.

results might be obtained by interpolating the zero crossing region with a polynomial function and using faster digitizers. This would be paid in terms of computing time needed to process the data sets. For SMANDRA application the time resolution obtained in this study is sufficiently good: a time resolution of $\Delta t = 0.8$ ns [FWHM] reflects in about 4 cm depth for the inspected voxel for 14 MeV tagged neutrons. Voxel depths of the order of 10 cm are a normal choice to ensure the required statistical accuracy in the gamma ray spectra compatible with acceptable inspection times [73].

4.8.3 Further improvements in timing optimization

The optimal working condition of virtual CFTD is the signal obtained with a rise time of 4-5 bin in order to get a good determination of zero crossing. For very fast signals (as example in case of EJ-228) the rise time is concentrated in one or two bin and this introduces systematic errors in the achievable time resolution. Fig 4.30 shows the spectrum of coincidence between two EJ-228 produced by virtual CFTD. The double peaks disappears for detectors with larger rise-time as the $LaBr_3$(Ce). The same happen for signal selected in the data analysis with a rise time characterized by a fixed number of time bins.

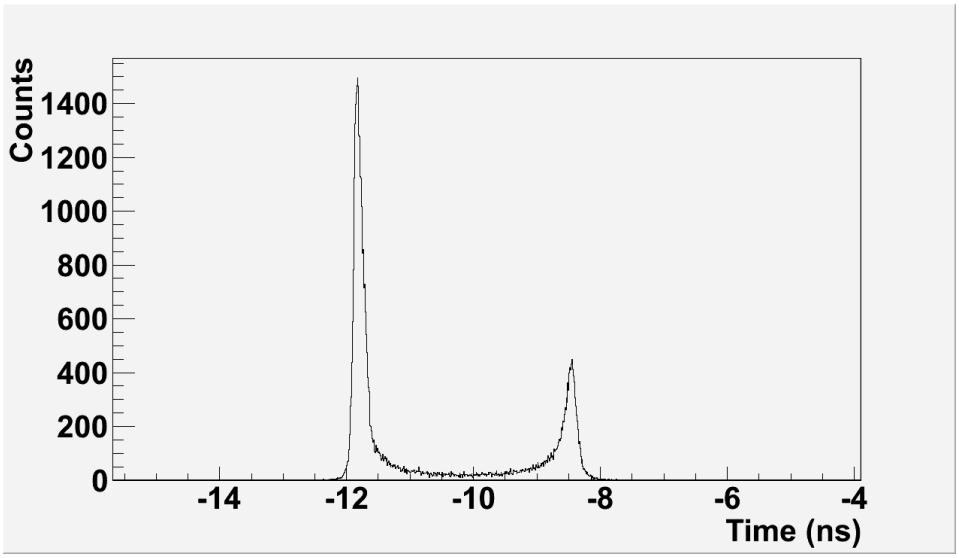

Figure 4.30: Coincidence spectra for two EJ-228. The sistematic errors caused by the reduced number of bin in the sample digitization produces a double peak in the timing spectra.

To overcome this problem there are two solutions. The first consists in increasing the rise time of the signal through a capacitor, the second one consists in using a faster FlashADC.

The experimental setup was performed by replacing two detectors EJ-228 40 cm away each from the other. It was recorded gamma-gamma coincidence with a source of ^{22}Na, centrally located. For each run we saved two spectra: the first in

selftrigger mode in order to verify the stability of energy calibration, the second in coincidence to calculate time resolution between the two detectors. We will call the two detectors Left and Right, powered at 1800 V and 1750 V respectively, to have similar gain in pulse heigth spectra. The voltage is close to the reference values of the photomultiplier.

Increasing rising edge with capacitor

The introduction of a capacitor (parallel-connected) in the input circuit of the FlashADC produces an increase of the rising time of the signal proportional to the capacitance. For each capacitor, the CFTD parameters (F and D) need to be optimized. The time resolution is calculated as the RMS of the spectrum because the presence of the double peak makes impossible to perform any gaussian fit. If there is no systematic error that causes the double peak, the distribution will be Gaussian and the RMS of the spectra will coincide with the σ of the distribution. Fig 4.31 shows RMS: data are reported versus the capacitance as obtained with optimized CFTD parameters.

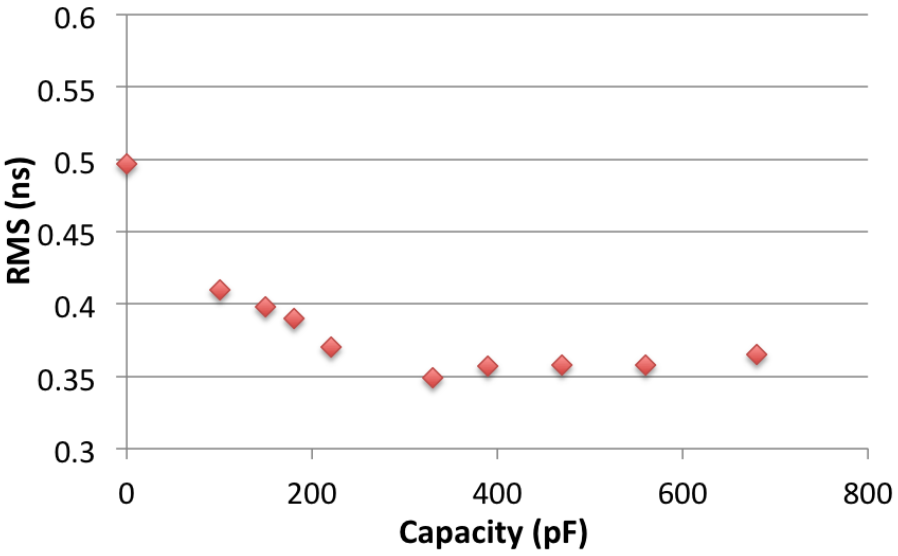

Figure 4.31: RMS (ns) as a function of the capacitance. The best resolution is obtained with a capacitor of 330 pF.

There is a minimum between 220 and 390 pF with a RMS value of about 0.35 ns. At higher capacity value, the rising time of the signal becomes very long and then the time resolution tends to slowly rise. The results reported in Fig 4.31 suggest that there is an optimal value for the rise time of the signal that produces the best temporal resolution with the V1720 digitizer. To understand what is the optimal lenght of the rise time, we are going to associate to each value of the capacity the average number of bins in the rising part of the signal. Fig 4.32 shows the correlation

bewteen the condensator's capacity and the number of bin in the rise front of the signal.

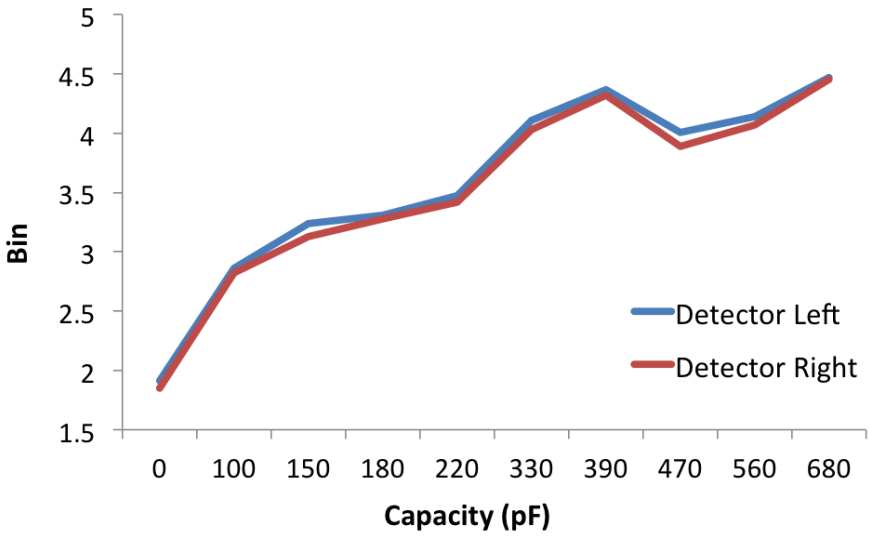

Figure 4.32: Lenght of the rising edge of the signal versus condensator's capacity

It is evidente a non-linear dependency with a drop over 400 pF. To better undestand this trend we compare the various signals to see how the introduction of the capacitor affects the shape of the pulse. The "reference" scope is calculated by the average of all pulse inverted and appropriately normalized to an unitary intergral. Fig 4.33 reports the "reference" scope of four representative capacitor from 0 to 680 pF and the comparison between the two values where is the discontinuity.

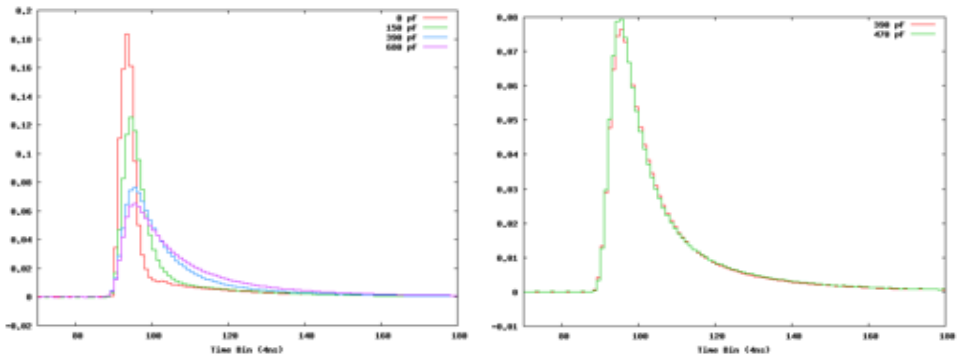

Figure 4.33: In the left panel the "reference" scope for four different capacitor, in the right panel a focus on two particular values.

It is evidente that the introduction of a capacitor acting as a RC filter by increasing the duration of the signal and decreasing its amplitude. Higher is the value of the capacitor and greater is the number of bins in the signal. The modification of the signal shape partially precludes the possibility of performing a good Pulse Shape Discrimination to distinguish between neutron/gamma ray. Looking to the

Capacity (pF)	F	D	Det Left	Det Rifght
0	0.7	2	1.91	1.85
100	0.5	3	2.86	2.82
150	0.5	3	3.24	3.13
180	0.4	3	3.31	3.28
220	0.4	3	3.47	3.42
330	0.2	4	4.11	4.03
390	0.2	4	4.37	4.32
470	0.3	5	4.01	3.89
560	0.3	4	4.14	4.07
680	0.2	4	4.47	4.45

Table 4.10: Optimized CFTP parameters and number of bins in the rising edge of the two detectors.

right panel of Fig 4.33, we can undestood the reason of the discontinuity in Fig 4.32. By increasing the value of the capacitor from 390 to 470 pF the signal undergoes a change different than expected. Most likely over a certain value the capacitor starts to modify the tail more than the rest of the signal causing this drop.

Another interesting point is the dependence of the temporal resolution respect to the number of bins in the rising edge of the signals reported in fig 4.34. The optimal

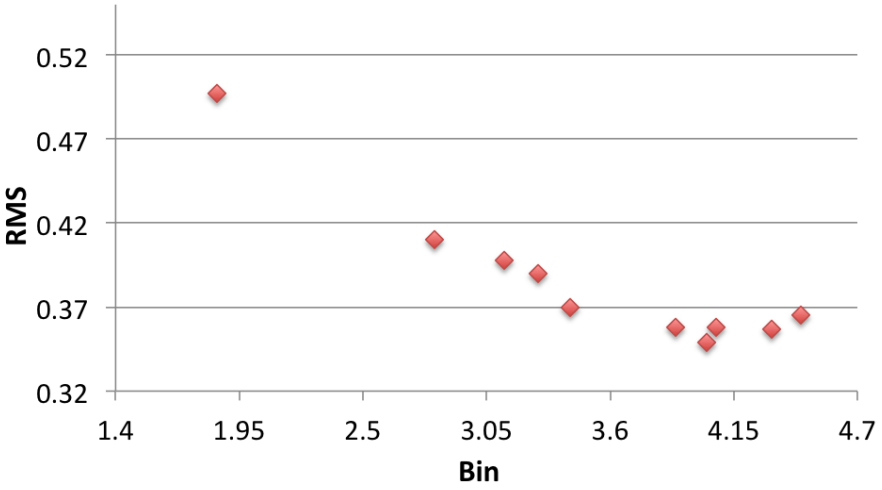

Figure 4.34: Time resolution versus the number of bins in the rising edge of the signal

number of bin, to minimize the time resolution, is equal to 4. In this configuration we need a capacitor of 330pF to shape the EJ-228 signal in order to obtain an average rising front of 4 bins. For completeness we reporte in Table 4.10 the values of optimized CFTD parameters and the number of bins in the average rising edge for each used capacitor.

High voltage dependence

The ratio energy/channel increases with the capacitance of the detector. It is important to control this increase to set properly threshold and energy calibration. Using ^{22}Na source we are able to verify that the decrease of the gain in the energy spectrum is about 10% between the maximum value of 680pF and the first spectrum without capacitor, while the value of the energy resolution remains almost constant.

To compensate the loss of gain we tried to increase the operating voltage of the photomultiplier to see if there is an improvement in the time resolution. In this test the capacity was set at the value of 330 pF. The results do not show significant improvements, the RMS remains equal to the minimum value found earlier (0.35 ns) within errors and the gain increases of 40% for a voltage of 1900 V. The increase of voltage does not lead to substantial improvements in the temporal resolution.

V1751 measurements

The V1751 is a 1GS/s flashADC of the same family of V1720. The higher sampling rate allows to have a width of the integration bin of 1 ns and consequently do not require any additional capacitors to analyze the rise time of the signal in case of fast detector. The length of the rise time has an average value of 4.5 bin that is in agreement with the previous tests performed with V1720 and capacitor. With no threshold (about 50 keV) we obtained a time resolution of 0.27 ns and setting a threshold of 100 keV the resolution decreases to 0.20 ns. With the same threshold the V1720 digitizers plus a 330 pF capacitor obtains a RMS of 0.34 ns with an worsening of 30% in time resolution.

Furthermore using a ^{60}Co source it is possible to study the correlation between the time resolution and the energy threshold up to the value of 700 keV. Figure 4.35 compares the results of V1751 digitizer in terms of time resolution [FWHM] with those obtained by the same detectors with standard NIM electronic. It is clear that the time resolution obtained with digitizer is very close to that obtainable with standard NIM electronics altough the possible loss of resolution in digitizing the signal. Most likely refining the CFTD software the results would be slightly better. Furthemore it is interesting to note that time resolution of digitizer is less sensitive to the increase of the threshold than standard NIM electronic. The filter on the signal's shape made by digitizier cleans a lot of noise that in analog electronics inevitably ends in CFTD.

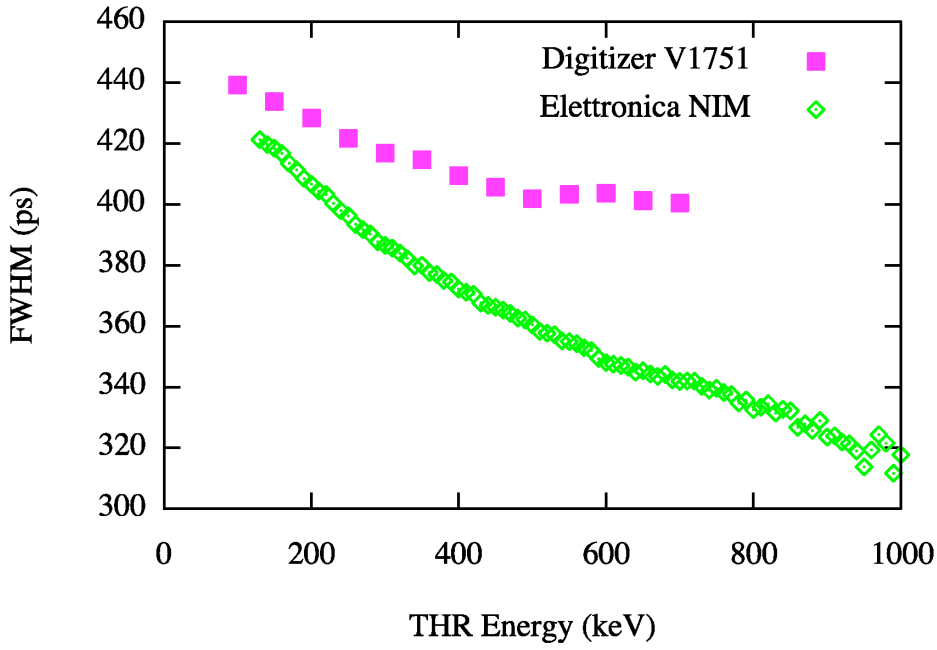

Figure 4.35: Comparison of time resolution [FWHM] versus threshold energy for V1751 digitized and standard NIM electronic.

Chapter 5

Sensitivity tests

5.1 Standards

Standards play an important role in the characterization of an inspection system. They may establish size or shape or capacity of a given device and specify the required performances. They also define the test procedures so that there is no misunderstanding among those quoting a given system performance.

International Standards are produced by Organizations like the International Electrotechnical Commission (IEC), the International Organization for Standardization (ISO) and the International Telecommunication Union (ITU). IEC covers electrotechnology and related conformity assessment, ITU covers telecommunications and ISO covers nearly all other technical fields, a number of service sectors, management systems and conformity assessments.

In addition there are several other Institutes that serve as national coordinator for standards, for example the American National Standards Institute (ANSI) is the official U.S. representative for the ISO and IEC.

The International Atomic Energy Agency (IAEA) has recently published the first techinal guidance: *Technical and Functional Specifications for Border Monitoring Equipment* [74] originated from the results of the *Illicit Trafficking Radiation Detection Assessment Programme* (ITRAP) completed in 2000.

For our purpose we focus on three particular standards that provide rules and guidelines to characterize radiation monitoring systems. Two of them are defined by IEC, the third one is the Technical Guidance published by IAEA.

5.1.1 IEC standard

IEC (International Electro-technical Commission) defines a set of standard for detection systems dedicated to the monitoring of ionizing radiation in various operational fields. Two of them are of particular interest for our project:

1. IEC 62244 Radiation protection instrumentation - Installed radiation moni-

tors for the detection of radioactive and special nuclear materials at national borders,

2. IEC 62327 Hand-Held instruments for the detection and identification of radionuclides and additionally for the indication of ambient dose equivalent rate from photon radiation.

As far as we know, there is no specific IEC documents for mobile systems such as SMANDRA.

The main difference between the two standards is that hand-held devices are required to detect not only the presence of a radiation source, but also to be able to identify it. From this point of view, SMANDRA performances can be directly compared to IEC62327 requirements as for gamma and neutron sensitivity, further IEC62244 parameters can be considered in case of evaluating the possible use of SMANDRA technology in portal installations.

Briefly, IEC IEC62327 rules require:

- in case of gamma rays, to rise an alarm within 3 seconds if radiation levels exceed threshold, and to identify the source in 1-2 minutes for a given dose of 0.5 μSv/h on the front face of the detector,
- in case of neutrons, to get an alarm within 10 seconds in presence of a ^{252}Cf source that produces a dose of 3 μSv/h on the detector (corresponding to a source emitting $2 \cdot 10^4$ neutrons/s placed at a distance of 25 cm).

According to IEC, a criterion for the acceptability of an instrument is a Probability of Detection PD greater than 90% at a Confidence Level of 95% (PD and CL are defined in the next section).

5.1.2 IAEA Technical guidance

The Technical Guidance prepared by IAEA provides technical and functional requirements for equipment used at international borders for the interdiction of illicit nuclear and radiological threats.

The document is addressed to all instruments used by FLOs (Front Line Officers) and to experts divided into the following types:

- fixed radiation portal monitors (RPMs), with a subcategory of Spectrometric Radiation Portal Monitors (SRPMs), featuring real-time radionuclide identification,
- personal radiation detectors (PRDs),
- hand-held radionuclide identification devices (RIDs),

- hand-held neutron search devices (NSDs),
- portable radiation scanners (PRSs).

We are interested in particular to RIDs, NSDs hand-held systems and Portable radiation scanners (PRSs). Hand-held systems are used to detect, localize, and identify radioactive and nuclear material, as well as provide gamma dose rate measurement to ensure radiation safety during the localization and identification process. RIDs is conceived as an instrument usable in conjunction with present monitoring devices such as PRDs. They are used for detection in targeted search situations to give dose rate, type of radiation (neutron or γ-ray) and identification of the individual isotopes.

PRSs are designed mainly for covert detection of unauthorized or undeclared activities but are also useful in specific situations where the usage of fixed portals or hand-held systems are not possible. For example, they may be used aboard large vessels, such as airplanes or ships, at public/urban areas and at borders without law-enforcement control. This instrument has the same main functions of detection and identification as an RIDs but its design is significantly different because they are using large detectors (for the identification of weaker sources), the presence of a neutron detector, a real-time/automatic identification mode and flexibility for changing backgrounds (e.g., for mobile use).

The common requirements for these systems are the following:

- false Alarm Rate (FAR) for either gamma rays or neutrons during operation. It shall not be more than one per hour,
- probability of detection of 90% with a confidence level of 95%,
- detection of radioactive material that produces a dose rate of 0.05μSv/h in the point of closest approach to the instrument and moves with a speed of 0.5 m/s. ,
- energy range for γ-ray from 50 keV to 1.33 MeV.

In particular for hand-held systems:

- time for radionuclide identification less than 100 seconds at the exposure rate of 0.05 μSv/h,
- trigger a neutron alarm within 5 seconds with a ^{252}Cf source of $2.0 \cdot 10^4$ n/s placed at 0.20 m from the instrument[75].

For portable radiation scanners the following requirements are needed:

- time for radionuclide identification less than 60 seconds at the exposure rate of 0.05 μSv/h,

- detection of a neutron source that emits $1.2 \cdot 10^4$ neutrons/s and moves with a speed of 0.5 m/s at a distance of closest approach between the source and a PRS of one meter.

5.2 Statistical definitions

The evaluation of a system whose aim is to detect radioisotopic sources or SMN shall satisfy strict test protocols. The necessary statistical background has recently revised in [76].

In particular it is requested that the instrument has a certain value of PD (Probability of Detection) to reduce as much as possible the PFA (Probability of False Alarm). These two values must be defined and experimentally testified for a certain Confidence Level (CL). In the next paragraphs we will analyze the meaning of these terms.

First of all, we define the Binomial Discrete Density Function $b(m, n, p)$ that is the basis of following definitions:

$$b(m, n, p) = (Pr(BIN(n, p)) = m) = \frac{n!}{m!(n-m)!} p^m (1-p)^{n-m}$$

where $m = 0.1, \ldots, n$ is the number of successful events in the search for hidden materials in n independent attempts with $p = PD$ (see [77]). PD is here intended as the probability to succeed in finding hidden sources.

Cumulative function $CL(m, n, PD)$, for a given series of n measurements and a number m of successes with a fixed PD, is defined as:

$$CL(m, n, PD) = \sum_{j=0}^{m-1} b(j, n, PD)$$

with $x = 0.1, \ldots n, 0 \leq p \leq 1$, Binomial Cumulative Distribution Function ($BINCDF$) can also be defined as follows:

$$BINCDF(x, n, p) = Pr(BIN(n, p) \leq x) = sum_{k=0}^{x} \binom{n}{k} p^k (1-p)^{n-k}$$

To find the maximum number of identification m_c with a given PD and a desired CL we must reverse the upper equation:

$$BINCDF(m_c - 1, n, PD) \geq CL$$

BINCDF is a discrete step-function in the x variable, thus it does not have a continuous inverse function. The value m_c must be intended as the first integer for which $BINCDF(mc-1, n, PD)$ is greater than CL.

$$m_c = INVBINCDF(CL, n, PD) + 1$$

This reverse function can be found ready-to-use inside statistical function of many spreadsheet, eventually under other names. Some of them do not return the maximum number of positive identification, instead they calculate the maximum number of failures (M_c); in this case we speak of Probability of False Alarm (PFA). When $PD = 1 - PFA$ the two quantities are connected by a simple formula:

$$m_c + M_C = n$$

At this point we calculate the maximum acceptable number of wrong results for a given PD or PFA with a fixed CL. Standards require a Confidence Level of 95%, Table 5.1 contains the maximum number of failures for various PD/PFA and different values of the attempts number$n$.

PD	0.9	0.8	0.7
PFA	0.1	0.2	0.3
n=2	*	*	*
n=3	*	*	*
n=4	*	*	*
n=5	*	*	*
n=6	*	*	*
n=7	*	*	*
n=8	*	*	*
n=9	*	*	0
n=10	*	*	0
n=11	*	*	0
n=12	*	*	0
n=15	*	0	1
n=20	*	0	2
n=25	*	1	3
n=30	0	2	4
n=40	0	3	6
n=50	1	5	9
n=60	1	6	11

Table 5.1: Maximum number of failures for various PD/PFA and n attempts

Working with a PD of 90% and at a CL of 95% we need at least 29 consecutive positive tests to satisfy requirements. There is a way of evaluating directly the required number of consecutive positive results as a function of CL and PD.

$$a = \frac{\log(CL)}{\log(PD)}$$

The number of attempts will be the smaller integer greater than a. Fig. 5.1 shows the dependance of a function of PD for different values of CL.

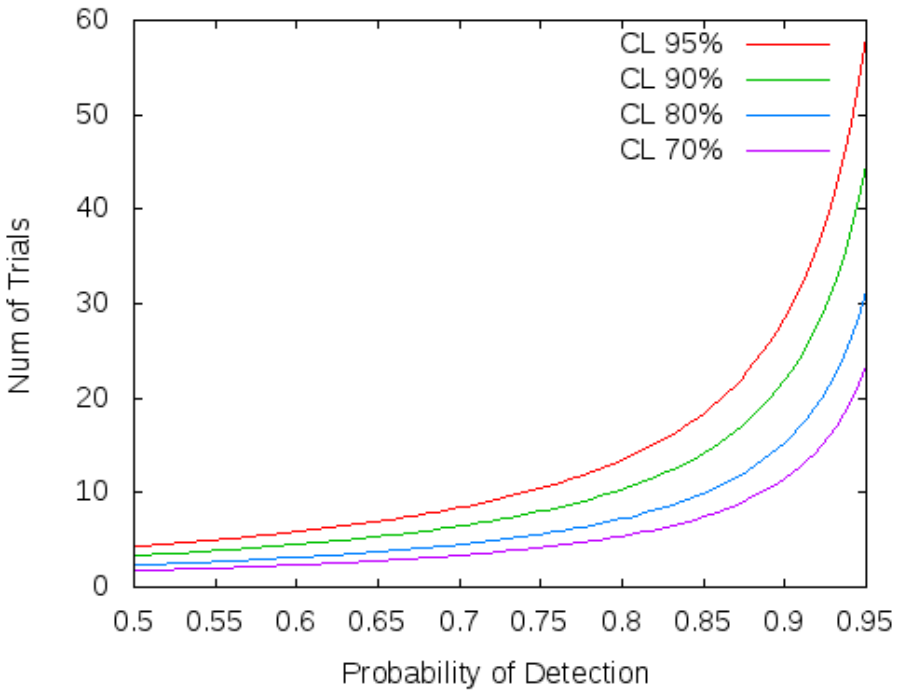

Figure 5.1: Number of attempts as function of PD and CL

5.3 Definition of Detection Probability

Radioactive decay follows Poisson statistics, so we must take it into account in defining the thresholds. Poisson distribution is a discrete probability distribution that expresses the probability for n events to be realized in a given time, providing that their medium number is λ. This distribution is also known as "rare event's law"; it is defined as:

$$P(n) = e^{-\lambda}\frac{\lambda^n}{n!}$$

for any n belonging to naturals. If we assume that the detector produces a normal distribution of responses, the presence/absence of a particular threat might be expected to produce two normal distributions [78] (see Fig 5.2).

Using components defined in Fig. 5.2, a variety of different performance metrics have been established, the most well-known are summarised in Table 5.2. One of the most used is the Detection Probability (PD), already introducted in Section 5.2. This component represents the ability of a test to correctly identify target presence,

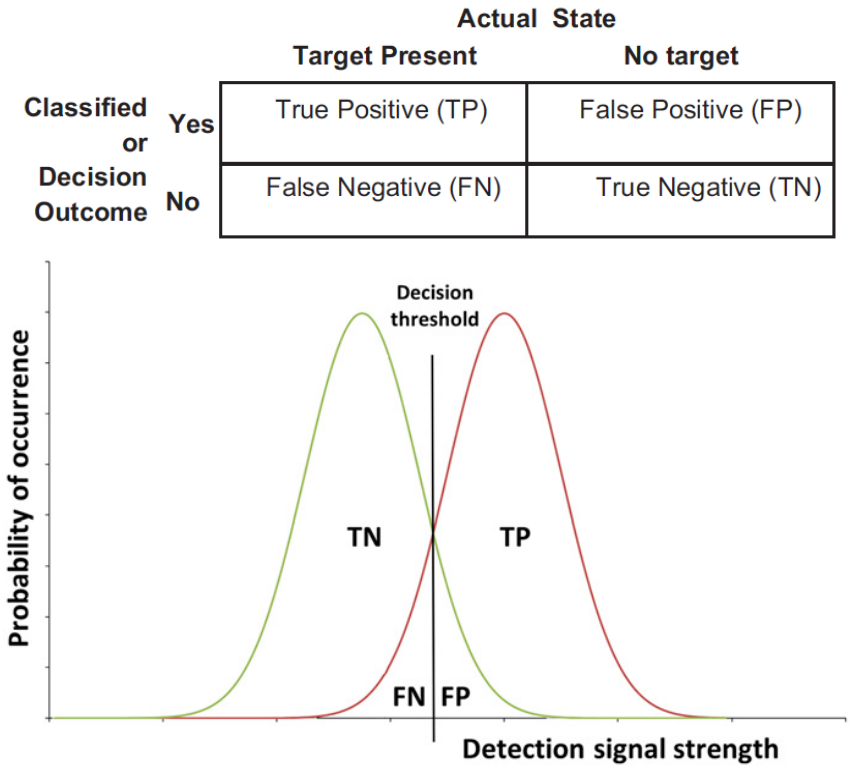

Figure 5.2: In the upper panel the confusion matrix and in the lower panel the associated decision distributions with respect to detection signal strength [78]

given that a target is actually present. A second key performance metric is the False Alarm Rate, that represents the rate at which items are incorrectly labelled as a threat when they are in fact benign.

Quantity	Definition
Detection probability, true positive rate	$TP/(TP+FN)$
True negative rate (TNR)	$TN/(FP+TN)$
False alarm rate or false positive rate	$FP/(FP+TN)$

Table 5.2: A selection of common quantities derived from the confusion matrix.

Note that the threshold in Fig. 5.2 is placed at the point sometimes referred as the optimal value. Optimal means that misclassification of items (False Positive and False Negatives) is minimized. However, in our as well as in many other applications this would be a poor choice of decision threshold: it may be considered better to shift the threshold such that the number of false positive is minimized and true positive maximized according to the requirements of PD and FAR.

5.3.1 Threshold

Once we know the average number of background events (λ), it is possible to set a threshold in accordance with standards. For example, the IAEA standars requires that there is no more than one false positive alarm per hour. If the sampling time is 3

seconds this means that FP is the 0.083% of the total background events ($TN+FP$). Therefore the threshold must be set at 99.917% of the total integral of Poisson distribution. The integral of the Poisson distribution is defined as:

$$I = \frac{\Gamma(k+1,\lambda)}{k!}$$

where $\Gamma(x,y)$ is the incomplete gamma function and k belongs to natural positive number. When $I > 1 - PFA$ the first integer k is set as threshold.

In Fig. 5.3 is reported Poisson distribution and integral for various λ.

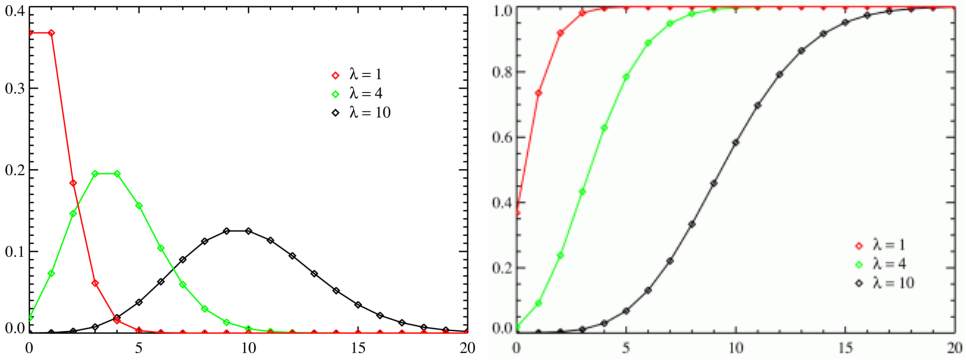

Figure 5.3: In the left panel the Poisson Distribution, in the right panel the Cumulative distribute function (CFD). Curves for different value of λ are shown.

5.4 Neutron Sensibility Tests

IEC62327 standard for hand-held instruments requires the emission of an alarm within 10 s of measurement. We started with the acquisition of 10 spectra, each with a duration of 10 seconds, using PSD on NE-213 detector to count the number of neutron events. In a first step we determined the best cut in energy domain corresponding to minimum PFA, comparing 10 different background counting windows from 200 to 1400 keVee with steps of 200, and calculating the number of neutron events above each of these thresholds.

From these background acquisitions we derived the average neutron number over all the runs and calculated the correspondent Poisson function P(n). Then, when the integral of $P(n)$ overcomes 90% of total, the corresponding number of events is taken as threshold.

In Table 5.3 we report the number of neutron events recorded in the first 10 acquisitions with 10 different energy thresholds. AVG refers to average values for each threshold, and THR is the alarm threshold (PFA = 10%).

We see that considering the energy cut at 200 keVee the alarm threshold obtained counts 8 events while the number of neutrons measured for all the ten background

Cut (keVee)	200	400	600	800	1000	1200	1400	1600	1800	2000
Run 1	6	1	0	0	0	0	0	0	0	0
Run 2	7	1	1	1	1	1	1	1	1	1
Run 3	3	0	0	0	0	0	0	0	0	0
Run 4	2	0	0	0	0	0	0	0	0	0
Run 5	4	0	0	0	0	0	0	0	0	0
Run 6	4	1	0	0	0	0	0	0	0	0
Run 7	3	1	0	0	0	0	0	0	0	0
Run 8	6	2	0	0	0	0	0	0	0	0
Run 9	4	1	0	0	0	0	0	0	0	0
Run 10	5	0	0	0	0	0	0	0	0	0
AVG	4,4	0,7	0,1	0,1	0,1	0,1	0,1	0,1	0,1	0,1
THR	8	2	1	1	1	1	1	1	1	1

Table 5.3: Neutron events with different thresholds

runs is under this value: hence we have 0 false alarms (FA). Raising the threshold to 400 keVee it is verified the presence of 1 FA, as for higher values of energy cut.

In a second step the Californium source (10^4 neutron/s) was placed at the distance of 100, 120 and 140 cm to experimentally determine the PD of our system.

Table 5.4 reports the number of the alarms at each distance for all the ten energy threshold, considering 10 s acquisition repeated 10 times.

Cut (keVee)	200	400	600	800	1000	1200	1400	1600	1800	2000
100 cm	10	10	7	9	8	5	4	4	3	2
120 cm	10	10	6	7	4	2	0	0	0	0
140 cm	10	9	7	6	4	4	2	1	1	1

Table 5.4: Number of alarms. For details see the text.

Only with the lowest cut (200 keVee) we have 10 consecutive successes at every distance.

Working with a PD of 90%, to testify that out CL matches the value of 95% as required by the standards, we must run a test with at least 29 consecutive detections. Consequently the source was placed 120 cm far from the detector, and we acquired 30 runs with the source and 30 runs of background with higher statistic were acquired. Table 5.5 lists the results for the first 3 cuts in energy.

The results gave the final confirmation that the best energy cut is 200 keVee, and that for that value our system has a PD of 90% at a Confidence Level of 95% with a 10^4 n/s source placed at 120 cm from the detector.

Considering that IEC62327 standard for hand-held devices requires such performance with more intense source placed at a distance of only 25 cm from the detector, we can reasonably conclude that the neutronic part of SMANDRA not only satisfies

Cut (keVee)	200	400	600
Count threshold	9	3	1
FA background	0 out of 30	1 out of 30	9 out of 30
Positive alarms, source in position	30 out of 30	29 out of 30	29 out of 30

Table 5.5: Positive alarms

IEC62327 requirements, but also that our system presents a sensitivity about 60 times greater that required in case of an hand-held instruments.

5.5 Gamma Sensibility Tests

IEC62327 standard requires an alarm within 3 seconds of acquisition in presence of a gamma-ray emission in addition to the natural background.

To check the SMANDRA sensitivity to gamma rays we considered both NaI(Tl) and $LaBr_3$(Ce) detectors. We computed the total integral of gamma spectra, since we are interested in having an alarm in presence of any kind of radioactive source. The gamma-ray performance must be documented in an energy range from 59 to 1330 keV, corresponding to the characteristic energies of ^{241}Am and ^{60}Co, respectively.

As in the case of neutrons, we performed 30 background acquisitions with NaI(Tl) and $LaBr_3$(Ce) detectors to calculate the alarm thresholds, and 30 more acquisition with various gamma sources placed at different distances from the detectors.

First measurement has been carried on with a ^{60}Co source that has an activity of 400 kBq, providing a dose of 0.144 μSv/h at the distance of 1 m. IEC62327 standard requires to identify any gamma source that increases the background dose of 0.5 μS/h, given that at 0.5 m we are over the alarm threshold. We placed the source at the maximum distance allowed by the lab room: 2.71 m. In these conditions the source provided a dose of 0.02 μSv/h on the front face of the detector.

The test has been repeated with a ^{241}Am source with an equivalent dose of 2 orders of magnitude smaller than ^{60}Co. We put the source 80 cm far from the scintillators. At this distance it provided a dose of 2.5 nSv/h.

Table 5.6 shows the results for the alarm tests performed by using the same procedures as the one described before for the neutrons.

For both NaI(Tl) and $LaBr_3$(Ce) detector IEC62372 standards are satisfied with 90% of PD at 95% CL. Also in this case our system has a better performance compared to requirements, as it provides the same PD for much smaller radiation dose rates.

Detector	NaI(Tl)	$LaBr_3$(Ce)
Threshold (events in 3 s)	2527	757
FA on background	0 out of 30	2 out of 30
Alarms with ^{60}Co at 271 cm	30 out of 30	30 out of 30
Alarms with ^{241}Am at 80 cm	30 out of 30	29 su 30

Table 5.6: Results of the alarm tests

5.6 Source identification

5.6.1 Identification process

The identification of a radioactive source from a single gamma spectrum is a complex problem, and many different algorithms have been studied. The idea underlying all these solutions consists in the comparison of the spectrum with one or more other spectra of known sources or a combination of them.

Many factors contribute to the complexity of the task, and each peak could be evaluated under different parameters with the following related issues:

- energy: different sources can present similar peaks, identical within the limits of resolution; furthermore, calibration can be not perfectly linear,
- resolution: even in state-of-the-art detectors, resolution is a function of energy and may be affected from other dependencies,
- intensity: sources can be shielded by materials resulting in one energy-dependent attenuator; this makes nearly impossible the use of criteria based on relative intensities.

In this work a simple model has been used, based only on energies and resolutions. It will be a working basis for future upgrade of the software.

The first step consists in the creation of a small database of sources, each with the number of expected peaks and their energies (in keV). Feasible example can be ^{22}Na (511, 1274.5), ^{60}Co (1173, 1332), ^{137}Cs (661.7) and the internal activity of $LaBr_3$(Ce) (1460). This set can be extended in future.

The actual analysis of a spectrum starts with the Compton Background subtraction procedure that is part of ROOT analysis functions. In Fig. 5.4 the red line shows a calibrated spectrum of ^{22}Na source as acquired from the digitizer using the NaI(Tl) detector, whereas the black line shows the same spectrum after automatic Compton subtraction.

Next step is the application of an algorithm for peak identification (see Fig. 5.4) through a gaussian fit. From this, energy and sigma values that allows to obtain

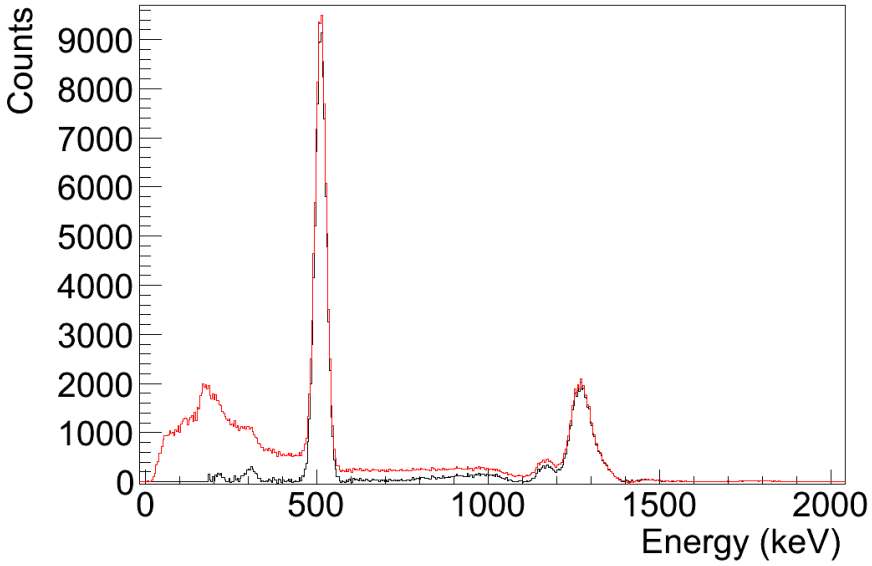

Figure 5.4: Red line is the raw spectrum acquired from NaI(Tl) detector with a ^{22}Na, black line shows the same spectrum after automatic compton subtraction

the percent energy resolution for each peak. Such parameters are saved, as in the example shown below:

```
Found 2 peaks:

1) Mean: 1158.634888     Sigma: 25.479431
   Res.: 4.914968%       Res(E): 4.759285%

2) Mean: 1315.373779     Sigma: 27.046551
   Res.: 4.595579%       Res(E): 4.466737%
```

Res(E) is the predicted resolution that is function of the detector NaI(Tl) or $LaBr_3$(Ce) and gamma ray energy, obtained in first approximation by scaling as $\frac{K}{\sqrt{E}}$, where E is the energy and K is a parameter empirically determined.

Peaks with resolution lower than predicted or larger more than a factor 2 are rejected. The value of 2 has been proved to be a good compromise between the need of filtering peaks with poor resolution and the possibility that - for many reason - the actual resolution can be often larger than expected. Further improvements in the peak rejection criteria are left for the future.

Finally, the algorithm starts a loop over known sources from the database, trying to find the nearest detected peak for each expected energy. Sources are classified by two parameters: the number of peaks matched, and the S-index, that is the average absolute distance from expected energies, normalized to sigma units:

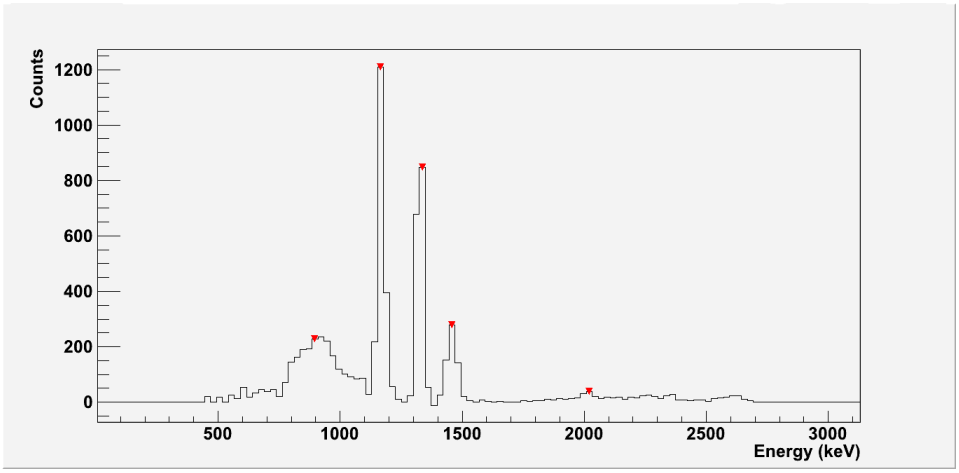

Figure 5.5: Calibrated spectrum of ^{60}Co source, $LaBr_3$(Ce) with internal activity

```
Found 2 peaks:

1) Mean: 1158.634888     Sigma: 25.479431
   Res.: 4.914968%       Res(E): 4.759285%

2) Mean: 1315.373779     Sigma: 27.046551
   Res.: 4.595579%       Res(E): 4.466737%

Nearest peak to 1173 is 1158 with sigma 25.479431
Nearest peak to 1332 is 1315 with sigma 27.046551
*** Source: 60Co         Matches: 2/2          S-Index: 0.589259
```

Continuing in our example, we see that the algorithm tried to find ^{60}Co energy peaks in the measured spectrum. ^{60}Co presents two characteristic peaks very near each other, and both match (2/2) with an average distance of 0.58 sigma units.

For every source, if a peak doesn't match within 3 sigma units, it is not counted. If a source is missing a match for more than 25% of expected peaks, it is marked as "not found".

At present time, this simple but automated procedure is able to identify ^{22}Na, ^{60}Co, ^{137}Cs, the internal activity peak of $LaBr_3$(Ce) and the natural background; if we launch the program on a $LaBr_3$(Ce) spectrum of the ^{60}Co source (see Fig. 5.5) we correctly obtain:

```
Found 3 peaks:

1) M: 1168.402222 S: 15.087454 R: 2.886032% R(E): 2.217548%
```

```
2) M: 1326.356567 S: 14.017448 R: 2.362034% R(E): 2.081321%

3) M: 1458.046875 S: 21.800505 R: 3.341739% R(E): 1.985105%

Nearest peak to 1173 is 1168 with sigma 15.087454
Nearest peak to 1332 is 1326 with sigma 14.017448
*** Source: 60Co        Matches: 2/2        S-Index: 0.353671

Nearest peak to 1460 is 1458 with sigma 21.800505
*** Source: K/LaBr      Matches: 1/1        S-Index: 0.089591
```

5.6.2 Test with SMANDRA detectors

In the final release of the program, the presence of a gamma alarm generated from NaI(Tl) and $LaBr_3$(Ce) is supposed to start another acquisition, lasting 1 or 2 minutes (as requested from IEC standard) for the automatic identification of the radioisotope.

A first series of tests have made in the above mentioned geometrical conditions (^{60}Co source at 271 cm and ^{241}Am at 80 cm) and also using a 400 kBq ^{137}Cs sourced placed at 271 cm.

The procedure was the following: we acquired 5 spectra for every source and 5 background spectra, every run being 1 minute long. Automatic software performed the subtraction of the n-th background from the n-th spectrum. The 15 background-subtracted spectra (5 per source) are automatically processed with the three steps below:

a) energy calibration,

b) subtraction of the continous part of the spectrum,

c) peak search and gaussian fit.

The result is a list of peaks identified by energy, integral and resolution. The resolution information is used to reject possible false-identification of the algorithm (structures clearly too large to correspond to a radioactive decay). Details on the procedure are in Section 5.6.1.

Figures 5.6, 5.7 and 5.8 show example of automatic peak identification on spectrum taken with NaI(Tl) and Cs, Co, Am sources. Red triangles mark identified peaks. We note that in case of Cs and Am the program identifies only characteristic transition, while in the Co spectrum also other structures are marked; considering that resolution is larger and integral smaller than “normal” peaks, they can easily be identified and rejected.

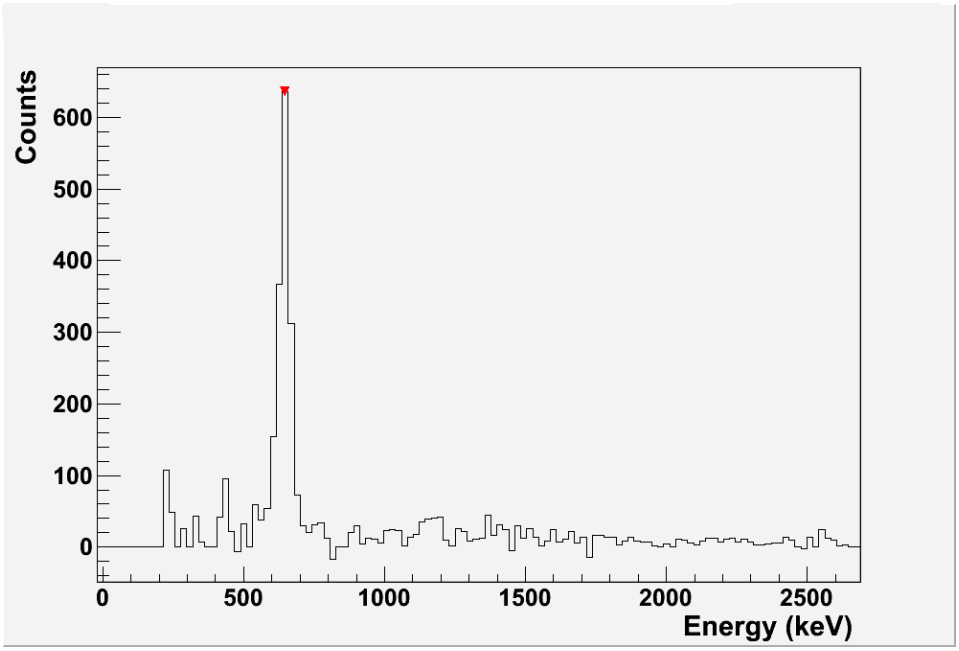

Figure 5.6: ^{137}Cs spectrum after the automatic analysis

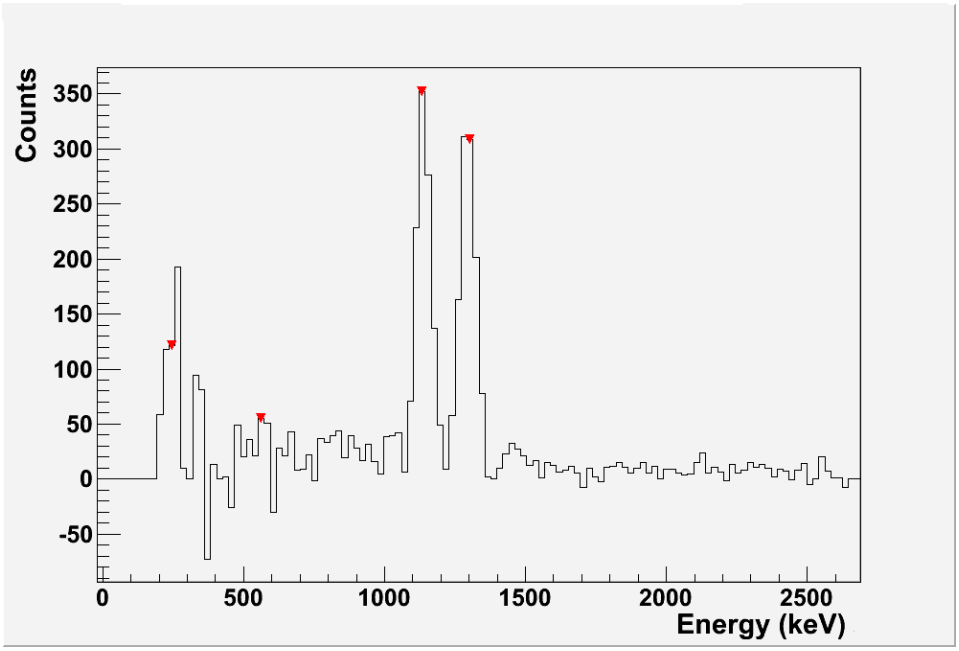

Figure 5.7: ^{60}Co spectrum after the automatic analysis

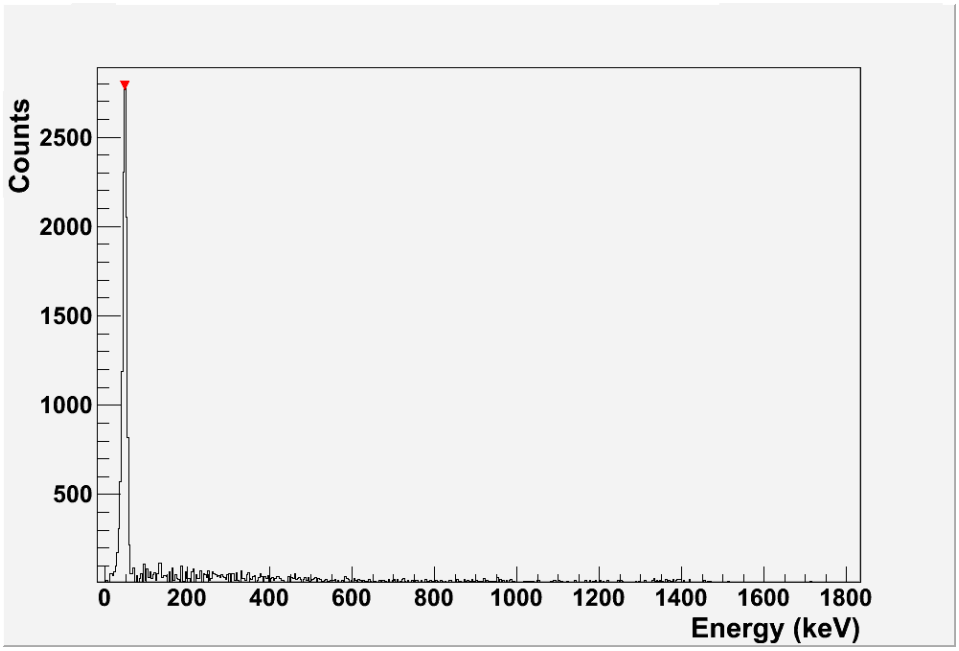

Figure 5.8: ^{241}Am spectrum after the automatic analysis

Results are summarized in Table 5.7.

Source	E_γ (keV)	Measured E_γ (keV)	Measured Res (%)
^{241}Am	59	47.23 ± 0.04	24.32 ± 1.05
^{137}Cs	661	648.1 ± 1.4	6.72 ± 0.56
^{60}Co	1170	1144.0 ± 1.8	5.41 ± 0.15
	1330	1299.8 ± 1.4	4.77 ± 0.24

Table 5.7: Results of the source identification tests

Reported uncertainties refer to the deviation from the average evaluated for the 5 measurements. Apart from systematic shifts due to calibration, we see that the precision in determining the centroids is very good, while the resolution is affected from a typical error of 5%. These two parameters determine uncertainty of the integral, which is always under 7% (worst case with Cesium source).

As a conclusion, it seem that system performances did reach the targets. Using NaI(Tl), that is bigger than $LaBr_3$(Ce) and has a greater efficiency, SMANDRA can generate an alarm at greater distances (or lower doses) as requested by the IEC standard, and can also identify the sources with a 1 minute acquisition.

Chapter 6

Measurement at JRC (Ispra)

The results reported in this Chapter have been obtained by using calibration gamma ray-sources and neutron sources (^{252}Cf and AmBe) located inside the INFN-LNL whereas Special Nuclear Material has been made available by the PERLA Laboratory at JRC Ispra where the tests were performed.

In Table 6.1 we report the SNM samples used in our tests.

SNM	Code	Weight (g)	Enrichment
Plutonium	CBNM61	6.6	62,5% in ^{239}Pu
	CBNM70	6.7	73,3% in ^{239}Pu
	CBNM84	6.7	84,4% in ^{239}Pu
	CBNM93	6.6	93,4% in ^{239}Pu
MOX	ENEA01	168.1 Pu	66,4% in ^{239}Pu
Uranium	LU102	388	1,0% in ^{235}U
	UP899S	46,4	89,9% in ^{235}U
	LU25	2500	2,5% in ^{235}U
	LU44	2500	4,4 in ^{235}U

Table 6.1: Special Nuclear Material samples used at the PERLA laboratory.

It is interesting to note that the 6 g Pu samples CBNMxx are expected to emit neutrons at the rate of 0.5-3 kcps depending on the isotopic composition, the estimate of the nominal gamma emission being more difficult due to the absorption of the metallic enclosure of the sample.

6.1 Detection in Passive Mode

As a first attempt, the detection of SNM samples was explored in passive mode using the SMANDRA multi-detector box. The sensitivity of the system in detecting weak gamma ray and neutron sources, as obtained in our Applied Physics Laboratory at LNL, is reported in Sec. 5. The detection protocol for the SNM test is the following:

a) for each measurement a background run was first performed in order to define the alarm threshold for neutrons in the NE-213 detector, as well as for gamma

ray in the high efficiency NaI(Tl) scintillator. Alarm thresholds correspond to 3 seconds measuring time;

b) all SNM samples were placed in front of the detector box, shielded by 6 mm of iron. The distances were adjusted so that the various sources would deliver a dose of 0.5 μSv/h at the surface of the detector box. This condition was defined for each sample by use of a Victoreen Model 451P ionization chamber;

c) for all samples, 5 or 10 minutes acquisitions were performed. Events were grouped offline into 3 s measurements using the time stamps. This process was done in order to verify the detection probability (PD) at a given confidence level (CL). Test were performed at PD= 90%, CF= 95% according to the prescriptions of IEC standards. Specifically, this protocol was defined in accordance with the prescriptions for hand-held radiometric system reported in [79].

6.1.1 Small Pu samples

The small 6g Pu samples (CBNMxx) produced alarms both for neutrons and for gamma rays satisfying the required PD. Typical count rates with the sample sources resulted several times higher than the laboratory background. The measured neutron yield is reported in Fig. 6.1 in terms of counts per gram of plutonium sample in a minute measurement as a function of ^{239}Pu isotopic abundance (blue squares). The red line is the expected yield assuming a detection efficiency of about 20% for the neutron detector after energy windowing.

Gamma rays spectra from the Pu samples have been studied making use of the superior energy resolution of the $LaBr_3$(Ce)scintillator, needed to disentangle the complex spectra [80]. Typical results for a 61% enrichment sample are presented in Fig. 6.2 where the upper panel shows the raw (energy uncalibrated) spectrum for a 10 minute acquisition. The high energy structure is due to the internal activation of the $LaBr_3$(Ce) scintillator (1440-1470 keV [8]). Our software produces automatically the calibrated spectrum, subtracting the continuous part of the energy distribution and producing the spectrum in the lower panel. It is also possible to subtract the background due to the ambient as well as the internal $LaBr_3$(Ce) radioactivity. Few gamma ray transitions are visible in this spectrum: the lines at E_γ = 373, 414 and 451 keV that can be attributed to the ^{239}Pu decay and lines at E_γ = 662 and 772 keV deriving from the ^{241}Am decay. Moreover, the E_γ = 208 keV line is due to the ^{241}Am nucleus as well as to the ^{237}U, another daughter nucleus often in secular equilibrium with ^{241}Pu. It is also interesting to note that ^{239}Pu has also a transition at E_γ = 203 keV that can not be resolved with the present system.

The same transitions are found with Pu samples with different isotopics but the peak ratios are different according with the isotopic composition of the sample.

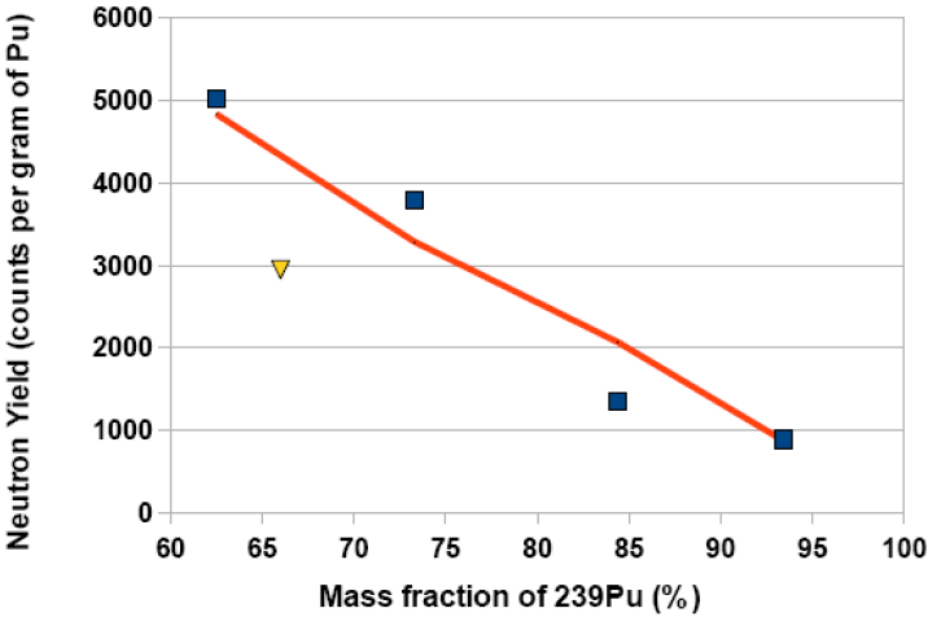

Figure 6.1: Measured neutron yield for 6 g calibration Pu samples (blu squares) as a function of the sample mass percent of the ^{239}Pu isotope relative to total plutonium. The triangle refers to a very large Pu sample (ENEA01). The red line refers to yield estimate based on the sample isotopic composition.

Such features are reported in Fig. 6.3 in term of yield of the relevant ^{239}Pu lines as a function of the sample composition. Fig. 6.4 displays the ratio between the relevant gamma lines of ^{239}Pu and ^{241}Am as a function of enrichment. Thus, after the simultaneous gamma and neutron alarms, the gamma ray spectra can be used to identify the plutonium sample providing as well some rough information about the isotopic composition, especially in the very high enrichment zone.

6.1.2 MOX sample

Signatures from a larger Pu sample have been studied using the MOX ENEA01. This is particularly interesting because of the large amount of Pu present in the sample (170g) mixed with uranium oxides (1011g) and the presence of a 2.5 cm thick Pb shield around the sealed source container. The sample was positioned in accordance with prescriptions about dose rate as described above. The sample releases a strong neutron signature that alarms the system providing the required DP. However, the normalized neutron yield is lower respect to the ones from 6g samples, as reported in Fig. 6.1 due to the self absorption inside the material.

The gamma ray emission is also very strong even after the lead shield. The collected gamma ray spectrum displays clearly the expected ^{239}Pu - ^{241}Am gamma lines as demonstrated in Fig. 6.5. Consequently, it seems that large Pu samples could be easily identified also in presence of lead shielding.

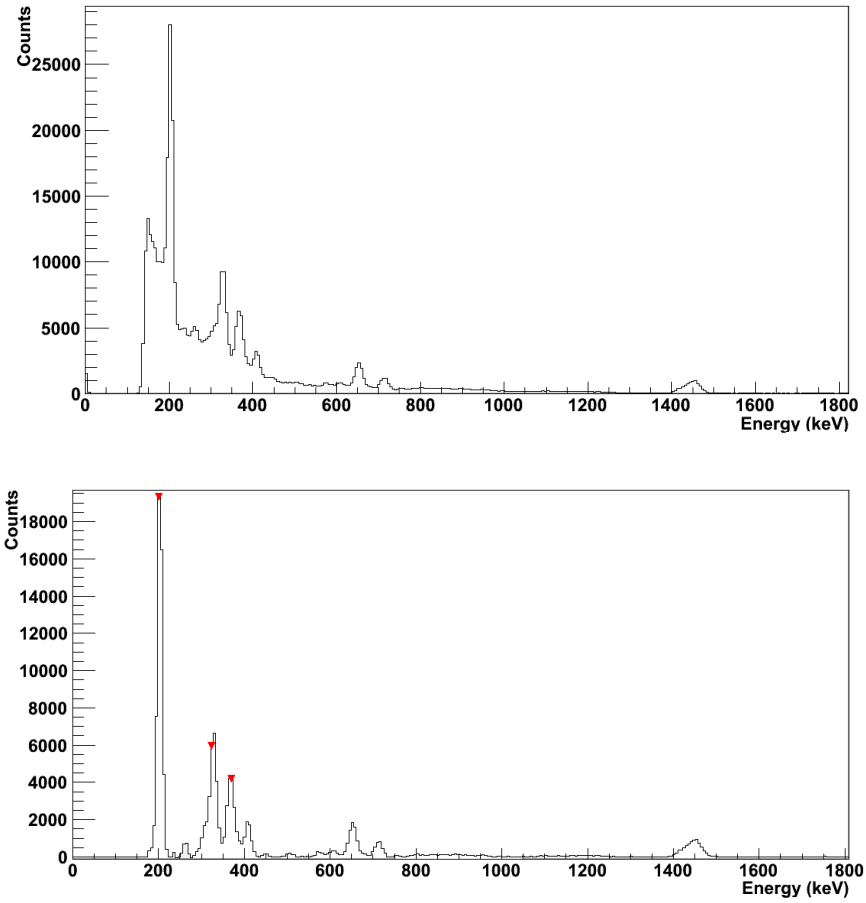

Figure 6.2: Gamma ray spectrum of aCBNM61 at different stages of the data processing.

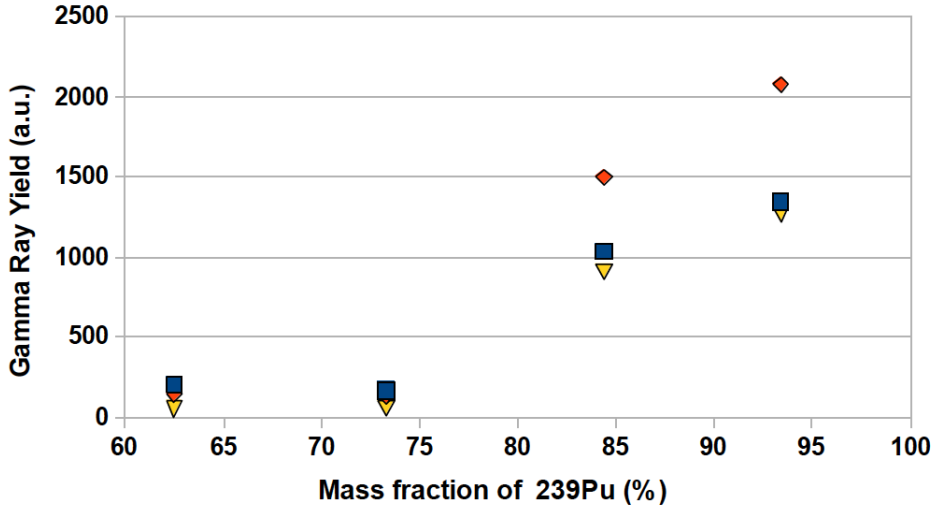

Figure 6.3: Yield of the relevant ^{239}Pu gamma transitions as a function of the sample composition (red diamond $E_\gamma = 375$ keV; blu square $E_\gamma = 332$ keV; yellow triangle $E_\gamma = 413$ keV).

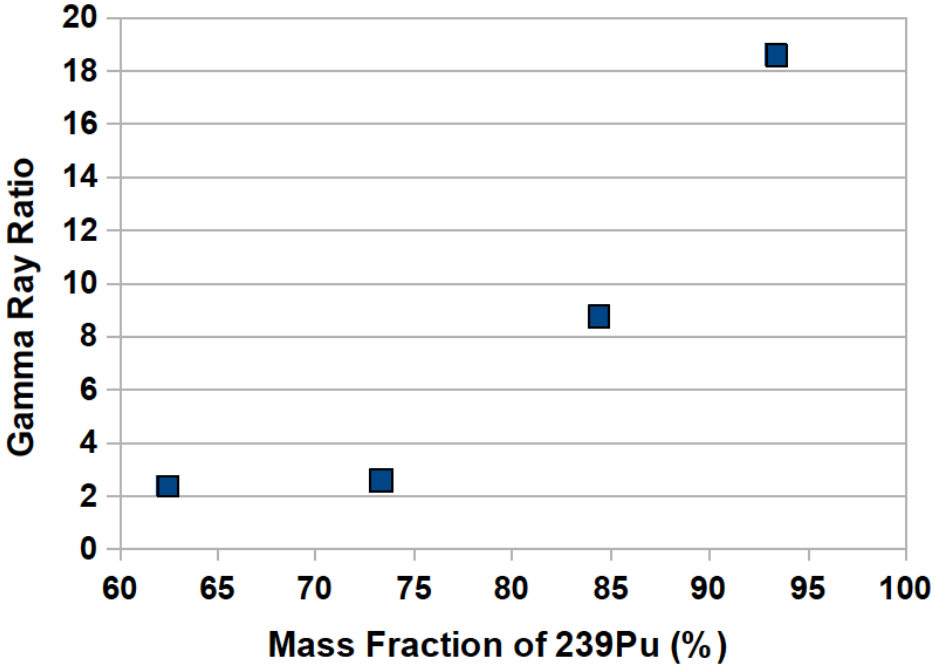

Figure 6.4: Ratio between the relevant ^{239}Pu (E_γ = 375 keV) and ^{241}Am (E_γ = 375 keV) gamma rays as a function of the enrichment of the sample.

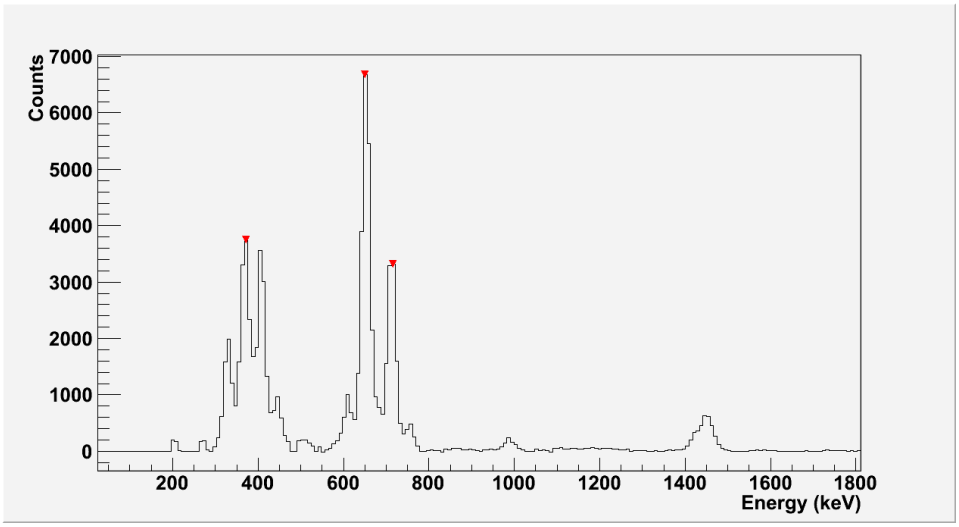

Figure 6.5: Gamma ray spectrum from the ENEA01 MOX sample.

6.1.3 Uranium samples

Uranium samples LU102 and UP899S were used to investigate the response of the system operated in passive mode to SNM with different neutron/gamma ratios. The intensity of gamma ray emission from the sample is sufficient to yield an alarm, whereas neutron emission resulted to be only about twice the laboratory background. Consequently long measuring times are required in order to get a neutron alarm with the required confidence level. As far as the gamma ray signatures, measured spectra are reported in Fig. 6.6. In the high enriched sample (UP899S) the $E_\gamma = 186$ keV transition in ^{235}U is evident, whereas for the low enrichment sample LU102 the two transitions of ^{238}U at $E_\gamma = 767$ and 1001 keV are clear.

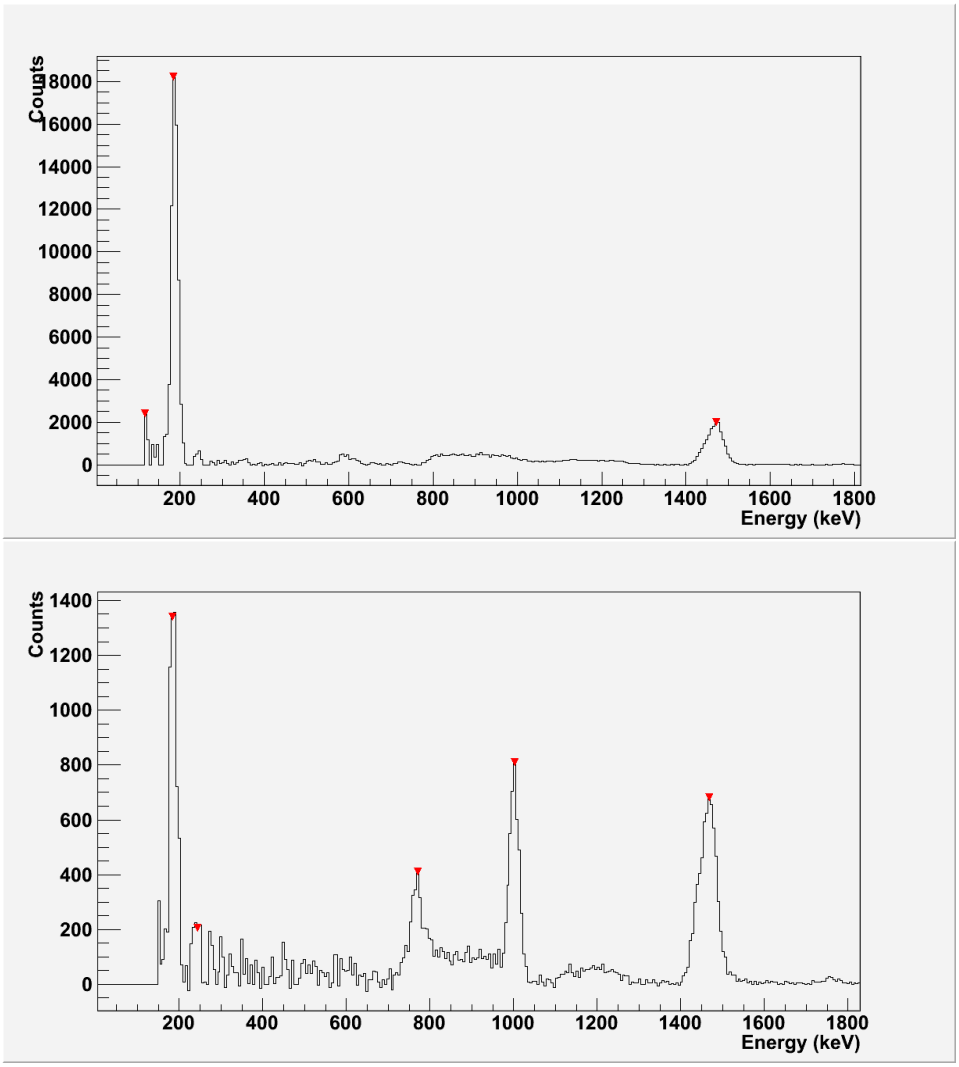

Figure 6.6: Gamma ray spectra from UP899S (top) and LU102 (bottom) samples.

6.1.4 Behaviour with shielding materials

As shown in this Section, the Pu samples produce neutron as well as gamma ray alarms in the detection system when the dose delivered at the detector surface is 0.5 μSv/h. In the same condition the U samples produce a clear gamma ray alarm but the neutron emission being too weak. In both cases the $LaBr_3(Ce)$ gamma ray spectra provide hints on the isotopic composition of the sample. It is worth considering how this information is modified by the presence of shielding materials.

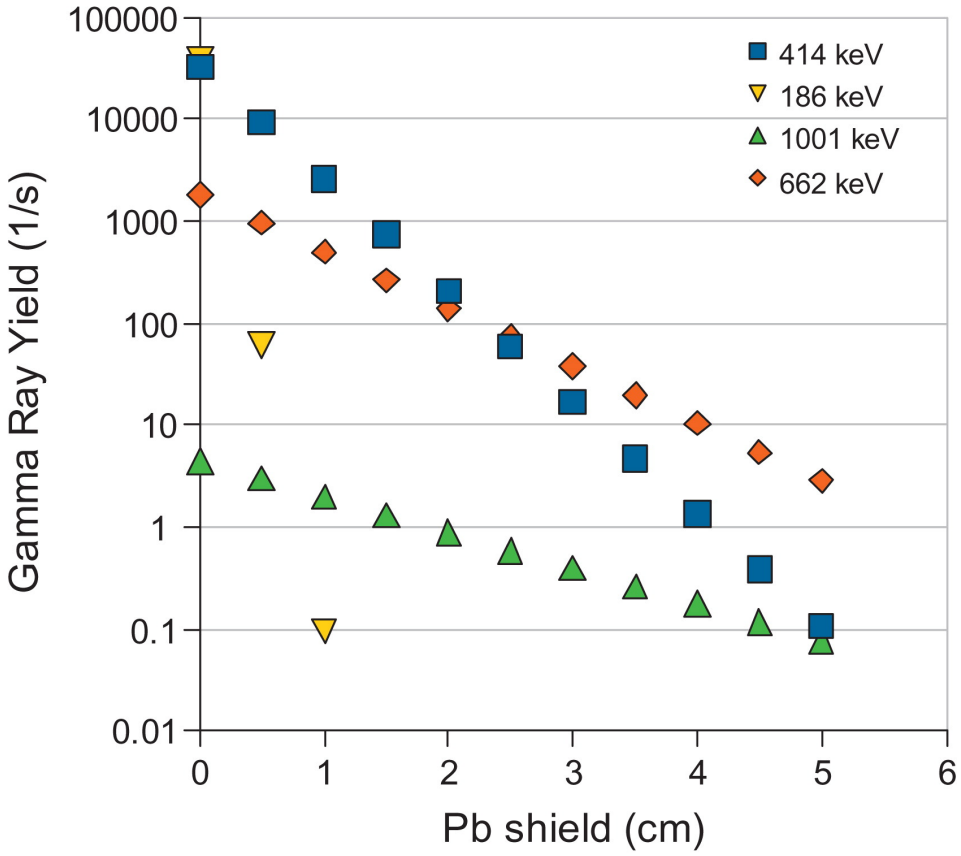

Figure 6.7: Gamma ray yield from 1 g weapon grade plutonium and uranium samples as a function of the thickness of lead shield (diamond ^{241}Am $E_\gamma = 662$ keV; square ^{239}pu $E_\gamma = 414$ keV; yellow triangle ^{235}U $E_\gamma = 186$ keV; green triangle ^{238}U $E_\gamma = 1001$ keV).

The effect of different materials on the neutron emission of a source hidden in a cargo container is discussed in detail in [12] and we refer to this work for the attenuation of the neutron signal of a Pu sample. However, it is interesting to consider in more detail the γ-ray signal from the samples studied in this work when shielded with heavy metals. This is shown in Fig. 6.7 where the effect of the attenuation due to lead shielding is detailed for the characteristic gamma rays emitted from a 1 g source of weapon grade plutonium (93% ^{293}Pu) and uranium (93% ^{235}Pu). In case of the WGPu, the ^{239}Pu and the ^{241}Am transitions ($E_\gamma = 414$ keV and $E_\gamma = 662$ keV) still have a yield of about 100 Hz after 2.5 cm of shielding

making the detection possible at close contact. However, the ratio between the ^{239}Pu / ^{241}Am transition is modified from $R = 18$ with no shield to $R = 0.8$ with 2.5 cm lead providing a false hint on the isotopic composition of the sample as shown in Fig. 6.4. Moreover, the photon signature from highly enriched uranium is extremely weak even after 1 cm lead due to the low energy of the ^{235}U transition and the intrinsic low yield of the ^{238}U one. Also in this case the lead shield causes a strong change in the isotopic composition derived from the γ-ray spectrum.

Summarising, the detection of uranium samples in passive mode seems to be difficult in case the sample is shielded with high Z material that will significantly attenuate the gamma signature from the source. Shielding the uranium with low Z materials seems to be superfluous because only the neutron signal being weak. Detection of uranium with active interrogation is the subject of the next section.

6.2 Active Interrogations

In active interrogations the associated particle detector signal is also processed in the V1720 card. The associated particle detector covers solid angle fraction of about $1 \cdot 10^{-4}$ of 4π so that a rate of 10 kHz is expected in the operation of the neutron generator at a total intensity of 10^7 neutron/s. The limit is imposed by the laboratory license.

To obtain the neutron beam spatial distribution, a vertical and horizontal scan was performed to experimentally determine the size and central position of neutron beam. A liquid scintillator EJ301 2"x2" was used in coincidence with YAP detector. The profile of the beam is shown in Figure 6.8

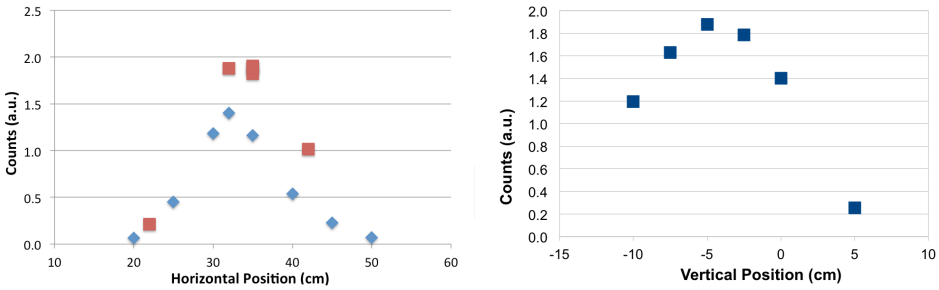

Figure 6.8: Horizontal optimization (left panel): blu squares represent the first scan, orange diamonds represent the second scan after vertical optimizazion. Right panel: vertical optimization.

In the above conditions, the spot of the tagged neutron beam produced by the TPA17 generator at the object position, located about 30 cm from the detector box surface, has been measured to be about 15 cm [FWHM].

In the active mode operations we stored directly all single events processed by the V1720 card running at a typical total rate of about 50 kHz, writing the interesting

Material	Phys. St.	ρ (g/cm^3)	H(%)	C(%)	N(%)	O(%)
Nitroglicerine	Liquid	1.6	2.2	15.9	18.5	63.4
Ammonium Nitrate	Solid	1.7	5.0	0.0	35.0	58.0
Black Powder	Solid	1.7-1.95	0.5	11.0	10.5	36.0
Nitrocellulose	Solid	1.5-1.7	2.4	24.3	14.1	59.2
PETN	Solid	1.76	2.4	19.0	17.7	60.7
TNT	Solid	1.5-1.6	2.2	37.0	18.5	42.3
C-3	Solid	1.58-1.62	2.9	22.8	32.8	41.6
C-4	Solid	1.64-1.66	3.6	21.9	34.5	40.2
Comp B	Solid	1.71	2.7	24.4	30.5	42.7
Tetryl	Solid	1.57-1.71	1.8	29.3	24.4	44.6
Dynamite	Solid	1.25	4.0	14.0	15-20	59
Trinitroanisole	Solid	1.41	2.1	34.6	17.3	46.1
Trinitroxilene	Solid	1.60	3.5	42.4	16.5	37.6

Table 6.2: Chemical composition of most used explosives

part of the digitized signals. Off-line software analyzes the event files reconstructing the coincidence events and the time correlation between detectors. The time interval from the start time of the digitalization and a given fraction of the front part of the signal is determined for each detector, correcting for the amplitude effect. This type of analysis yields a time resolution better than the intrinsic limit of the V1720 sampling bin (4 ns). Laboratory tests using gamma-gamma coincidences with a ^{22}Na source and a fast plastic as trigger detectors are as follows (when the lower threshold discrimination is set at about 500 keV):

- δt = 1.15 ns [FWHM] for $LaBr_3$(Ce),
- δt = 5.4 ns [FWHM] for NaI(Tl).

In the active interrogation tests the two large U samples LU25 and LU44 were employed together with a 16.7 kg iron cylinder, a 6.7 kg lead bricks and a sample of about 10 kg organic material composed by 50% of Plexiglas and 50% of melamine powder. Typical interrogation run lasted for 10 minutes. In some cases few interrogation runs were performed for the same sample.

6.2.1 Chemical Sample

The use of SMANDRA for non-destructive analysis with active interrogations is aimed primarily to the research of hazardous and / or illegal material. In most cases these dangeours substances are composed by organic compounds with different chemical composition. As an example we report in table 6.2 the chemical composition of some explosives.

From the reported data, it is clear that a non-destructive analysis system must be able to determinate the concentration of carbon, oxygen, nitrogen and possibly

Material	Weight	Dimension
Graphite (C)	3 kg	Carton box (22.5 x 17 x 15.5 cm^3)
Melamine ($C_3H_6N_6$)	5 kg	Two samples of 2.5 (11.5 x 11,5 x 20 cm^3)
Boric acid (H_3BO_3)	4 kg	Four samples of 1 kg (Cylinder: D 9.5 cm, H 17.5 cm)
Plexiglas $(C_5O_2H_8)_n$	5.2 kg	Two plates of 2.6 kg (30 x 16 x 5 cm^3)

Table 6.3: Principal characteristic of the samples used during JRC test

hydrogen inside the sample. To this aim it is necessary the determination of the characteristic γ-ray emitted by the organic nuclei under bombardment of 14MeV neutrons. A compete review of γ-ray spectra obtained with NaI(Tl) scintillators from most relevant organic nuclei can be found in [81].

In order to demonstrate the ability of SMANDRA to identify the presence of nuclei C, N, O, some samples were prepared and used into JRC Laboratory where the introduction of liquid substances is explicitly forbidden. The characteristics of the samples used are shown in table 6.3:

The first measurement was carried out with the simplest sample: graphite. In this case it was recorded only the time-stamp of the events and this limits the time resolution of the system. The results for a 15 minutes run are shown in Fig. 6.9 for the detector $LaBr_3$(Ce) and in Fig. 6.10 for NaI(Tl).

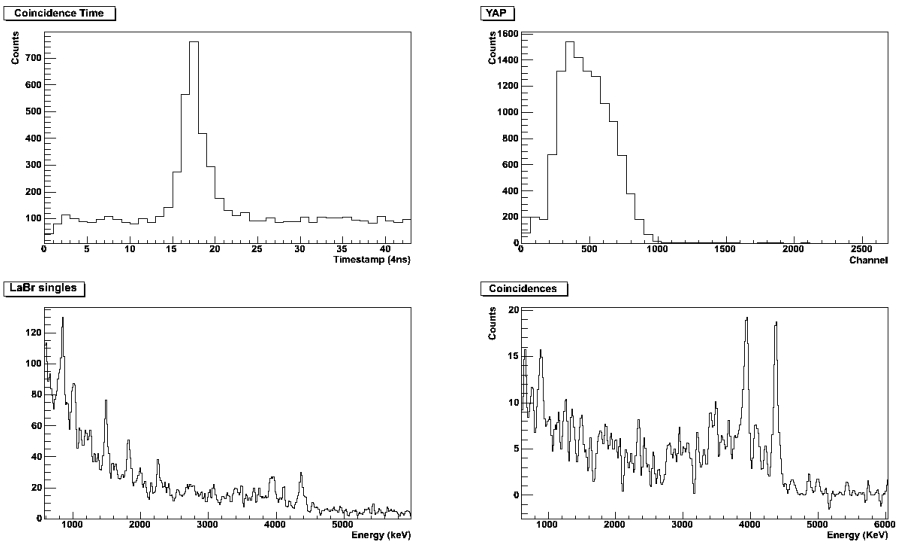

Figure 6.9: Experimental results obtained with graphite for $LaBr_3$(Ce) detector. In the upper left panel coincidences reconstructed using the time-stamp. In the top right panel energy spectra for the associated particle detector YAP:Ce. In the bottom left panel total energy spectra for $LaBr_3$(Ce). In the right panel energy histogram for events in coincidence between $LaBr_3$(Ce) and YAP:Ce.

The coincidente γ-ray spectrum (down-right panel in fig 6.9) clearly shows the full-energy peak at 4.4 MeV and the single escape peak at 3.9 MeV due to the first excited level of ^{12}C. From Fig. 6.9 and 6.10 it is possible to determine the time and energy resolution of the system. The time resolution for $LaBr_3$(Ce) is about 9 ns

[FWHM] (about two bins in time stamp) and the energy resolution is 2% [FWHM] at 4.4 MeV. For NaI(Tl) we have a time resolution of 30 ns [FWHM] while the energy resolution is 5.8% [FWHM] at 4.4 MeV. However, the presence of the carbon is uniquely determined by the transitions at 4.4 MeV and 3.9 MeV. The yield of the transition can provide an estimate of the amount of carbon in the voxels of the sample using empirical calibration.

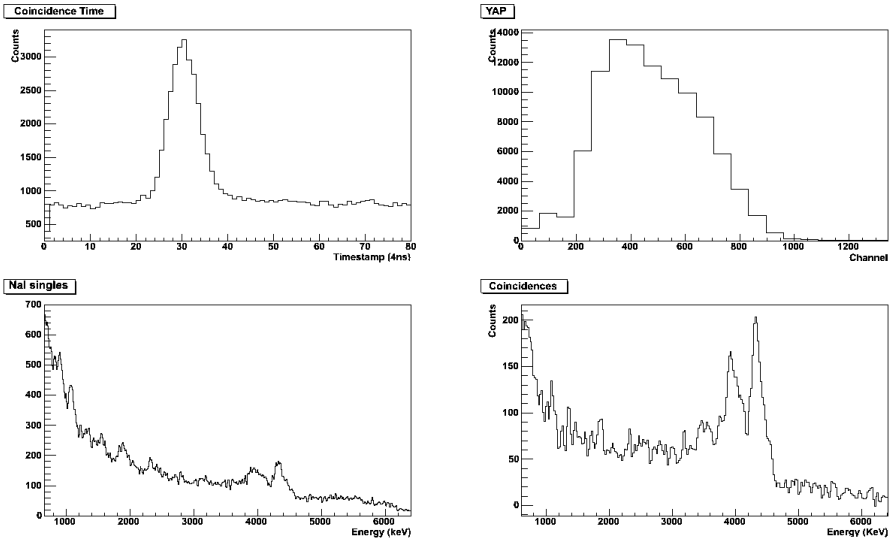

Figure 6.10: Experimental results obtained with graphite for NaI(Tl) detector. In the upper left panel coincidences reconstructed using the time-stamp. In the top right panel energy spectra for the associated particle detector YAP:Ce. In the bottom left panel total energy spectra for NaI(Tl). In the right panel energy histogram for events in coincidence between NaI(Tl) and YAP:Ce.

For the other irradiated sample we report only the spectra for $LaBr_3(Ce)$ scintillator that, thanks to the higher energy resolution, allows us to clearly identify the transitions present in the coincidence energy spectra. Fig 6.11 shows the result of melamine's irradiation. In this case it is evident the presence of carbon and nitrogen. In Fig. 6.12 is shown a spectrum obtained from a composite sample of plexiglass and melamine; where the presence of oxygen transitions it is also detected.

These tests confirm the possible of verify the presence of various elements C, N, O looking at the γ-transitions induced by 14 MeV neutrons. Regarding the presence of hydrogen the only way to reveal it, is to search the 2.2 MeV transition due to thermal neutron capture. Since the thermalization of neutrons in the sample is a process of a few tens of microseconds, the signal is distributed between the uncorrelated events in the time of flight spectra. The result of selecting a set of such events is reported in Fig. 6.13 that shows the 2.2 MeV transitions and then the possibility to reconstruct the presence of hydrogen in the sample.

Finally, we perform further irradiation with typical shielding material, iron and lead. The situation in irradiating iron and lead is shown in Fig. 6.14. Moreover, the

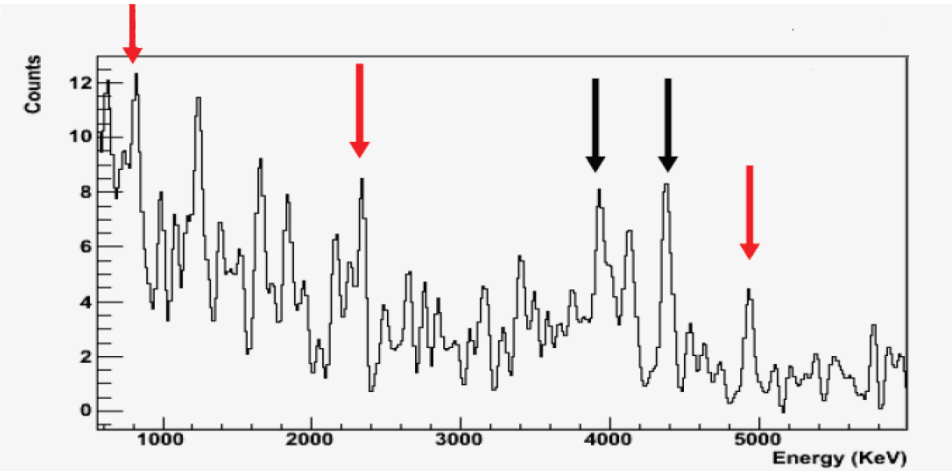

Figure 6.11: Experimental results obtained with melamine sample for $LaBr_3(Ce)$ detector. The black arrows indicate the position of the Carbon peaks (4.4 and 3.9 MeV), while the red arrows indicate the transitions attributed to nitrogen (5.1 MeV, 2.3 MeV, 0.7 MeV).

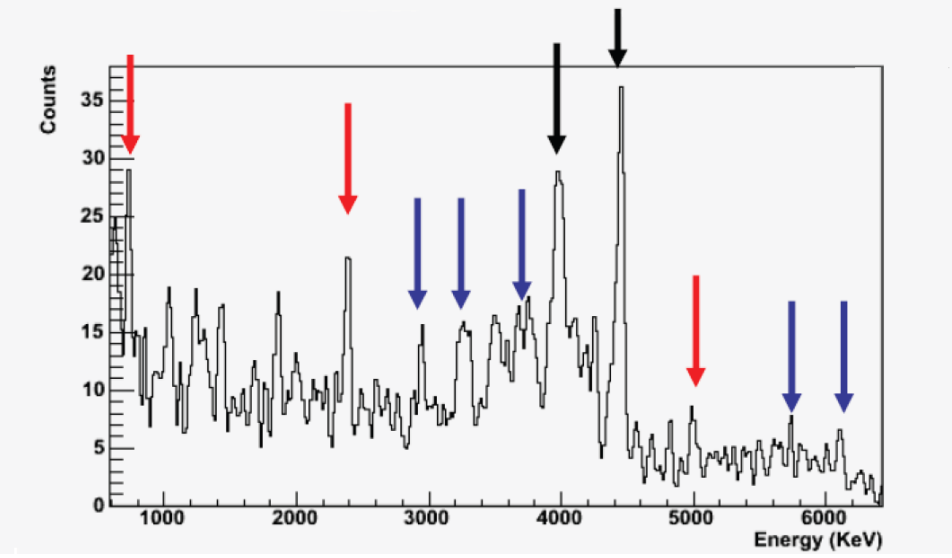

Figure 6.12: Experimental results for $LaBr_3(Ce)$ detector obtained with a mixed sample of plexiglass and melamine. The black arrows indicate the carbon signature (4.4 and 3.9 MeV), the red arrows indicate the nitrogen transitions (5.1 MeV, 2.3 MeV, 0.7 MeV) and the blue arrows indicate the structures due to oxygen (6.1 and 5.7 MeV, 3.7, 3.1 and 2.7 MeV).

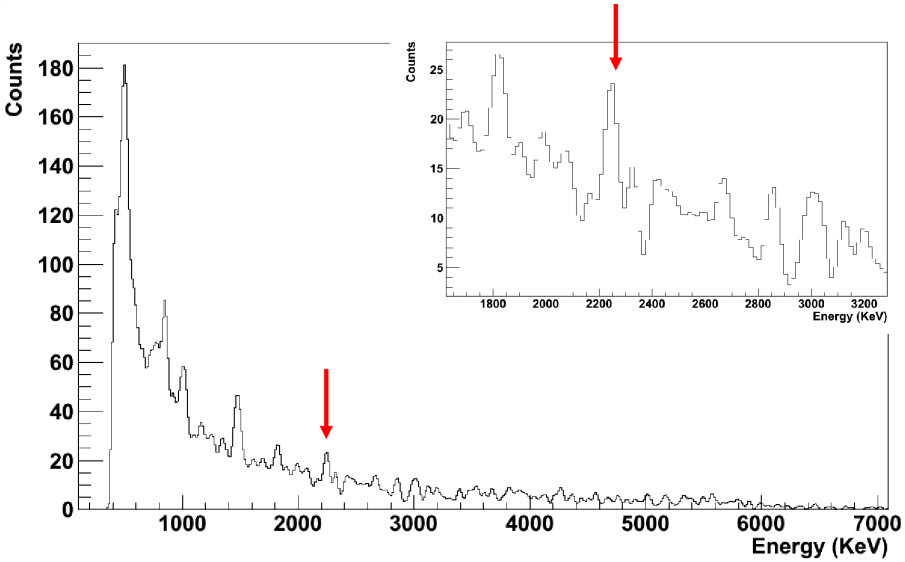

Figure 6.13: Experimental results for $LaBr_3(Ce)$ detector obtained with a mixed sample of plexiglass and melamine. The selected events are not correlated in the time of flight spectra. The transition at 2.2 MeV is due to neutron capture in hydrogen

coincident spectra of iron exhibits the well known gamma ray transitions of inelastic excitation ($E_\gamma = 0.847$ and 1.238 MeV) that can be used to identify easily this type of materials [81]. The $LaBr_3(Ce)$ coincident spectrum of the lead sample shows some structures that can be attributed to transitions in Pb isotopes as the well known $E_\gamma = 2.61$ MeV transition in ^{208}Pb. In this case the low statistics of the structure implies a long measurement to have a direct identification of lead.

6.2.2 Special Nuclear Material

Typical results for U samples obtained in the interrogation with fast neutron are reported in Fig. 6.15 for the $LaBr_3(Ce)$ scintillator in coincidence with the associated alpha particle detector.

The spectrum of the alpha particle singles detected by the YAP:Ce scintillator is reported in the upper right panel, while the inclusive gamma ray spectrum from the $LaBr_3(Ce)$ is in the lower left panel, and shows the well known patter of the emission from ^{238}U at $E_\gamma = 767$ and 1001 keV. The time distribution of the coincidences (upper-left panel) exhibits a double peaked structure due to the detection in the $LaBr_3(Ce)$ of gamma rays and neutrons from the irradiated sample. Finally the energy distribution of the gamma ray in prompt coincidence mode shows no relevant structures that can be easily used to identify directly and in a efficient way the uranium nuclei.

However the coincident discrete gamma ray spectra alone seems to be hardly usable to distinguish between Pb and U when the gamma ray signature due to the radioactive decay of uranium nuclei is not visible. Consequently we have explored

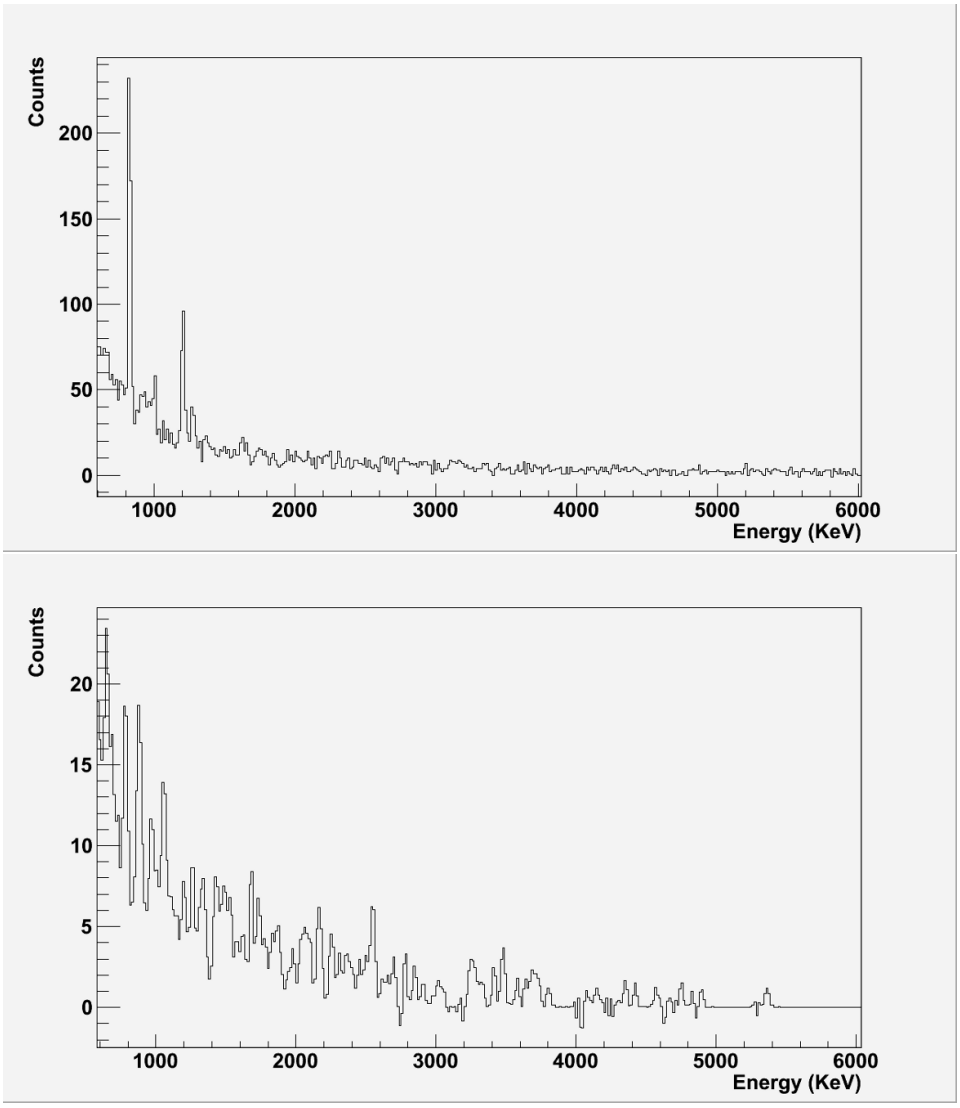

Figure 6.14: $LaBr_3(Ce)$ gamma ray spectra in coincidence with the associated alpha particles iron (top) and lead (bottom) samples.

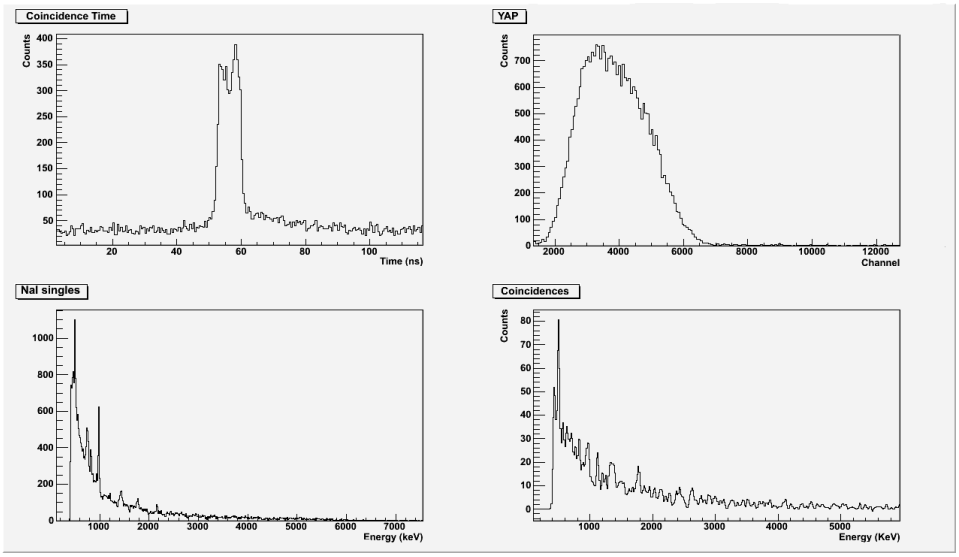

Figure 6.15: $LaBr_3(Ce)$ coincidences with the associated alpha particle detector for the LU44 sample.

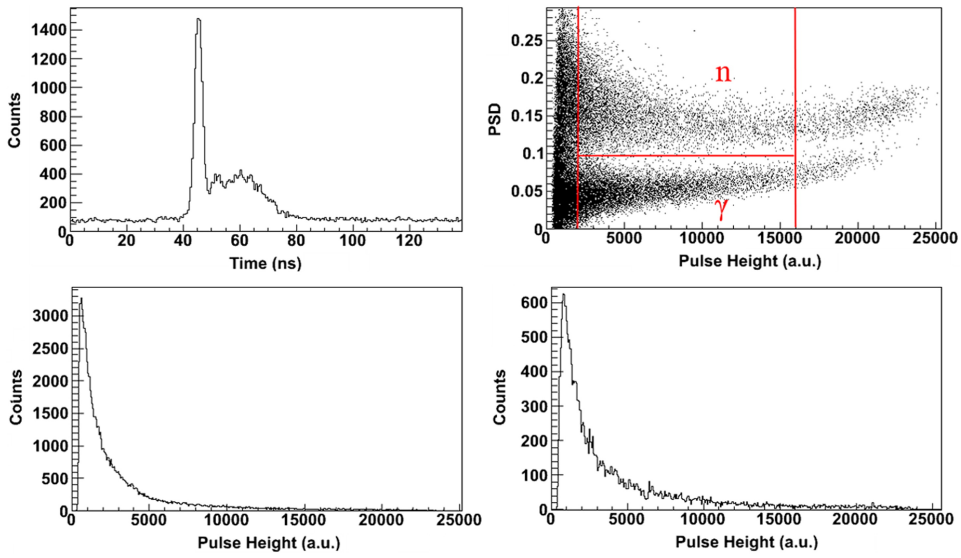

Figure 6.16: Response of NE-213 detector to LU44 emission. For details on the panels see the text. In the upper right panel, the Pulse Shape Discrimination (PSD) parameter is reported versus the scintillator pulse height. In this case PSD is the ratio between the delayed light component and the total light, computed using the two integration gates provided directly by the V1720 FPGA. Lines in the panel define the areas for accepted gamma ray and neutron events.

other signatures collected by our detection system.

The time spectrum of NE-213 shows for each sample a very narrow peak due to prompt coincidences mainly due to neutron induced gamma rays, well separated by a second larger peak due to secondary neutrons produced by the 14 MeV neutron beam, as shown in Fig. 6.16 in case of irradiation of the LU44 sample. Such secondary neutrons are associated to fission (n,f) as well as (n,xn) reactions. The pulse height distribution both in single and coincident mode does not provide useful information whereas the pulse-shape discrimination is used to discriminate gamma rays and neutrons in addition to the time of flight information.

Consequently the number of the detected gamma ray and neutrons is derived directly from the particle discrimination algorithm selecting the two types of event by windowing the time difference between the alpha particle and the liquid scintillator signals. This allows a very good separation between the two types of events.

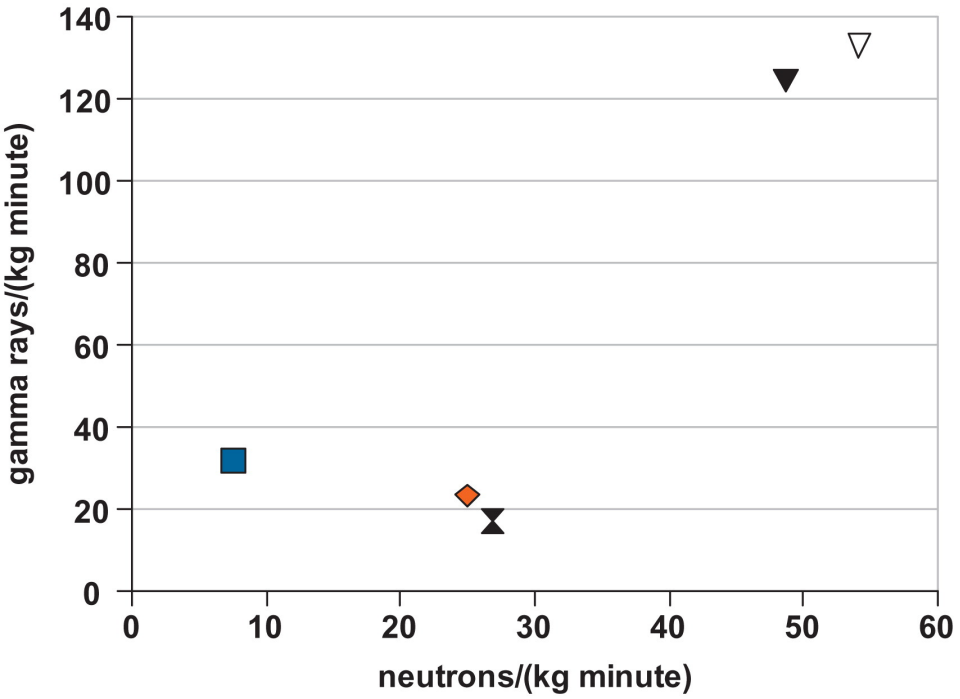

Figure 6.17: Correlation between the normalized neutron and gamma ray yields measured in the NE-213 detector: the square refers to iron, the diamond to lead, the cross to organic and the triangles to uranium (full triangle LU44, empty triangle LU25). Data are relative to 1 kg sample for 1 min irradiation.

The yields obtained in this way, normalized to sample weight, ratio between the sample and the beam area and measuring time, are displayed in Fig. 6.17 in terms of correlation between the number of gamma rays and neutrons detected in the liquid scintillator for each sample. It is interesting to note that the relative number of detected gamma rays and neutrons for each sample is correlated to the relevant neutron and gamma producing cross sections for each elementary sample (see Fig. 6.18). Data reported in Fig. 6.18 have been obtained using directly the

relevant secondary neutron producing cross sections from the ENDF/B-IIV data files [82] properly multiplied for the average number in the exit reaction channel. Gamma ray producing cross section for lead and iron are obtained by summing the production cross section for discrete gamma rays reported in [81]. Uranium data are taken from an old Los Alamos report [83]. In evaluating the gamma ray production cross section the effective threshold in the detector has been considered.

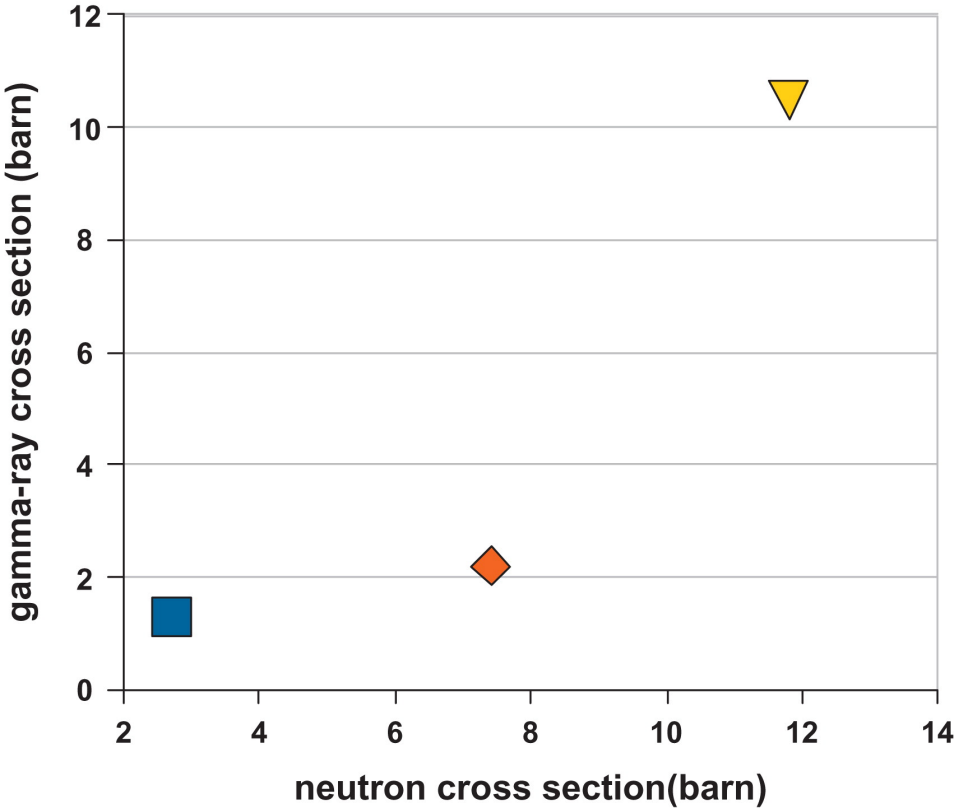

Figure 6.18: Correlation between neutron and gamma ray production cross-section: the square refers to iron, the diamond to lead and the triangle to uranium.

The similarity between the experimental data of Fig. 6.17 and the cross section estimate is striking. The difference between uranium and materials commonly used for shielding is so large that some uncertainties in the cross section estimates seem to be negligible.

As a conclusion, the empirical correlation displayed in Fig. 6.17 shows that, taking into account sample mass and area, it is possible to discriminate uranium from other materials using only the liquid scintillator data. This means that in case of a sealed lead cask that shields the characteristic gamma ray pattern of a uranium sample radioactive decay, the interrogation with tagged neutrons is able to provide evidence for an anomalous emission of gamma rays and neutrons due to the presence of uranium.

In case of the inspection of a suspect volume, as the case of cargo container, the

tagged neutron technique allows to define a voxel inside the total volume. In this case it is questionable that a representation as the one in Fig. 6.17 can be applied to search for uranium. In this case new observables are required to evidence the presence of fissile material. Assuming the case of the irradiation of a given voxel inside a container, the gamma ray spectrum from $LaBr_3$(Ce) easily identifies the presence of organic or iron based material through the well known gamma lines. In this case, in order to discriminate between lead and uranium samples for which no discrete coincident gamma rays in the $LaBr_3$(Ce) detector are usable, a more accurate analysis is needed assuming that the radioactive decay pattern of U nuclei could be shielded and therefore does not provide an alarm.

In order to obtain a discrimination plot, triple coincidences between the associated alpha particle, the liquid scintillator and the large volume NaI(Tl) detector were analyzed. The idea is to verify whether the multiplicity of gamma rays and neutrons emitted in the fission of ^{238}U yields a signature different from the Pb nuclei where neutron multiplication is due only to (n,xn) reactions.

Typical experimental data obtained in reconstructing such triple coincidence events are displayed in Fig. 6.19 for the uranium sample.

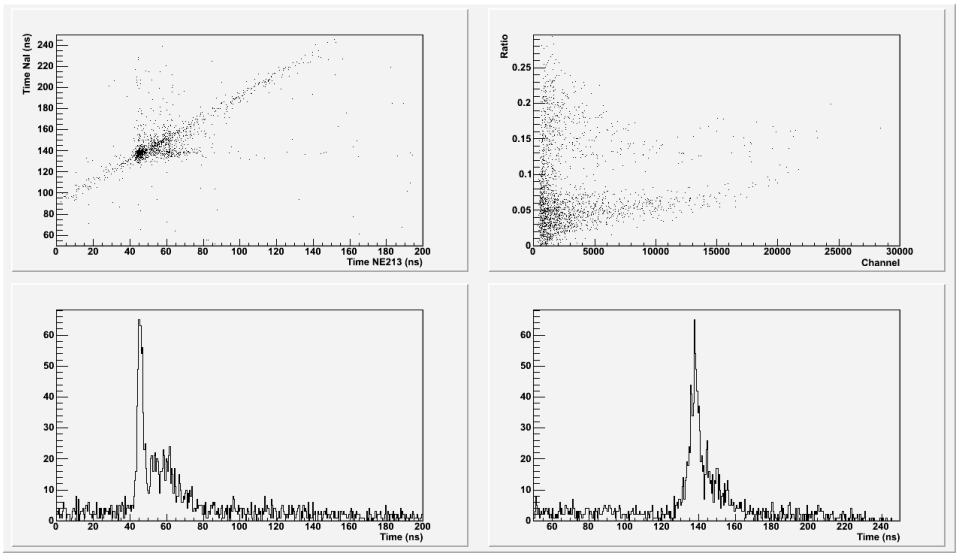

Figure 6.19: Triple coincidence events between the associated alpha particle, the NE-213 and the NaI(Tl) detectors. For details see the text.

The lower panels report the time correlation between alpha particle and NE-213 (left) and alpha particle and NaI(Tl) (right) for all events in triple coincidence. A clear peak is seen, mainly due to gamma rays, followed by a broad distribution due to the secondary neutrons. The superior time resolution of the liquid scintillator allows us to separate more clearly the two components. In the upper right panel is reported the NE-213 neutron-gamma discrimination 2-D plot. In the upper left panel is reported the 2-D time correlation between the coincidence time distributions. This

plot is particularly interesting since it shows clearly the cross talk between the two detectors represented by the diagonal distribution, whereas the different combination between neutrons and gamma rays detected in both detectors are responsible for the main structures in the 2-D plot.

To obtain a parameter which does not need a normalization, the number of triple coincidences (YAP:Ce-NE-213-NaI(Tl)) is divided by the number of double coincidences (YAP:Ce-NE-213). This analysis is repeated twice for gamma rays or neutrons identified in the liquid scintillator. In Fig. 6.20 the data obtained in this way are plotted in a 2-D representation of neutron events against gamma events for the different samples explored in this work. The empirical representation results in the grouping of the sample in three regions. Lead and organic material exhibit a high probability of triple coincidence for gamma ray events (in the NE-213) but low as far as the neutron case. The iron is characterized by a larger probability for neutron respect to previous samples but lower for the gamma rays. The two uranium samples have the largest probability for neutron triple events but an intermediate value for the gamma rays respect previous samples. As a result, clear distinction between uranium and other samples is obtained.

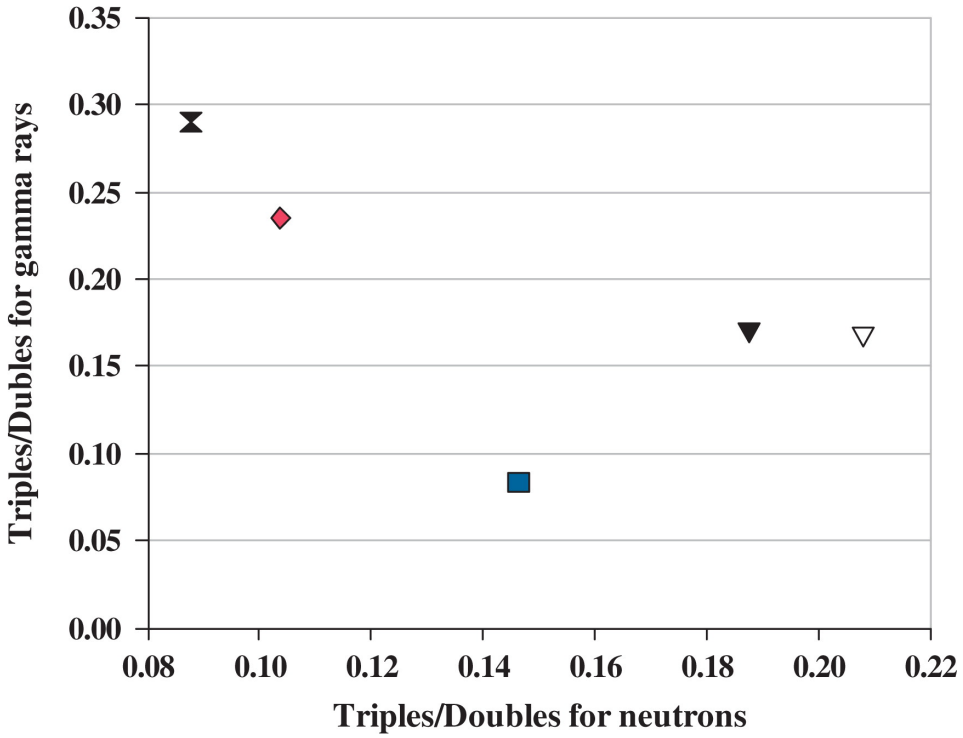

Figure 6.20: Double and triple coincidence results for different samples

It is worth considering that the result in Fig. 6.20 is strongly dependent on the geometry of the present detection system. The role of the large NaI(Tl) consists in a simple counter in coincidence with the liquid scintillator. We compare mainly the probability that a gamma or neutron event identified in the liquid scintillator is

accompanied by an additional gamma-ray in the NaI(Tl). We make this because of the efficiency of the NaI(Tl) for neutrons is supposed to be lower than the one for photons and the threshold used in active interrogation is about 500 keV. From this point of view, the neutron events have a larger probability of being accompanied by a gamma-ray for the uranium. It is cleary correlated to the presence of the fission cross section.

6.2.3 Shielded Special Nuclear Material

More recently we have also studied the effect of the shielding on this type of discrimination by simply using a ^{252}Cf source to produce fission events. Results are reported in Fig. 6.21 and are relative to the unshielded source. It seems that using 1 or 2 cm lead shielding immediately inhibits the detection of γ-ray in the NaI(Tl) detectors thus lowering the triple/double ratio. This means that a shielded fission source will be easily confused with other materials. A second test was performed by replacing the NaI(Tl) with a second liquid scintillator where only neutrons are software selected. In this case, since neutrons are scarcely attenuated by the lead, the triples/double ratio of a fissile source remains close to that of an unshielded source. This evidence will guide us to design a new version of the SMANDRA passive unit able to distinguish fission sources in presence of different shielding.

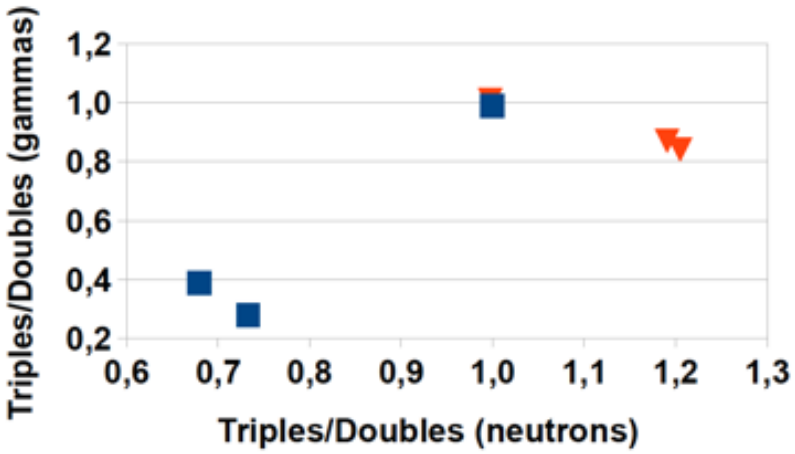

Figure 6.21: Dependence of the Triples/Doubles Ratio for γ-rays and neutrons as a function of the lead shield thickness when the NaI(Tl) detector is used to build the triple events (squares). The triangles refer to a system in which the NaI(Tl) is replaced by a liquid scintillator in which only neutrons are selected. The data without shield are normalized to the (1,1) point whereas the other data points refer to 1 cm and 2 cm lead shields

Chapter 7

Demostration at the La Spezia seaport

In July 2012 the "passive unit" of the SMANDRA system has been employed in a field demonstration at the La Spezia seaport (Italy) together with the other participants to the task SlimChek of the SLIMPORT project.

Figure 7.1: SMANDRA box and small robotic arm, ready for the dimonstration

The passive unit of SMANDRA is shown in Fig. 7.1. Inside the box a 12V - 36 Ah battery is enclosed to ensure sufficient autonomy to all instrumentation (electronic front-end and detectors). A ruggedize laptop is placed above the box and communicates with the operative center throught WIFI connectivity. This allows

the operator to remotely control all the functions of SMANDRA. After our system has detected the presence of a possible threat, other components of the SlimCeck task operated with a robot-system.

The robotic system for the management of dangerous goods in a container consists of two Unmanned Ground Vehicles (UGV). Currently, companies Allen Vanguard and Telerob constitute the major competitors on this market. The most famous products are Defender and Vanguard ROVs for Allen Vanguard and Teodor and Telemax for Telerob. These products are basically remote-control platforms, mainly used in Explosive Ordnance Disposal (EOD) missions. The system used by SlimCheck leads to a significant improvement compared to the present state of the art, providing platforms with sensors for detection of NRBC (Nuclear, radiological, biological and chemical) threats. Another novelty of the robotic system of SlimCheck is the remote-control anthropomorphic arm that uses haptic interface: this is very important because allows the operator to have a feedback that can be decisive in this kind of mission.

The "A" robot provides access to the goods and handles the items for accurate inspection. These operations require a considerable dexterity and a fine control of movements and for these reason the robot is equipped with the anthropomorphic arm with haptic interfac. However, the dangerous goods may be hidden under heavy loads or located behind bulky objects. These problems are overcome by the "M" robot (Handling), a forklift capable of handling large quantities of material for opening the passage to the robot A and enable it to carry out the dangerous object. Both robots are controlled throught WIFI network to which they also communicates in real time the results of NBCR measurements.

The potential applications of this robot system can be extended to all cases concerning safety, since the system in question is able to completely replace the direct presence of an operator. Today the identification of a NRBC threat in a seaport is assigned to the Vigili del Fuoco (Firefighter Corp), which analyze manually the goods with a certain risk for workers. This system can ensures the operator safety, since it replace him in the inspection, and certainly ensure the promptness of intervention, running in a semi-automatic mode for long emergency protocols foreseen in these cases.

The demonstration was directed to the Vigili del Fuoco and was structured in the following way:

- the SMANDRA system was used to determine the position of a weak radioactive source (about 20 kBq) located inside a shipping container and to identify the radioactive material (Fig. 7.2),
- a remote controlled forklift opened the container and entered it to remove some

pallets of materials around the source position (Fig. 7.3),

- the robotic arm A entered the container, catching and transporting the source on a safety dump located outside the container (Fig. 7.4).

Fig 7.5 shows the central station. The demonstration was successfully completed.

Figure 7.2: SMANDRA determines the position of the radioactive source inside the container

Figure 7.3: Remotecontrol forklift opens the container

Figure 7.4: The remote controlled robotic arm entered the container after removals of pallets

Figure 7.5: Operative central where all the components of SlimCeck are remote-controlled

Chapter 8

Possible applications

Liquid scintillators, like NE-213, found a rather marginal use in Homeland Security applications since many operational contexts prohibit these liquids because of their toxicity and flammability. Moreover liquid scintillators detect neutron above a low energy threshold (usually few hundred keV) and exhibit a good gamma-ray efficiency so that such detectors are normally characterized by a modest gamma-ray rejection capability, a property that is required to identify weak neutron source in a strong gamma-ray background [84]. It has been recently pointed out that selecting the fast neutron energy region in the total neutron spectrum optimizes the signal-to-background ratio improving the detection of weak neutron source [10]. New liquid scintillation materials have become recently available as the EJ-309 type [85] (from Eljen Technology) characterized by low toxicity and high flash point (144 °C) compared to the more traditional EJ-301 (flash point 26 °C) equivalent to the well known NE-213. The EJ-309 scintillator has been employed in pure and applied research works confirming a PSD capability well suited to perform neutron spectroscopy [86][87]. The gamma rejection capability of the EJ-309 was the subject of a recent study [88]. In next sections we will study the possible application of liquid scintillator detectors in the field of Homeland Security with respect to neutron detection in an intense gamma-ray background.

8.1 Characterization of new liquid scintillators

The detectors studied in this work consist of 2"x2" liquid scintillator cells coupled to an H1949-51 HAMAMATSU photomultiplier (PMT) through an EJ-560 silicon rubber interface. The PMT anode signals were directly fed into a CAEN V1720 12 bit 250 MS/s Digitizer. The PMTs operated at relatively low voltage (HV=1600 Volt) to avoid saturation effects in digitizing the pulses. The optimization of the DPP parameters has been performed empirically by maximizing the FoM corresponding to different sets of the DPP parameters. It is found that the optimized DPP parameters for the EJ-301 and EJ-309 detectors are identical: 70 and 17 bins

for the Long and Short Gates respectively, 10 bins for the Pre-gate and 4 bins for the Baseline Threshold (each bin is 4 ns wide). With the above parameters, each pulse is characterized by 70 samples and the V1720 Digitizers handles count rate up about 100 kHz without dead time. Finally, the energy calibration of the scintillation light was established by using the procedure described in [10] based on the fit of the experimental pulse shape distribution by using the theoretical Compton scattering distribution with an empirical spreading width to account for the finite detector resolution. Samples of those spectra for a ^{22}Na radioactive source are reported in Fig. 8.1.

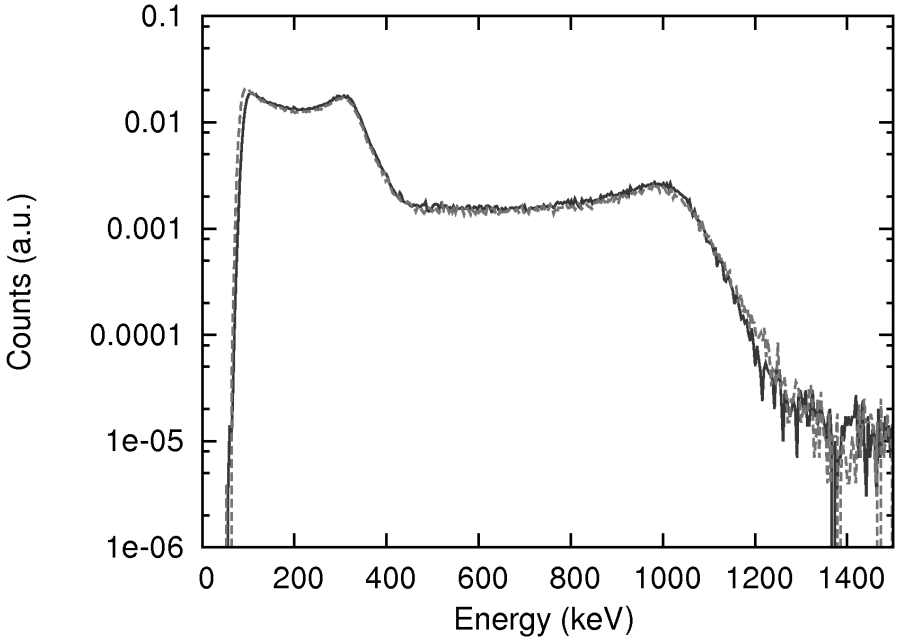

Figure 8.1: Calibrated $^{Na}22$ pulse height distribution for the detectors studied in this work: EJ-301 full line, EJ-309 dashed line

It is clear from Fig. 8.1 that the spectra measured with the two scintillators are very similar. The calibration procedure allows one to obtain an estimate of the detector pulse height resolution by determining the spreading width needed to reproduce the Compton Edge structures (see [62] for more details). The energy resolution is defined as σ/L, where L is the energy value of the Compton Edge. The energy resolution for the two liquid scintillators is equal to $\sigma/L = 6.0\%$ for the Compton Edge of the 1275 keV gamma-ray ($\sigma/L = 8.2\%$ for the Compton Edge of the 511 keV gamma-ray). This figure is slightly better respect to those reported in [62] for a 2"x2" EJ-228 plastic scintillator processed with standard NIM electronics. Finally, the low energy detection threshold, as determined from the spectra in Fig. 8.1, results to be about 60 keV.

Typical PSD versus energy scatter plots are shown in Fig. 8.2 (^{252}Cf $0.7 \cdot 10^4$ n/s

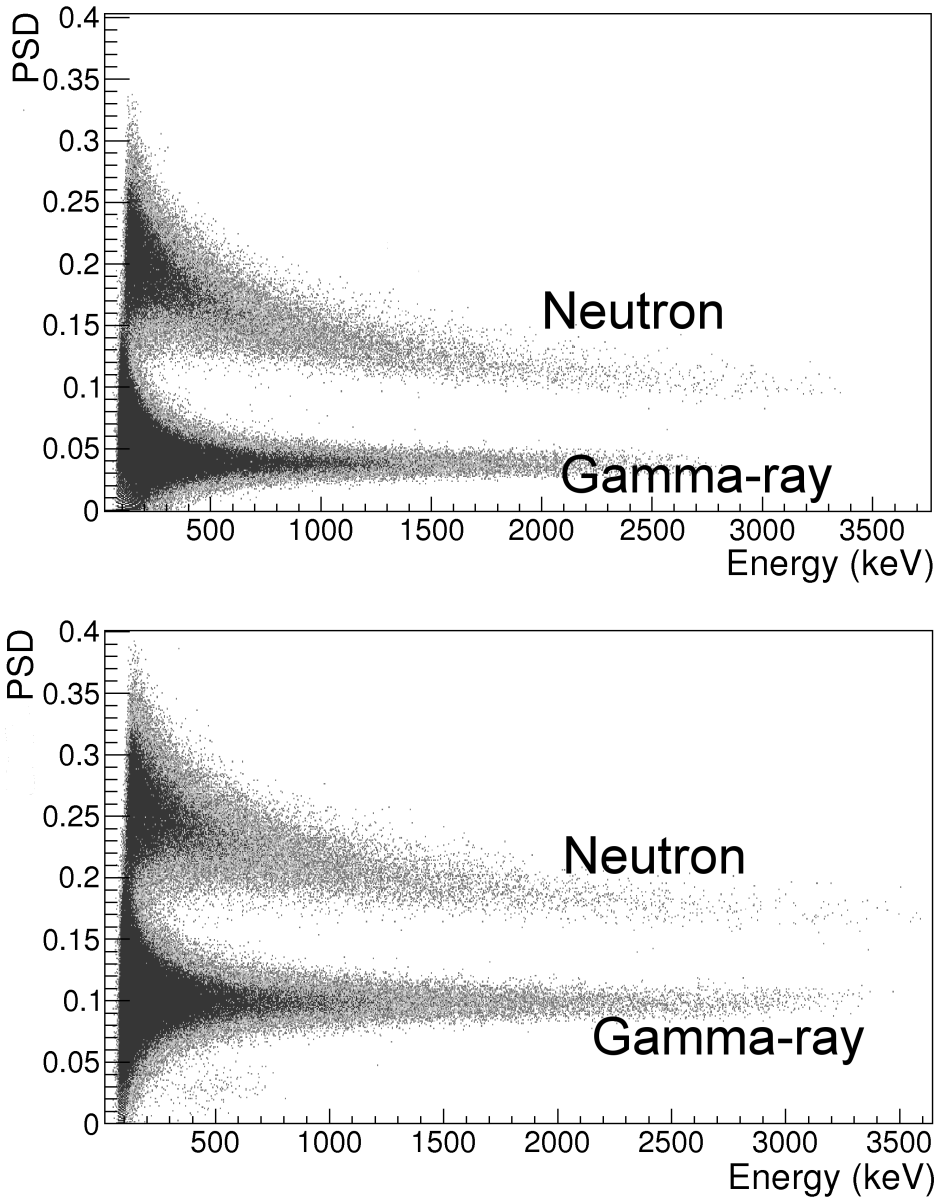

Figure 8.2: Scatter plot PSD versus energy of a ^{252}Cf source measured with the EJ-301 detector (upper) and EJ-309 (bottom).

at 15 cm). In this representation the neutron and gamma regions can be separated by a cut at PSD = 0.09 for the EJ-301 and PSD = 0.16 for the EJ-309 for energies larger than 300 keV.

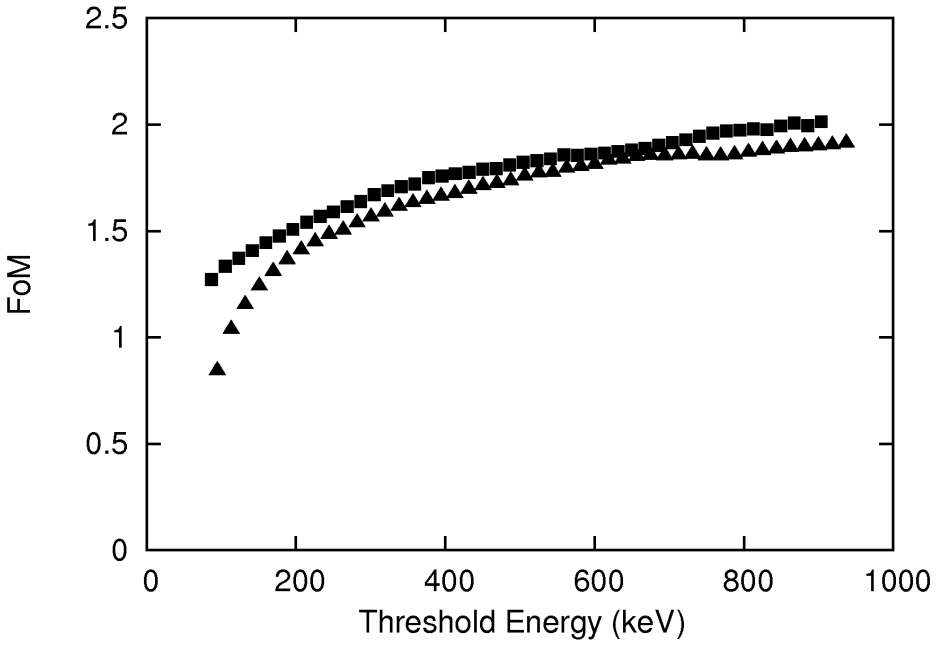

Figure 8.3: Figure-of-Merit parameter (FoM) as a function of the low energy threshold for the detectors studied in this work. EJ-301 squares. EJ-309 triangles. The statistical uncertainties are within the marker size

A number of PSD spectra have been produced and analyzed by varying the low energy threshold. Extracted FoM values are reported in Fig. 8.3 for the two detectors explored in this work as a function of the low energy threshold. We can notice that the FoM increases, improving the discrimination, with the low energy threshold reaching values FoM > 1.5 for thresholds of about 300 keV. This threshold value corresponds to about 1.5 MeV in proton energy by using the response functions provided in [41]. The slightly lower pulse shape capability of the EJ-309 with respect to the EJ-301 is also confirmed, although the measured FoM values for the two detectors are fairly closed. The FoM values measured for the EJ-301 in the present work can be compared with the FoM $= 1.6 - 1.8$ for 4"x2" detectors employing the same liquid scintillator for a threshold of 1.5 MeV proton energy [41] and FoM $= 1.61 - 1.68$ for a 2"x2" BC-501A scintillator for thresholds of 0.6 and 1.0 MeV proton energy [89].

8.1.1 Improve the γ-ray rejection capability

As discussed in details in [90], it is required that the neutron detectors employed in Homeland Security applications shall be able to detect the presence of neutrons inside a high gamma-ray background. As an example, for hand-held instruments the

relevant requirements are contained in the IEC62244 standard [79]. In this case, it is mandatory that the instrument generates a neutron alarm within 10 s sampling time when a 10 ng unmoderated ^{252}Cf source (equivalent to $2 \cdot 10^4$ neutron/s) is placed at 25 cm from the detector, which is equivalent to a distance of 15 cm for our $0.7 \cdot 10^4$ neutron/s source. At the same time it is generally required in Homeland Security applications that neutron detectors shall maintain their performance in presence of gamma radiation at a dose rate of 100μSv/h at the front face of the detection assembly. Obviously this gamma background shall not trigger false neutron alarms. As detailed in [90], this gamma dose rate is produced by a ^{137}Cs source delivering 7800 photons/(s·cm^2) at the front face of the detector.

Two major effects have to be considered when the detector is operated in a high gamma-ray field:

- the possibility of fake neutron events due to physical effects as the signal pile-up as well as instabilities of the front-end electronics at high rate that might produce signals with a neutron-like shape,
- the tail of the gamma-ray peak towards the neutron region in the PSD spectrum.

EJ-301 scintillator

We start considering the number of false neutrons events produced by gamma-rays in the EJ-301 liquid scintillators when the gamma-ray background are increased by using ^{137}Cs sources placed at different distances from the detector front face. After some preliminary tests with a 400 kBq source, a first irradiation was performed by placing a 590 MBq ^{137}Cs source at 67 cm distance from the detector. At this distance the dose rate at the surface of the detector is about 100μSv/h and the detector count rate was about 50 kHz. The PSD scatter plot obtained directly by using the FPGA parameters is reported in the left panel of Fig. 8.4. It is clear that a large number of gamma-ray events are contaminating the neutron region. To reduce the contamination effect it is necessary to operate a pile-up rejection [88]. Moreover, an improvement of the pulse shape discrimination was also obtained in [91] by using a "hybrid" technique through the use of software that processes the digitized signals.

To filter out pile-up events or look for signals that generate fake neutrons, the digitizer operated to record the relevant part of the digitized signal in a time window of 280 ns, which corresponds to the Long Gate integration time. On the stored data file, a filter was applied to detect the presence of pile-up looking at multiple minima in the digitized signal. In addition the FPGA parameters were compared event-by-event with the same parameters derived off-line from the digitized signals. The

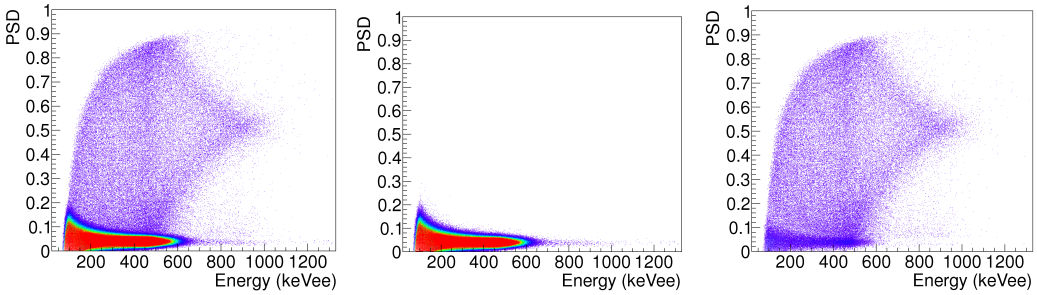

Figure 8.4: PSD scatter plot from the EJ-301 scintillator irradiated with ^{137}Cs source at the dose rate of 100μSv/h. Left: scatter plot obtained from the FPGA processed parameters. Center: scatter plot after the off line event filtering and Right: rejected events. Note that simply looking at the colour code might be misleading, in fact the rejected events represent only about 5% of the total.

filtering action resulted in the rejection of about 2% of events labelled as pile-up but an additional 5% of the events were discarded since they did not fulfil the quality control performed offline on the FPGA parameters. This means that some FPGA integrations (Short or Long Gates) are not correct at this count rate. For example some events have the correct total energy (i.e. the Long Gate integration) but not the Short Gate integration resulting in a wrong determination of the PSD parameter. The result of this action is shown in Fig. 8.4 where are reported the distribution of accepted and rejected events after the filtering. It appears that the filtering operation eliminates all spurious gamma-ray events that would end up in the wrong region of the scatter plot. Once the event filtering strategy was established, the ^{252}Cf source was placed at 15 cm from the detector face together with the 590 MBq ^{137}Cs source to test the possibility of detecting the weak neutron source in a high gamma-ray field as required in Homeland Security applications. The obtained PSD plot of the gamma-neutron test after the filtering is reported in Fig. 8.5: we can notice that the neutron-gamma discrimination is good enough to detect the presence of the neutron source.

We then considered the problem related to the tail of the gamma-ray distribution in the neutron region. This effect is shown in Fig. 8.6 where one-dimensional PSD distributions are shown with the low energy threshold E=300 keV for different irradiations: ^{252}Cf source alone (top panel) ^{252}Cf and^{137}Cs sources with the gamma-ray dose rate of 1 μSv/h (middle panel) and 100 μSv/h (bottom panel). In this representation of the data the neutrons are well discriminated from the gamma-ray even when the relative yield of the gamma-rays is increased by several order of magnitudes. It appears that the PSD threshold for the neutron identification needs to be slightly increased from 0.09 to 0.11 to compensate for the spill of events from the gamma peak at larger PSD values. This means that it is rather difficult to identify neutrons by a simple condition on the PSD parameter independent from

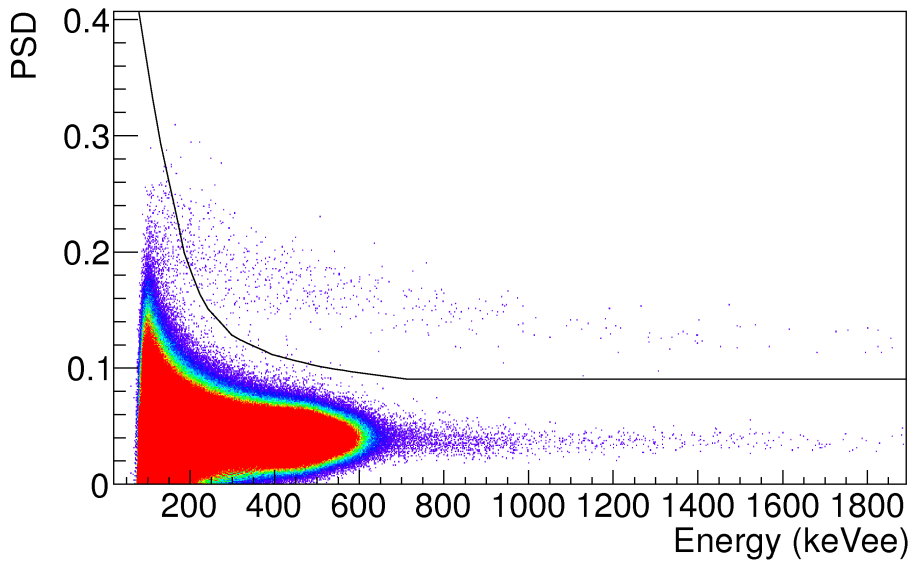

Figure 8.5: PSD scatter plot after off line filtering for a weak ^{252}Cf source in the high gamma-ray background corresponding to 100μSv/h. The line shows the boundary for neutron-gamma events discrimination

the gamma-ray dose rate.

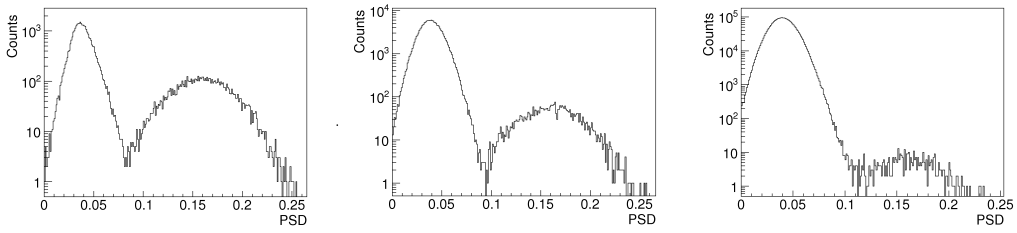

Figure 8.6: Neutron-Gamma PSD distribution for a low energy threshold corresponding to 300 keV. Left: ^{252}Cf source; Middle: ^{252}Cf source in a 1μSv/h gamma-ray background. Right: ^{252}Cf source in a 100μSv/h gamma-ray background.

To optimize the neutron-gamma separation for the different gamma-ray background conditions, a polynomial function was defined, as shown in Fig. 8.5, to define the boundary of the neutron region in the PSD scatter plot. This separation line works good also for lower intensity gamma-ray background. The effect of the event filtering and neutron events selection was studied in detail by looking at the neutron counts for different conditions:

1. the laboratory room background;
2. the ^{252}Cf source placed at 15 cm from the detector;
3. the 100μS/h irradiation with ^{137}Cs only;
4. the irradiation as in 3 but with the ^{252}Cf source of 2.

Irradiation	No Filter	Filter
Background	0.1	0.1
^{252}Cf at 15 cm	58	56
^{137}Cs at 100μSv/h	$6.1 \cdot 10^3$	0.7
^{137}Cs at 100μSv/h and ^{252}Cf at 15 cm	$6.1 \cdot 10^3$	54

Table 8.1: Average neutron counts registered for 10 s time bins with the EJ-301 scintillator for different irradiations.

The results, in terms of the average number of detected neutrons for 10 s time bins, are reported in Table 8.1 showing the impressive effect of the software filtering: in a high intensity gamma-ray field more than 6000 "fake" neutrons counted in 10 s are rejected allowing the detection of the ^{252}Cf source. Moreover the software filter does not reject true neutron events, therefore it is possible to detect a weak neutron source in a strong gamma-ray background with an extremely good signal-to-background ratio S/B = 54/0.7 = 77.

Finally, the false alarm rate (FAR) and the probability of detection (PD) was determined following the prescriptions of [76] for 10 s sampling time, as required by the standard IEC62327 for hand-held instruments [79]. Results are reported in Table 8.2. We started with a long room background run that provided 188 sets of data, each one characterized by 10 s sampling time. The average number of detected neutrons was so low that the threshold for neutron alarm was set to N > 1 neutron event. With this threshold, the probability of positive false alarm was about 0.53% with the room background and about 5% with the high gamma-ray background. On the contrary, the probability of alarm with the ^{252}Cf source was 100% in both experimental configurations. The results reported in Table 8.2 demonstrate that the probability of detection of the ^{252}Cf source is PD = 95% at 95% confidence level in both cases of gamma-ray background. It is also worth noting that the false alarm rate is strongly dependent on the alarm threshold N > 1. We recall that such low threshold was set considering the very low counting rate of neutrons in the room background. This value would allow us to detect extremely low intensity neutron sources in standard natural gamma-ray background. On the other hand a slight increase of the threshold value would result in a substantial reduction of the false alarm rate in a strong gamma-ray background.

EJ-309 scintillator

The experimental tests described in previous section were repeated with the EJ-309 scintillator obtaining results very close to those of EJ-301. The PSD scatter plot obtained after software filtering for the ^{252}Cf and ^{137}Cs at 100μSv/h dose rate irradiation is reported in Fig. 8.7. Here the polynomial line is used to discriminate

Irradiation	Trials	Neutron alarms
Background	188	1 (0.53%)
^{252}Cf at 15 cm	59	59 (100%)
^{137}Cs at 100μSv/h	58	3 (5%)
^{137}Cs at 100μSv/h and ^{252}Cf at 15 cm	61	61 (100%)

Table 8.2: Neutron alarms with the EJ-301 scintillator in different irradiations.

Irradiation	No Filter	Filter
Background	1.0	0.1
^{252}Cf at 15 cm	60	57
^{137}Cs at 100μSv/h	$5.6 \cdot 10^3$	1.0
^{137}Cs at 100μSv/h and ^{252}Cf at 15 cm	$5.6 \cdot 10^3$	53

Table 8.3: Average neutron counts registered for 10 s time bins with the EJ-309 scintillator for different irradiations.

gamma-ray and neutrons with EJ-309.

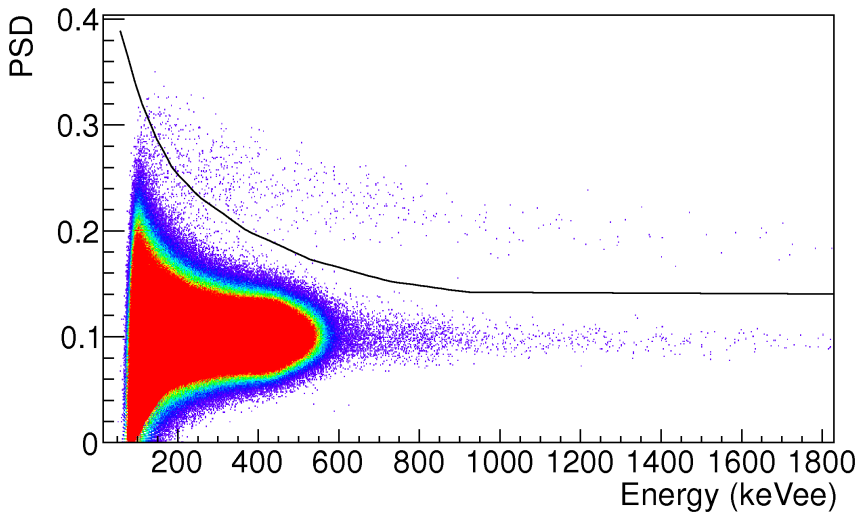

Figure 8.7: EJ-309 PSD scatter plot after off line filtering for a weak ^{252}Cf source in the high gamma-ray background corresponding to 100μSv/h. The line shows the boundary for neutron-gamma events discrimination

It appears that a sufficiently good discrimination is obtained after software filtering also using the EJ-309 scintillator. Numerical results in terms of average number of detected neutrons for 10 s time bins are reported in Table 8.3, where it is shown that the behaviour of the EJ-309 scintillator is substantially the same as EJ-301. Indeed the off line software filtering the number of "fake" neutrons is almost zero so that the detection of a ^{252}Cf source appears to be possible also in this case.

However one should mention that EJ-309 exhibits events with an irregular signal shape giving rise to a certain number of "fake" neutrons when processed by

Irradiation	Trials	Neutron alarms
Background	188	4 (2.1%)
^{252}Cf at 15 cm	59	59 (100%)
^{137}Cs at 100μSv/h	62	3 (4.8%)
^{137}Cs at 100μSv/h and ^{252}Cf at 15 cm	63	63 (100%)

Table 8.4: Neutron alarms with the EJ-309 scintillator in different irradiations.

the FPGA even at low gamma-ray intensities, typical of natural room background. Nevertheless the software filter rejects such fake neutrons.

Finally in Table 8.4 we show results on false alarms and detection capability related to the EJ-309 scintillator. Also in this case the threshold for the neutron alarm is N > 1 event and the probability of positive false alarms is about FAR = 4.8% in the high gamma-ray background. The probability of detection is PD = 95% at 95% confidence level. As a conclusion the performances of EJ-309 measured in this work are essentially equivalent to those of EJ-301.

8.1.2 Measurements at higher dose

Additional short irradiations were also performed by changing the 590 MBq ^{137}Cs source-detector distance to 47 and 37 cm, which correspond to a dose rate of 200 and 300 μSv/h respectively. In such conditions, it is still possible to identify neutrons after software filtering. In Fig. 8.8 we reported PSD scatter plots for the EJ-301 and EJ-309 scintillators irradiated by the ^{137}Cs at 37 cm and ^{252}Cf sources with and without the software off-line filtering.

It is worth mentioning that in those irradiations the rejection of events was quite high: about 4% of the events were rejected because of the pile-up filter and 10% after the FPGA quality check. The possibility of performing PSD in such extreme conditions is also documented in Fig. 8.9 where the PSD distributions are shown for the two scintillators with a energy threshold of 300 keV.

8.2 Compact portable spectrometer

Looking at the possibility of using EJ-309 detector as a compact portable neutron-gamma spectrometer, we studied the detector properties by replacing a traditional linear focused PMT by a Flat Panel type. Such device offers several advantages with respect to the traditional one having roughly the same cost: first of all it is extremely compact reducing substantially the overall length of the detector. Secondly it has a lower power requirement and, finally, it is less sensitive to magnetic fields. Thus it seems to be well suited for portable instruments.

The detectors studied in this work consist of two cylindrical EJ-309 liquid scintil-

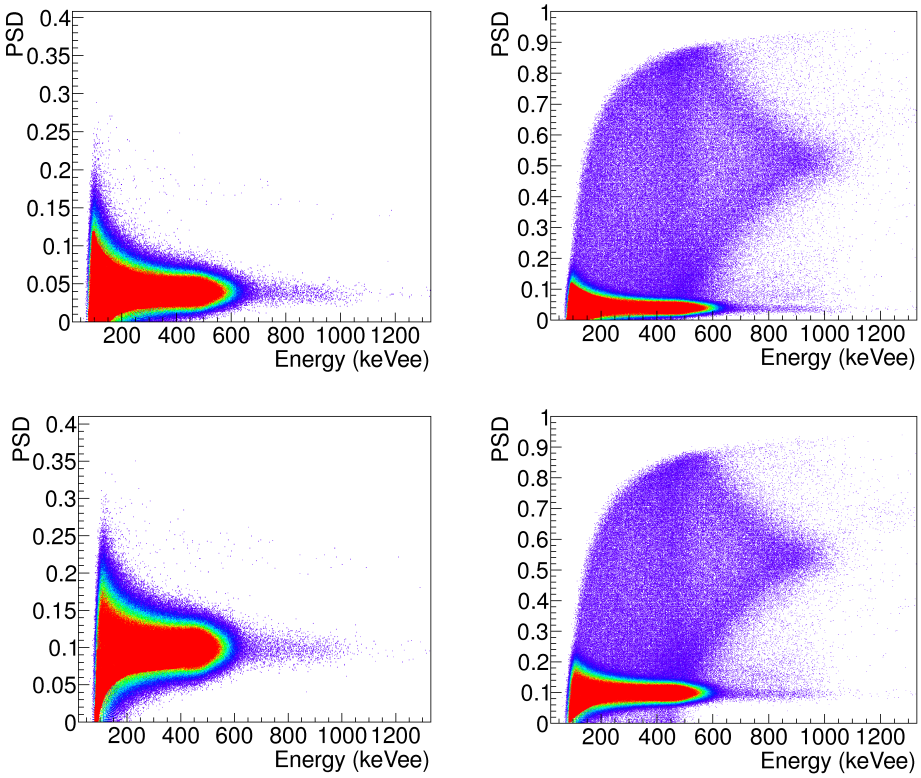

Figure 8.8: PSD scatter plot before (left panel) and after (right panel) off line filtering for a weak ^{252}Cf source in the high gamma-ray background corresponding to 300 μSv/h. Top: EJ-301. Bottom: EJ-309.

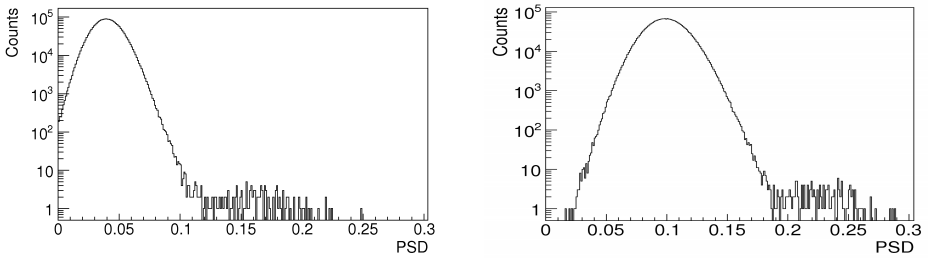

Figure 8.9: PSD distribution for the EJ-301 (left panel) and EJ-309 (right panel) scintillators in case of the weak ^{252}Cf source in the high gamma-ray background (dose rate 300 μSv/h) with a low energy threshold of 300 keV.

	Detector A	Detector B
PMT	H1949-51	H8500
Dimensional Outline	Max Diameter 7.5 cm Total Length 23.5 cm	Area 8.5 x 8.5 cm^2 Total Length 2.8 cm
Total Weight	900 g	940 g
Operating Voltage	-1600 V	-1050 V
Divider current A	0.80 mA	0.20 mA

Table 8.5: Comparison between Detector A and B features.

lator cells 5 cm diameter by 5 cm thickness. As in previous paragraph, one cell was coupled to an H1949-51 HAMAMATSU liner focused 12 dynodes photomultiplier (PMT) through an EJ-560 silicon rubber interface. In the following we indicate this detector as Detector A. A second cell was coupled by using the EJ-560 interface to an H8500 HAMAMATSU flat panel position sensitive photomultiplier (PSPMT). In the following we indicate this second device as Detector B. It is worth noting that the two PMTs have a rather equivalent cost. The PSPMT is characterized by a square active area of about 5x5 cm^2 divided in 64 independent anodes (pixels). In our application all anodes outputs were properly connected together, consequently the use of the PSPMT is perfectly equivalent to the PMT: a single HV channel and a single anode signal.

Table 8.5 compares the major technical features of the two PMTs relevant for the present application. The two major advantages in using the PSPMT are clearly evident: size reduction of the device and lower power requirement. In the present work the detector anode signals are directly fed into a CAEN DT5751 10 bit 1 GS/s Digitizer. The detectors are operated at HV= 1600 Volt and HV= 1050 V for the H1949-51 and H8500 MPTs respectively, to avoid saturation effects in digitizing the pulses. Inside the DT5751 card, Digital Pulse Processing (DPP) algorithms are implemented using FPGA as described in Section 4.5.

The energy calibration of the scintillation light was established by the procedure described in [62]. Samples of gamma ray energy spectra obtained with a ^{22}Na radioactive source are reported in Fig. 8.10. It is immediately evident that the spectra measured with the two detectors exhibits a similar energy resolution as deduced from the width of the Compton Edge for the 511 keV gamma ray. The energy resolution derived in this case is 5.0%, 4.7% for the 1275 keV gamma-ray, 8.8% and 8.2% for the 511 keV gamma-ray for detector A and B respectively. Finally, the low energy detection threshold, as determined from the spectra in Fig. 8.10, results to be below 50 keV. It is interesting to note that the slightly better energy resolution obtained with the H8500 PSPMT is most probably related to the larger photo-cathode quantum efficiency ($> 20\%$) in the range 300-400 nm, compared to

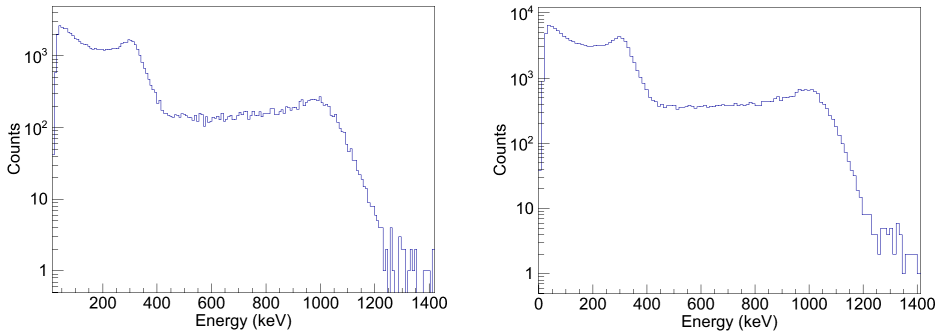

Figure 8.10: Calibrated gamma ray energy spectra obtained with a ^{22}Na source. Detector A left panel. Detector B right panel

that of the H1949-51 assembly ($< 20\%$) in the same wavelength range.

The pulse shape discrimination (PSD) of the two detectors was studied as in previous paragraph 8.1. Typical PSD versus energy scatter plots are shown in figure 8.11.

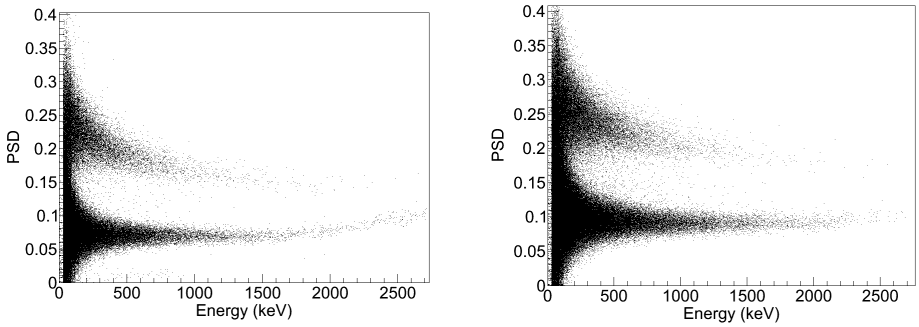

Figure 8.11: Pulse Shape Discrimination scatter plots: PSD versus energy. Left panel Detector A. Right panel Detector B

PSD spectra reported in figure 8.12 have been produced setting 300 keV low energy thresholds. Extracted FoM values are 1.67 and 1.66 for the Detectors A and B respectively, showing no difference

8.2.1 Operation in magnetic field

The detectors have been tested when operated in a magnetic field. Gamma ray spectra from a ^{22}Na source were measured with the detectors positioned in proximity of a dipolar electromagnet. The magnetic field value at the detector position was measured by a Hall probe (LABORATORIO ELETTROFISICO model DG4080 with a Hall probe FW BELL model STD 58-0404). The spectra measured with detector A and B for different magnetic field values are reported in Fig. 8.13 and 8.14, respectively.

As reported in Fig. 8.13, the gain of the photomultiplier for detector A decreases

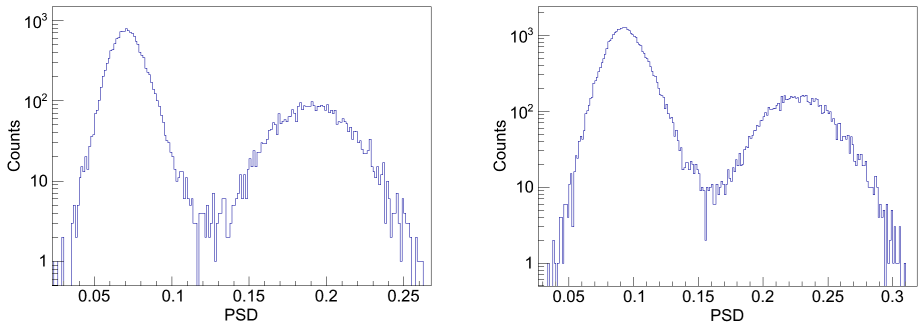

Figure 8.12: Pulse Shape spectra for 300 keV low energy threshold. Left panel Detector A. Right panel Detector B.

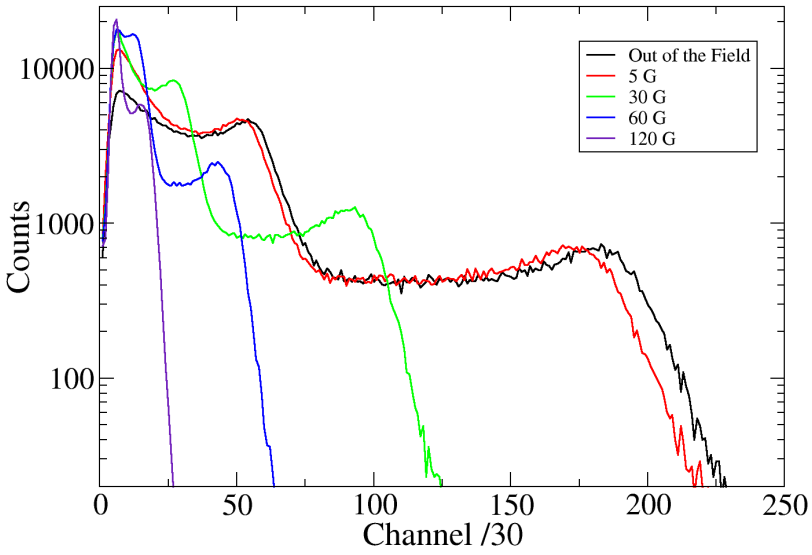

Figure 8.13: Pulse height distributions measure for different magnetic field values for detector A.

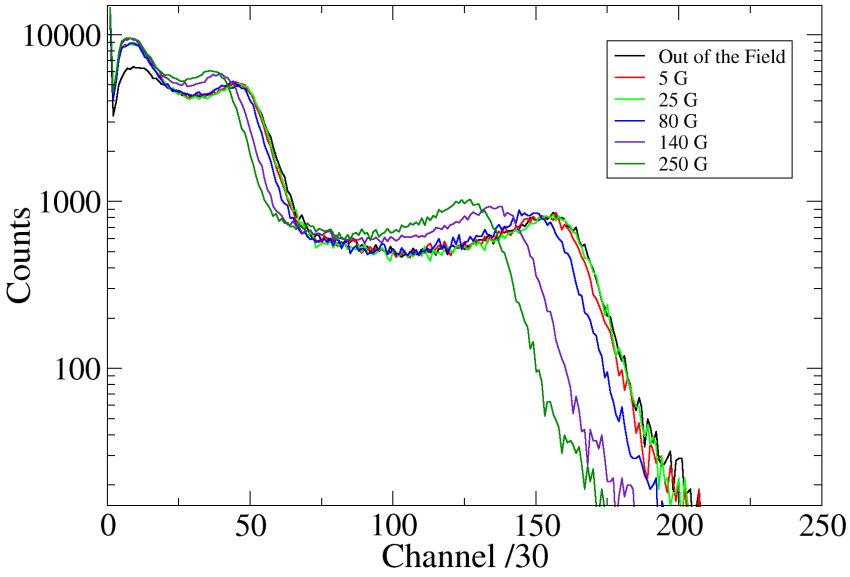

Figure 8.14: Pulse height distributions measure for different magnetic field values for detector B.

as the magnetic field increasing, with a corresponding deterioration of the energy resolution. As an example, the pulse height corresponding to the 1275 keV Compton Edge is reduced by about 70-80 % at 60 Gauss, with a reduction of energy resolution from 5% to 11%. The behaviour of detector B is rather different, as documented in Fig. 8.14. In this case the reduction of the Compton Edge position is within 20% when the field is about 250 Gauss with a correlated deterioration of energy resolution of the same order. This effect is certainly related to the larger distance between adjacent dynodes in the linear focused PMT, while in the Flat Panel design the dynode structure is more compact. As a result, the magnetic deflection of electrons with consequent loss of signal, caused the lowering of the final gain.

8.2.2 Time resolution

Specific test was performed to compare the time resolution achievable with detectors A and B. It is well known that the intrinsic rise time of the H8500 PSPMT single anode signal is better than the H1949-51 PMT one. However there is a small variable delay among the different anodes that needs to be taken into account when measuring time-of-flight [92]. As an example, the distribution of the relative delay with respect to one anode taken as reference is reported in Fig. 8.15. It seems that the average relative delay is about 500 ps with a width of about 500 ps [FWHM]. The latter does certainly contribute to the overall time resolution of a H8500 PMT when all anodes are read together as in the present application.

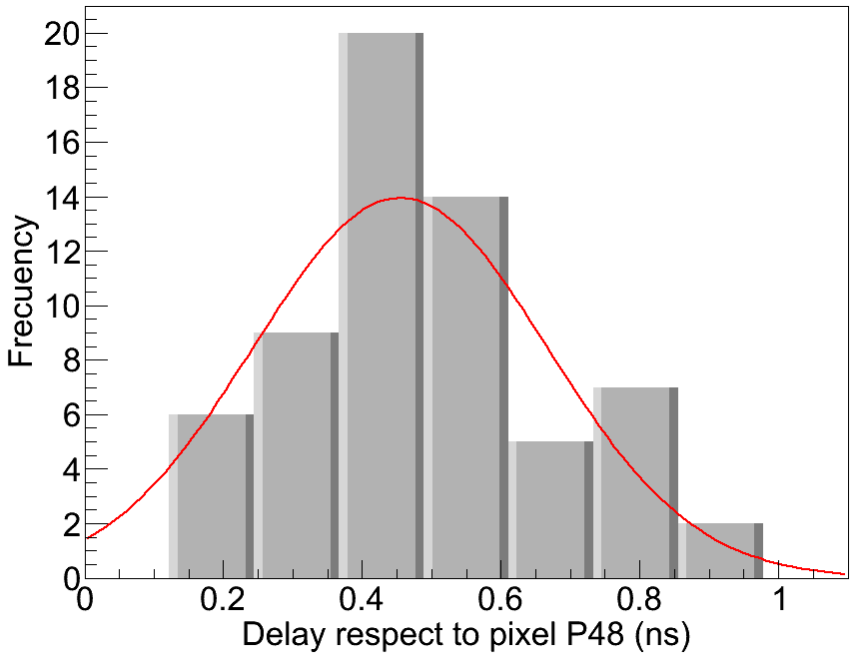

Figure 8.15: Relative distribution of the anode delays of a H8500 PMT

Experimental tests were performed by measuring gamma-gamma coincidences with a ^{22}Na source using a fast plastic (EJ-228 2"x2" coupled with a XP2020 PMT) as reference detector. The contribution to the overall measured time resolution of the fast plastic was experimentally determined by running two of such detectors in coincidence. Experimental data were acquired by the DT5751 digitizer. Experimental results are reported in Fig. 8.16 where the time resolution of single detectors (fast plastic EJ-228, detector A and detector B) are reported as a function of the energy threshold in the virtual CFTD. It appears that clustering the anodes of the H8500 PSPMT to provide a single timing signal deteriorates the achievable time resolution compared to the linear focus PMT. This can be explained by the delay distribution of the pixels (reported in Fig. 8.15) as well as additional delay due to the anodes connecting lines. However, it is worth mentioning that a sub-nanosecond time resolution is obtained even with a 100 keV low-energy threshold, well within the requirements of several applications.

8.2.3 Propotype

A first prototype of a compact spectrometer realized with new EJ-309 liquid scintillator coupled with H8500 Flat Panel is shown in Fig. 8.17.

The main characteristics are compactness, light weight, low power consumption, battery operated, usable within a weak magnetic field and controlled with small digital electronics. The total weight of the present prototype (including the computer)

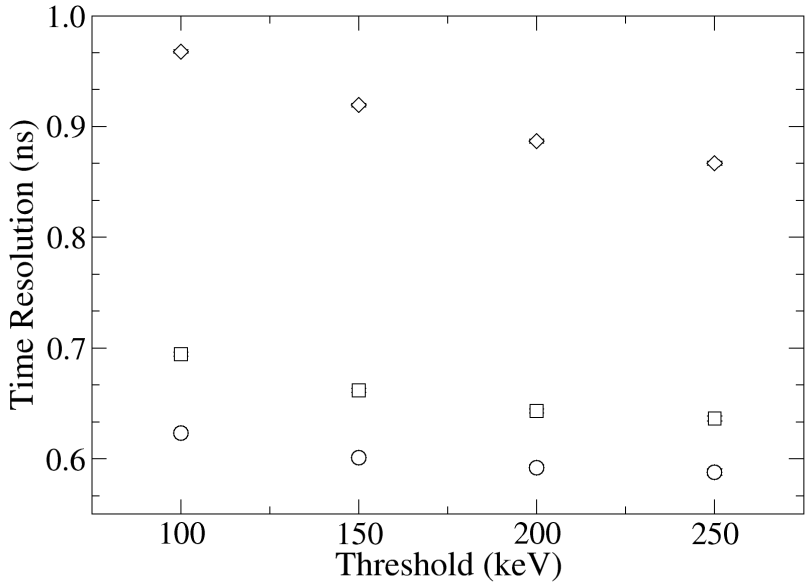

Figure 8.16: Time resolution of a single scintillation detector as measured with a ^{22}Na source as a function of the virtual CFTD energy threshold. Circles, squares and diamonds refer to the reference fast plastic detector: Detector A and Detector B, respectively

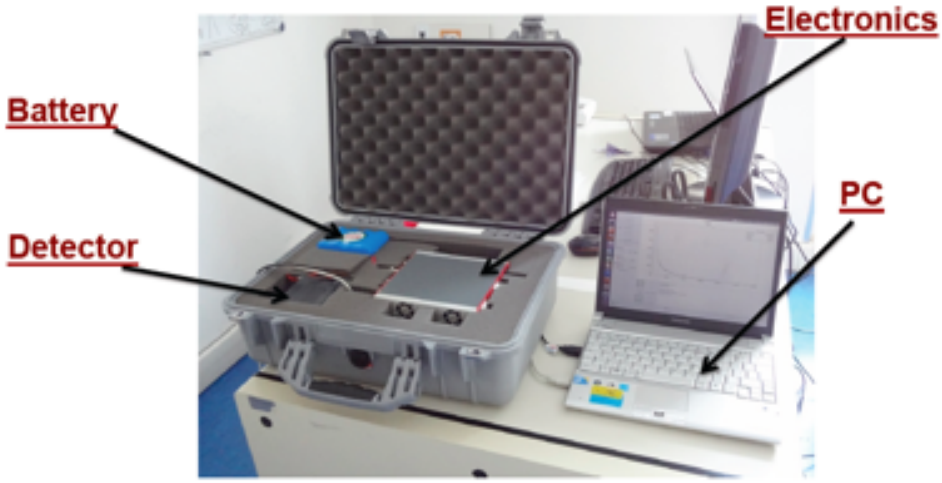

Figure 8.17: Prototype of battery operated neutron gamma spectrometer

is about 8.9 kg with a battery granting a working time of about 2.5 h. The prototype is currently under laboratory characterization. The efficiency of the detector for neutron and gamma rays complies with the requirements of IEC standards [79]. Moreover, software is under development to identify the radioactive sources using the relevant features of the spectra. First results show that the prototype satisfies IEC requirements for determining the presence of gamma ray sources in addition to the natural background as well as for isotope identification. The neutron detection capability of the system will open the possibility of detecting the presence of a weak neutron source as well as to get information about the neutron energy from the pulse shape distribution. First applications of the spectrometer are envisaged in the field of plasma physics and fusion research and engineering.

Chapter 9

Summary and conclusions

9.1 Detector performances

All the detector used in SMANDRA system have been fully characterized. Initial tests were done with traditional analog NIM electronics followed by the new digital electronics based on fast digitizers. Concerning the high efficiency detector for γ-ray (5"x5" NaI(Tl)), it was found an energy resolution of 7.7% for the 511 keV full energy peak with analog electronic comparable with values reported in literature [25]. A significant improvement of the measured energy resolution is obtained using digital electronic (fast digitizer CAEN V1720), in particularly at lower energy where the resolution for the 511 keV peak decreases to 7.0%. The detector maintains a good energy linearity in all the energy range investigated with active interrogation between few keV up to 8 MeV.

The energy resolution of a $LaBr_3$(Ce) scintillation detector improves by using the V1720 resepect to the resolution obtained with the same detector equipped with standard NIM shaping amplifiers up to 20 kHz. The values decrease from 3.5% at 511 keV with NIM electronics to 3.2% for fast digitizers. Saint-Gobain guarantees, for this detector, resolution better than 3.5% on ^{137}Cs peak at 662 keV. With the same source we measured a resolution of 3.12%, 11% better than nominal value. Further study has been performed to check the performances up to very high counting rate by using a 12bit 250 MS/s CAEN V1720 digitizer. Despite a slight deterioration at high rate, the energy resolution is generally better than the measured one using standard NIM electronics and is generally lower than the value declared by Saint-Gobain up to very high rates (i.e. 340 kHz). Instead $LaBr_3$(Ce) detector reveals a non-linearity in energy calibration for the largest pulse heights. Such effect is evident over 2 MeV and it is due to saturations of the PMT. In our case, this non-linearity has been compensated by using an additional quadratic term into the energy calibration. This procedure is necessary in active interrogations when photons in the range 2-7 MeV are of primary interest.

The time resolution was obtained processing off line the digitized signals in a

gamma-gamma experiment against a fast plastic scintillator. For $LaBr_3(Ce)$ detector the time resolution is about $\delta t = 1.2$ ns [FWHM] to be compared with $\delta t = 0.65$ ns [FWHM] when standard NIM Constant Fraction Time Discriminators are used. However the time resolution by using the V1720 digitizer is enought for the present application. Indeed results presented in section 4.8 demonstrate the possibility to get the following time resolution:

- 1 ns for fast detectors, i.e. $LaBr_3(Ce)$ and NE-213 liquid scintillator,
- 5 ns in the case of NaI(Tl) detector with a threshold of 500 keV.

These values are compatibile with SMANDRA requirements for NDA with tagged neutrons. We noticed that 5 ns correspond to 25 cm of flight distance for 14 MeV neutrons, and this would be the effective space resolution of the system using NaI(Tl) scintillator; with other two detectors the resolution would be smaller than 10 cm.

The performaces of NE-213 liquid scintillator were optimized as a function of the FoM parameter. Better performances were obtained with digital electronics respect to the classic NIM chain. The FoM parameter for NE-213, computed in an energy range of 400-1400 keVee, is 1.08 and 0.90 for digital and analog electronics respectively. This value ensures a good discrimination capability between neutron and γ-ray that allows the identification of neutrons as required from standards. Specific tests were performed at high rates to check the discrimination capability in presence of a intense γ-ray sources. The result shows a worsening of the FOM at high rate (35 kHz) of about 20% for NE-213 detector due mainly to signal pileup and electronic instabilites. Further tests performed with new detectors demonstrate the possibility to maintain the discrimination capability up to several hundred of kHz (300 kHz). This is due to better performance of new liquid scintillator and to the development of the FPGA firmware in which are now implemented a quality check on the FPGA output and a filter for pileup rejection.

9.2 Project goals

The detection and identification of standard radioactive sources (gamma ray and neutrons) has been tested successfully showing detection probability in order or even better with the requirements of this type of instrumentation.

The detection of special nuclear material has been tested with the mobile SMANDRA inspection system both as a high sensitivity passive spectroscopic system and as a complete active inspection system using tagged neutrons. The detection of plutonium samples seems to be possible with passive interrogation even in case of small samples (few grams) due to the yield of gamma ray and neutrons.

As it is well known, detection of uranium samples poses more problems because of the low neutron yield that characterizes this material. The gamma ray yield of highly enriched U samples could be easily shielded. In this case active interrogation is needed. Results of our work show that the SMANDRA inspection system is able to provide signature for the discrimination of uranium against heavy metals (as lead) by looking to the absolute gamma and neutron yield in coincidence with tagged neutrons or to correlations between detectors. It is worth mentioning that the SMANDRA system is a mobile multi-purpose spectrometric system not specifically designed to detect SNM. However the results reported might be implemented in future portable systems specifically designed to detect SNM in active mode. Some further results obtained with small detector cells are reported in Sec. 8 demonstrating some follow-up application of the SMANDRA know-how.

9.3 Publications

The publications concerning the SMANDRA system:

- D. Cester, D. Fabris, M. Lunardon, S. Moretto, G. Nebbia, S. Pesente, L. Stevanato, G. Viesti. *An integrated mobile system for port security.* ANIMMA Conf. Proc. 2011.

- D. Cester, G. Nebbia, L. Stevanato, G Viesti, F. Neri, S. Petrucci, S. Selmi, C. Tintori, P. Peerani, A. Tomani. *Special nuclear material detection with a mobile multi-detector system.* Nucl. Instr. and Meth. Section A, Volume 663, Issue 1, 21 January 2012, Pages 5563.

- D. Cester, G. Nebbia, L. Stevanato, G Viesti, F. Neri, S. Petrucci, S. Selmi, C. Tintori, P. Peerani, A. Tomani. *Special Nuclear material detection with a mobile multi-detector system.* AIP Conf. Proc. 1423, Pages 335-340, 2012.

- D. Cester, G. Nebbia, L. Stevanato, G. Viesti, F. Neri, S. Petrucci, S. Selmi, C. Tintori. *High rate read-out of $LaBr_3$(Ce) scintillator with the CAEN V1720 FADC.* AIP Conf. Proc. 1423, Pages 441-445, 2012.

- Stevanato et al. *High rate read-out of $LaBr_3$(Ce) scintillator with a fast digitizer.* Nucl. Instr. and Meth. Section A, Volume 678, 21 June 2012, Pages 8387.

- Stevanato et al. *Neutron detection in a high gamma-ray background with EJ-301 and EJ-309 liquid scintillators.* Nucl. Instr. and Meth. Section A, Volume 690, 21 October 2012, Pages 96-101.

Conference presentation:

- IEEE (NSS-MIC) 2011 - Nuclear Science Symposium, Medical Imaging Conference. *An integrated mobile system for port security* , 22-29 Ottobre 2011, Valencia, Spagna.

- CAARI 2012 - 22st International Conference on the Application of Accelerators in Research and Industry. *Neutron detection in a high gamma ray background with liquid scintillators*, 5-10 Agosto 2012, Forth Worth (TX), USA.

Finally, the work performed with the SMANDRA system has been the seed for an Italian Patent "Metodo per il riconoscimento di sorgenti radiattive" (PD2011A000236 12 July 2011) under request of the Padova University, inventors G. Viesti, G. Nebbia, L. Stevanato and D. Cester. The matter of the patent is not presented in this thesis work.

Bibliography

[1] R.A. Falkernrath et al. *Americas Achilles Heel.* Cambridge, MA: The MIT Press, 1998.

[2] Reuters. *Race against time to prevent nuclear terror - IAEA.* 2004.

[3] T.E. Valentine. *Techical Report ORNL/TM-1999/300*, 1999.

[4] `http://www.elsagdatamat.com/PDF/EDLink34.pdf`.

[5] S. Pesente, G. Nebbia, M. Lunardon, G. Viesti, S. Blagus, K. Nad, D. Sudac, V. Valkovic, I. Lefesvre, and M.J. Lopez-Jimenez. Tagged neutron inspection system (TNIS) based on portable sealed generators. *Nucl. Instrum. and Meth.*, B241:743–747, 2005.

[6] R. Nicolini, F. Camera, N. Blasi, S. Brambilla, R. Bassini, C. Boiano, A. Bracco, F.C.L. Crespi, O. Wieland, G. Benzoni, S. Leoni, B. Million, D. Montanari, and A. Zalite. Investigation of the properties of a 1"x1" $LaBr_3$:Ce scintillator. *Nucl. Instrum. and Meth.*, A582:554–561, 2007.

[7] M. Ciemala, D. Balabanski, M. Csatlos, J.M. Daugas, G. Georgiev, J. Gulys, M. Kmiecik, A. Krasznahorkay, S. Lalkovski, A. Lefebvre-Schuhl, R. Lozeva, A. Maj, and A. Vitez. Measurements of high-energy γ-rays with $LaBr_3$:Ce detectors. *Nucl. Instrum. and Meth.*, A608:76–79, 2009.

[8] M. Balcerzyk, M. Moszyski, and M. Kapusta. Comparison of $LaCl_3$:Ce and NaI(Tl) scintillators in γ-ray spectrometry. *Nucl. Instrum. and Meth.*, A537:50–56, 2005.

[9] S. Marrone, D. Cano-Ott, N. Colonna, C. Domingo, F. Gramegna, E.M. Gonzalez, F. Gunsing, M. Heil, F. Kappeler, P.F. Mastinud, P.M. Milazzog, T. Papaevangelouh, P. Pavlopoulos, R. Plag, R. Reifarth, T. Tagliente, J.L. Tain, and Wisshak. W. Pulse shape analysis of liquid scintillators for neutron studies. *Nucl. Instrum. and Meth.*, A490:299–307, 2002.

[10] R. T. Kouzes, J.H. Ely, A. Seifert, E. R. Siciliano, D. R. Weier, L. K. Windsor, M. L. Woodring, J. Borgardt, E. Buckley, E. Flumerfelt, A. Oliveri, and

M. Salvitti. Cosmic-ray induced ship-effect neutron measurements and implications for cargo scanning at borders. *Nucl. Instrum. and Meth.*, A587:90–100, 2008.

[11] M.S. Gordon, P. Goldhagen, K.P. Rodbell, T.H. Zabel, H.H.K. Tang, J.M. Clem, and P. Bailey. Measurement of the flux and energy spectrum of cosmic-ray induced neutrons on the ground. *IEEE Trans. Nucl. Sci.*, 51:3427–3434, 2004.

[12] R. T. Kouzes, E. R. Siciliano, J. H. Ely, P. E. Keller, and R. J. McConn. Passive neutron detection for interdiction of nuclear material at borders. *Nucl. Instrum. and Meth.*, A584:383–400, 2008.

[13] G. Vourvopoulos and P.C. Womble. Pulsed fast/thermal neutron analysis: a technique for explosives detection. *Talanta*, 54:459–468, 2001.

[14] T. Gozani. The role of neutron based inspection techniques in the post 9/11/2001 era. *Nucl. Instrum. and Meth.*, B213:460–463, 2004.

[15] A. Perez-Andujara and L. Pibida. Performance of CdTe, HPGe and NaI(Tl) detectors for radioactivity measurements. *Applied Radiation and Isotopes*, 60:41–47, 2004.

[16] J. Kockum. The response to high-energy gamma rays of a NaI(Tl) scintillation spectrometer. *Nucl. Instrum. and Meth.*, 4:171–180, 1959.

[17] J.H. Ha, J.C. Kim, Y.K. Kim, M. Youn, S.J. Chae, H.T. Chung, J.H. Choi, C.S. Lee, J.U. Kwon, C.B. Moon, J.S. Chai, Y.S. Kim, and J.D. Lee. Energy measurement of 50 MeV proton beam with a NaI(Tl) scintillator. *Nucl. Instrum. and Meth.*, 350:411–414, 1994.

[18] Saint-Gobain Crystals. Efficiency calculations for selected scintillators. `http://www.detectors.saint-gobain.com/uploadedFiles/SGdetectors/Documents/Technical_Information_Notes/Efficiency-Calculations.pdf`.

[19] C.M. Rosza and et al. Performance summary: Brillance scintillators $LaCl_3$ and $LaBr_3$, Saint Gobain crystals. Available at `www.detectors.saint-gobain.com`.

[20] E.V.D van Loef, P. Dorenbos, C.W.E van Eijk, K.W Krmer, and H.U Gdel. Scintillation properties of $LaBr_3$ crystals: fast, efficient and high-energy-resolution scintillators. *Nucl. Instrum. and Meth.*, A486:254–258, 2002.

[21] A. Iltis, M.R. Mayhugh, P. Menge, C.M. Rozsa, O. Selles, and V. Solovyev. Lanthanum halide scintillators: Properties and applications. *Nucl. Instrum. and Meth.*, A563:359–363, 2006.

[22] P. Menge, G. Gautier, A. Iltis, C. Rozsa, and V. Solovyev. Performance of large lanthanum bromide scintillators. *Nucl. Instrum. and Meth.*, A579:6–10, 2007.

[23] M. Moszyski, A. Nassalski, A. Syntfeld-Kauch, T. Szczniak, W. Czarnacki, D. Wolski, G. Pausch, and J Stein. Temperature dependences of LaBr3(Ce), LaCl3(Ce) and NaI(Tl) scintillators. *Nucl. Instrum. and Meth.*, A568:739–751, 2006.

[24] S.O. Flyckt and C. Marmonier. Photomultiplier Tubes - Principle and Applications. *Photonis*, 2002.

[25] Saint-Gobain data sheet, Brilance 380. `http://www.detectors.saint-gobain.com/uploadedFiles/SGdetectors/Documents/Technical_Information_Notes/BrilLanCe-Scintillators-Performance-Summary.pdf`.

[26] R. Casanovas, J.J. Morant, and M. Salvado. Energy and resolution calibration of NaI(Tl) and LaBr3(Ce) scintillators and validation of an EGS5 Monte Carlo user code for efficiency calculations. *Nucl. Instrum. and Meth.*, A675:78–83, 2012.

[27] F.G.A. Quarati, A. Owens, P. Dorenbos, J.T.M. De Haas, G. Benzoni, N. Blasi, C. Boiano, S. Brambilla, F. Camera, R. Alba, G. Bellia, D. Maiolino, C.and Santonocito, M. Ahmed, N. Brown, S. Stave, H.R. Weller, and Y.K. Wu. High energy gamma-ray spectroscopy with $LaBr_3$ scintillation detectors. *Nucl. Instrum. and Meth.*, A629:159–169, 2011.

[28] R. Scaf, R. Pani, R. Pellegrini, P. Bennati, M. Nerina Cinti, G. De Vincentis, and E. Di Castro. Spectral matching factors for LaBr3:Ce crystals coupled to Hamamatsu H8500 family PMTs. *Nucl. Instrum. and Meth.*, A643:89–94, 2011.

[29] J. Nilsson. *Using the $LaBr_3$:Ce scintillation detector for mobile γ-spectrometry.* Lund University, 2010.

[30] K. Alzimami, E. Abuelhia, Z. Podolyak, A. Ioannou, and N. Spyrou. Characterization of $LaBr_3$: Ce and $LaCl_3$: Ce scintillators for gamma-ray spectroscopy. *J. of Radioanalytical and Nucl. Chem.*, 278:755–759, 2008.

[31] B. Milbrath, R. Runkle, T. Hossbach, W. Kaye, E. Lepel, B. McDonald, and L. Smith. Characterization of alpha contamination in lanthanum trichlo-

ride scintillators using coincidence measurements. *Nucl. Instrum. and Meth.*, A547:504–510, 2005.

[32] W. Kernan. Self-activity in lanthanum halides. In *2004 IEEE Nuclear Science Symposium Conference Record*, volume 2, 2004.

[33] L.M. Bollinger and G.E. Thomas. Measurement of the time dependence of scintillation intensity by a delayedcoincidence method. *Rev. Sci. Instrum.*, 32:1044, 1961.

[34] J.M. Adams and G. White. A versatile pulse shape discriminator for charged particle separation and its application to fast neutron time-of-flight spectroscopy. *Nucl. Instrum. and Meth.*, 156:459–476, 1978.

[35] S.D. Jastaniah and Sellin P.J. Digital techniques for n/γ pulse shape discrimination and capture-gated neutron spectroscopy using liquid scintillators. *Nucl. Instrum. and Meth.*, A517:202–210, 2004.

[36] J. Sderstrm, P.A. Nyberg and R. Wolters. Digital pulse-shape discrimination of fast neutrons and γ-rays. *Nucl. Instrum. and Meth.*, A594:79–89, 2008.

[37] R.H. Johnson, D.T. Ingersoll, B.W. Wehring, and J.J. Dorning. NE-213 neutron spectrometry system for measurements from 1.0 to 20 MeV. *Nucl. Instrum. and Meth.*, 145:337–346, 1977.

[38] A. Zimbal, M. Reginatto, H. Schuhmacher, L. Bertalot, B. Esposito, F. Poli, J. M. Adams, S. Popovichev, V. Kiptily, and A. Murari. Compact NE213 neutron spectrometer with high energy resolution for fusion applications. *Review of Scientific Instruments*, 45:3553–3555, 2004.

[39] L.J. Perkins and M. C. Scott. The application of pulse shape discrimination in NE-213 to neutron spectrometry. *Nucl. Instrum. and Meth.*, 166:451–464, 1979.

[40] Y. Kaschuck and B. Esposito. Neutron/γ-ray digital pulse shape discrimination with organic scintillators. *Nucl. Instrum. and Meth.*, A551:420–428, 2005.

[41] N.V. Kornilov, I. Fabry, S. Oberstedt, and F.J. Hambsch. Total characterization of neutron detectors with a ^{252}Cf source and a new light output determination. *Nucl. Instrum. and Meth.*, A599:226–233, 2009.

[42] N.P. Hawkes, J.M. Adams, D.S. Bond, S. Croft, O.N. Jarvis, and N. Watkinsa. Measurements of the proton light output function of the organic liquid scintillator NE213 in several detectors. *Nucl. Instrum. and Meth.*, A476:190–194, 2002.

[43] C. Matei, F.J. Hambsch, and S. Oberstedt. Proton light output function and neutron efficiency of a p-terphenyl detector using a ^{252}Cf source. *Nucl. Instrum. and Meth.*, A676:135–139, 2012.

[44] A.A. Naqvi, F.Z. Khiari, A. Aksoy, A. Coban, and M.A. Al-Jalal. Light yield measurements of a NE-213 detector for 2.814.8 MeV neutrons. *Nucl. Instrum. and Meth.*, A325:574–577, 1993.

[45] D. Hermsdorf and K. Seeliger.D. Pasieka. A Monte Carlo program for calculation of efficiency of an organic scintillator for neutron detection. *Nucl. Instrum. and Meth.*, 107:259–268, 1973.

[46] B.K. Kamboj, M.G. Shahani, Phadnis U.V., and D. Sharma. A fast neutron detector with linear energy response. *Nucl. Instrum. and Meth.*, 148:57–60, 1978.

[47] R.T. Kouzes, E.R. Siciliano, J.H. Ely, P.E. Keller, and R.J. McConn. Passive neutron detection for interdiction of nuclear material at borders. *Nucl. Instrum. and Meth.*, A584:383–400, 2008.

[48] B.K. Das and A. Shyam. Development of compact size penning ion source for compact neutron generator. *Review of Scientific Instruments*, 79:123305, 2008.

[49] D.L. Chichester, J. Brainard, P.R. Schwoebel, K.L. Hertz, and C. Holland. Development of a field desorption ion source for neutron generator applications. *Nucl. Instrum. and Meth.*, B261:835–838, 2007.

[50] M. Lunardon, C. Bottosso, D. Fabris, S. Moretto, G. Nebbia, S. Pesente, G. Viesti, A. Bigongiari, A. Colonna, C. Tintori, V. Valkovic, D. Sudac, P. Peerani, V. Sequeira, and M. Salvato. Front-end electronics and daq for the euritrack tagged neutron inspection system. *Nucl. Instrum. and Meth.*, B261:391–395, 2007.

[51] S. Pesente, G. Nebbia, M. Lunardon, G. Viesti, D. Sudac, K. Na, S. Blagus, and V. Valkovi. Detection of hidden explosives by using tagged neutron beams with sub-nanosecond time resolution. *Nucl. Instrum. and Meth.*, A531:657–667, 2004.

[52] M. Lunardon, G. Nebbia, S. Pesente, G.M. Romagnoli, G. Viesti, M. Barbui, M. Cinausero, E. Fioretto, G. Prete, G. D'Erasmo, M. Palomba, and A. Pantaleo. A large area scanning system using 14 mev neutron tagged beams for non-destructive assays. *Nucl. Instrum. and Meth.*, B213:544–547, 2004.

[53] V. Valkovi, D. Miljani, P. Toma, B. Antolkovi, and M. Furi. Neutron-charged particle coincidence measurements from 14.4 MeV neutron induced reactions. *Nucl. Instrum. and Meth.*, 76:29–34, 1969.

[54] S. Baccaro, K. Blaek, F. de Notaristefani, P. Maly, J.A. Mares, R. Pani, R. Pellegrini, and A. Soluri. Scintillation properties of YAP:Ce. *Nucl. Instrum. and Meth.*, A361:209–215, 1995.

[55] M. Moszyski, M. Kapusta, D. Wolski, W. Klamra, and B. Cederwall. Properties of the YAP:Ce scintillator. *Nucl. Instrum. and Meth.*, A404:157–165, 1998.

[56] H. Haken and H.C. Wolf. *The Physics of Atoms and Quanta.* Springer-Verlag, 1996.

[57] S.A. Ghanem. Monte Carlo calculations of the response features for NaI detectors. *Applied Radiation and Isotopes*, 53:877–880, 2000.

[58] A. Douraghy, D. L. Prout, R. W. Silverman, and A. F. Chatziioannou. Evaluation of scintillator afterglow for use in a combined optical and pet imaging tomograph. *Nucl. Instrum. and Meth.*, A569:557–562, 2006.

[59] Nation Nuclear Data Center. `http://www.nndc.bnl.gov/`.

[60] G.F. Knoll. *Radiation detection and measurement.* John Wiley and Sons, 1989.

[61] H. Klein and F.D. Brooks. *International Workshop on Fast Neutron Detectors and Applications*, 2006.

[62] L. Stevanato, D. Fabris, X. Hao, M. Lunardon, S. Moretto, G. Nebbia, S. Pesente, L. Sajo-Bohus, and G. Viesti. Light output of ej228 scintillation neutron detectors. *Applied Radiation and Isotopes*, 69:369–372, 2011.

[63] O. Klein and Y. Nishina. *Z. Phys*, 52:853, 1929.

[64] N. Kudomi. Energy calibration of plastic scintillators for low energy electrons by using compton scatterings of γ rays. *Nucl. Instrum. and Meth.*, A430:96–99, 1999.

[65] R. Siciliano, J.H. Ely, R.T. Kouzes, J.E. Schweppe, D.M. Strachan, and S.T. Yokuda. Energy calibration of gamma spectra in plastic scintillators using compton kinematic. *Nucl. Instrum. and Meth.*, A594:232–243, 2008.

[66] G. Dietze and H. Klein. Gamma-calibration of NE-213 scintillation counters. *Nucl. Instrum. and Meth.*, 192:549–556, 1982.

[67] E.K. Mace and L.E. Smith. Automated non-destructive assay of UF_6 cylinders: Detector characterization and initial measurements. *Nucl. Instrum. and Meth.*, A652:62–65, 2011.

[68] R.C. Pereira, A.M. Fernandes, A. Neto, J. Sousa, C.A.F. Varandas, J. Cardoso, C.M.B.A. Correia, M. Tardocchi, M. Nocente, G. Gorini, V. Kiptily, B. Syme, and M. Jennison. Pulse analysis for gamma-ray diagnostics atca sub-systems of jet tokamak. *IEEE Transactions on Nuclear Science*, 58:1531–1537, 2011.

[69] A. Douraghy, D. L. Prout, R. W. Silverman, and A. F. Chatziioannou. Evaluation of scintillator afterglow for use in a combined optical and pet imaging tomograph. *Nucl. Instrum. and Meth.*, A569:557–562, 2006.

[70] Marek Moszyski. Energy resolution and non-proportionality of scintillation detectors new observations. *Radiation Measurements*, 45:372–376, 2010.

[71] L. Stevanato, D. Fabris, X. Hao, M. Lunardon, S. Moretto, G. Nebbia, S. Pesente, L. Sajo-Bohus, and G. Viesti. A new facility for non-destructive assay with a time-tagged ^{252}Cf source. *AIP Conf. Proc.*, 1336:181, 2011.

[72] A. Fallu-Labruyere, H. Tan, W. Hennig, and W.K. Warburton. Time resolution studies using digital constant fraction discrimination. *Nucl. Instrum. and Meth.*, A579:247–251, 2007.

[73] C. Carasco, B. Perot, S. Bernard, A. Mariani, J.-L. Szabo, G. Sannie, Th. Roll, V. Valkovic, D. Sudac, G. Viesti, M. Lunardon, C. Bottosso, D. Fabris, G. Nebbia, S. Pesente, S. Moretto, A. Zenoni, A. Donzella, M. Moszynski, M. Gierlik, T. Batsch, D. Wolski, W. Klamra, P. Le Tourneur, M. Lhuissier, A. Colonna, C. Tintori, P. Peerani, V. Sequeira, and M. Salvato. In-field tests of the euritrack tagged neutron inspection system. *Nucl. Instrum. and Meth.*, A588:397–405, 2008.

[74] International Atomic Energy Agency. *Technical and Functional Specifications for Border Monitoring Equipment*. Nuclear Security Series No. 1, 2006.

[75] International Electrotechnical Commission. *Radiation protection instrumentation Hand-held instruments for detection and identification of radioactive isotopes and additionally for the indication of ambient dose equivalent rate from photon radiation*. 2008.

[76] D. Gilliam, S. Leigh, A. Rukhin, and W. Strawderman. Pass-Fail Testing: Statistical Requirements and Interpretations. *J. Res. Natl. Inst. Stand. Technol.*, 114:195–199, 2009.

[77] N. Johnson, S. Kot, and A. Kemp. *Univariate Discrete distributions*. New York, 1992.

[78] K. Wells and D.A. Bradley. A review of x-ray explosives detection techniques for checked baggage. *Applied Radiation and Isotopes*, 70:1729–1746, 2012.

[79] M. Voytchev, P. Chiaro, and R. Rade. Development of international standards for instrumentation used for detection of illicit trafficking of radioactive material. *Radiation Measurements*, 44:1–5, 2009.

[80] J. P. Sullivan, M. W. Rawool-Sullivan, and T. R. Wenz. $LaCl_3$(Ce) and $LaBr_3$(Ce) gamma-ray spectra with various plutonium isotopic and uranium enrichment standards. *Journal of Radioanalytical and Nuclear Chemistr*, 276:699–705, 2008.

[81] W. El Kanawati, B. Perot, C. Carasco, C. Eleon, V. Valkovic, D. Sudac, J. Obhodas, and G. Sannie. Acquisition of prompt gamma-ray spectra induced by 14 Mev neutrons and comparison with Monte Carlo simulations. *Applied Radiation and Isotopes*, 69:732–743, 2011.

[82] M.B. Chadwick and et al. ENDF/B-VII.0, Next generation evaluated nuclear data library for nuclear science and technology. *Nuclear Data Sheets*, 107:2931–3060, 2009.

[83] L. Stewart and R. E. Hunter. Evaluated neutron-induced gamma-ray production cross sections for ^{238}U and ^{235}U. *Report LA-4918 UC-34*, 1972.

[84] Robert C. Runkle. Neutron sensors and their role in nuclear non proliferation. *Nucl. Instrum. and Meth.*, A652:37–40, 2011.

[85] `http://www.eljentechnology.com/images/stories/Data_Sheets/Liquid_Scintillators/EJ-309\%20data\%20sheet.pdf`.

[86] S.A. Pozzi, S.D. Clarke, M. Flaska, and P. Peerani. Pulse-height distributions of neutron and gamma rays from plutonium-oxide samples. *Nucl. Instrum. and Meth.*, A608:310–315, 2009.

[87] A. Lavietes, C. Liquori, M. Pickrell, R. Plenteda, M. Sweet, M. Shigeyama, T. Asano, T. Nagatani, and S. Nakajima. Gamma and neutron detector performance in a MOX fuel fabrication plant environment. In *Proceedings of the International Safeguards Symposium 2010*, Vienna, November 2010. `http://www.iaea.org/OurWork/SV/Safeguards/Symposium/2010/Documents/PapersRepository/340.pdf`.

[88] L. Swiderski, M. Moszynski, D. Wolski, J. Iwanowska, T. Szczesniak, P. Schotanus, and C. Hurlbut. Suppression of gamma-ray sensitivity of liquid scintillators for neutron detection. *Nucl. Instrum. and Meth.*, A652:330–333, 2011.

[89] J. Iwanowska, L. Swiderski, M. Moszynski, T. Szczesniak, P. Sibczynski, N.Z. Galunov, and N.L. Karavaeva. Neutron/gamma discrimination properties of composite scintillation detectors. *JINST*, 6:P07007, 2011.

[90] R. T. Kouzes, J. H. Ely, A. T. Lintereur, E. K. Mace, D. L. Stephens, and M. L. Woodring. Neutron detection gamma ray sensitivity criteria. *Nucl. Instrum. and Meth.*, A654:412–416, 2011.

[91] S. D. Ambers, M. Flaska, and S. A. Pozzi. A hybrid pulse shape discrimination technique with enhanced performance at neutron energies below 500 keV. *Nucl. Instrum. and Meth.*, A638:116–121, 2011.

[92] S. Pesente, G. Nebbia, G. Viesti, F. Daniele, D. Fabris, M. Lunardon, S. Moretto, K. Nad, D. Sudac, and V. Valkovic. Progress in tagged neutron beams for cargo inspections. *Nucl. Instrum. and Meth.*, B261:268–271, 2007.